UNIVERSITY OF CALIFORNIA, SAN DIEGO

Development and Application of *In Situ* Marine Inorganic Carbon Sensors: Quantifying Change at High Spatiotemporal Resolution in the Anthropocene

A dissertation submitted in partial satisfaction of the requirements for the degree
Doctor of Philosophy

in

Oceanography

by

Philip J. Bresnahan, Jr.

Committee in charge:

Todd Martz, Chair
Andrew Dickson
Jules Jaffe
Ralph Keeling
Yu-Hwa Lo

2015

The Dissertation of Philip J. Bresnahan, Jr., is approved, and it is acceptable in quality and form for publication on microfilm and electronically:

Chair

University of California, San Diego

2015

EPIGRAPH

Do unto those downstream as you would have those upstream do unto you.

Wendell Berry

TABLE OF CONTENTS

LIST OF FIGURES

LIST OF TABLES

ACKNOWLEDGEMENTS

I have received an unquantifiable amount of guidance and inspiration from an almost countless number of people. This is a brief set of remarks that doesn't even come close to showing my full appreciation for the help I've received along the way.

First and foremost, I would like to thank my advisor, Todd Martz, for his persistent and flexible presence. Todd was never hard to get a hold of when I (often) found myself lost and wandering through this challenging process. Yet at the same time, he maintained a deliberate distance, always allowing me to stumble a little, but never fall, in order to let me make this thesis, this journey, my own. Todd, thank you for providing me what seemed to be infinite resources, in terms of both laboratory capital and space for creativity. This will surely be one of the most memorable experiences of my career and, despite plenty of (constructive) struggles along the way, one of the most positive.

To my entire committee, Andrew Dickson, Jules Jaffe, Ralph Keeling, and Yu-Hwa Lo, thank you for making yourselves available so frequently and so wholeheartedly throughout my Ph.D. I have long considered Jules, the self-described "enginist/scienteer," to be a role model for my own career, both due to his intellectual creativity and desire to spread his passion for what we are doing here at Scripps and in the broader world of science and engineering. Andrew and Ralph taught two of my favorite, most memorable, and most challenging courses at Scripps. They have continued to challenge me to elevate my expectations of what levels of precision I should attain in all of my work. Andrew and his lab (especially Guy Emanuele, Emily

Bockmon, Laura Fantozzi, George Anderson, and David Cervantes) provided tremendous resources, from the best seawater on the market to the best advice on making reliable seawater CO_2 measurements available. Yu-Hwa offered expertise in microfluidics that I simply couldn't find elsewhere at UCSD or beyond.

Andreas Andersson, Stephen Bennett, and Glenn Ierley have played tremendously valuable roles as professional and academic mentors since my early days at Scripps and offered opportunities that I never could have imagined when I first arrived at Scripps. Thank you. I will do my best to pay it forward.

To my family—Mom, Dad, Christy, Meaghan—thank you so much for not just letting me go off and do this strange Ph.D. thing (across the country, no less!), but for truly encouraging me to chase my dreams, even when they didn't make a whole lot of sense ("you want to move to California to invent a robot to measure a gas that dissolves in the ocean?"). Christy and Meaghan, thanks for your careful balance of pushing me to excel and laughing at me/reminding me not to take myself too seriously. My lab family has given me never-ending guidance and moral support. Yui Takeshita proved (and continues to prove) that just about anything is possible in chemical sensor development and biogeochemical data analysis and that working through the entire night can actually be quite rewarding. Makaila LaShomb, Ellen Briggs, Taylor Wirth, Brittany Peterson, John Ballard, Kiley Yeakel, Kylee Chang, João Almeida, Steve Smith, and Al Zirino, thank you all for the many conversations, both science-related and personal, and assistance with just about everything I can imagine. And to my whole Scripps family and friends (especially Shannon), thank you for helping me stay just barely on this side

of sanity, or at least not letting me wander to the other side alone for too long. The Graduate Office, Marine Science Development Center, Dive/Boating safety crew, Communications Office, Development Office, and entire administration made my entire graduate career go much more smoothly and much more enjoyably. Thank you all!

Chapter 1, in full, is currently being prepared for submission for publication of the material. Bresnahan, P.J., and Martz, T.R. The dissertation author was the primary investigator and author of this material.

Chapter 2, in part, is currently being prepared for submission for publication of the material. Bresnahan, P.J., Martz, T.R., de Almeida, J.L., Maguire, P., Ward, B. The dissertation author was the primary investigator and author of this material.

Chapter 3, in full, is a reprint of material previously published in Methods in Oceanography, 2014: Bresnahan, P.J., Martz, T.R., Takeshita, Y., Johnson, K.S., LaShomb, M. The dissertation author was the primary investigator and author of this paper.

Chapter 4, in full, is currently being prepared for publication of the material. Bresnahan, P.J., Wirth, T., Martz, T.R., Andersson, A., Cyronak, T., D'Angelo, S., Pennise, J., Melville, W.K., Lenain, L., Statom, N. The dissertation author was the primary investigator and author of this material.

VITA

2008 Bachelor of Science, Lehigh University

2010 Master of Science, University of California, San Diego

2015 Doctor of Philosophy, University of California, San Diego

PUBLICATIONS

Bresnahan, P. J., Martz, T. R., Takeshita, Y., Johnson, K. S. and LaShomb, M., 2014 Best Practices for Autonomous Measurement of Seawater pH with the Honeywell Durafet. *Methods in Oceanography*, 9, 44-60. doi:10.1016/j.mio.2014.08.003

Martz, T., Send, U., Ohman, M. D., Takeshita, Y., **Bresnahan, P. J.**, Kim, H.-J. and Nam, S., 2014 Dynamic variability of biogeochemical ratios in the Southern California Current System. *Geophysical Research Letters*, 41, 2496-2501. doi:10.1002/2014gl059332

Martz, T., Takeshita, Y., Rolph, R. and **Bresnahan, P. J.**, 2012 Tracer monitored titrations: measurement of dissolved oxygen. *Analytical Chemistry*, 84, 290-296. doi:10.1021/ac202537f

ABSTRACT OF THE DISSERTATION

Development and Application of *In Situ* Marine Inorganic Carbon Sensors: Quantifying Change at High Spatiotemporal Resolution in the Anthropocene

by

Philip J. Bresnahan, Jr.

Doctor of Philosophy in Oceanography

University of California, San Diego 2015

Professor Todd Martz, Chair

The ocean's sequestration of anthropogenic carbon dioxide has major consequences for global change. Not only does it temper global warming by removing some of the greenhouse gas from the atmosphere, it also results in ocean acidification through the reaction of CO_2 and H_2O. While the environmental science community is well aware of these issues at a broad, global level, there are notable gaps in our understanding of changes occurring over smaller spaces and shorter times. This dissertation describes novel tools that are being developed and implemented in order to fill those gaps. Specifically, it focuses on autonomous, *in situ* systems designed to quantify total dissolved inorganic carbon (the sum of all chemical species formed in

seawater directly through the addition of CO_2 to H_2O) and pH (a measure of the proton concentration in seawater).

The first two chapters describe a "Micro-Rosette" for microfluidic quantification of total dissolved inorganic carbon (DIC) from profiling floats. Chapter 1 deals specifically with optimization of a gas diffusion cell, an integral component of any liquid-to-liquid (*i.e.*, seawater to receiving solution) DIC extraction technique. 109 unique combinations of gas diffusion cell geometry, seawater volume, and diffusion time were tested to rigorously determine the optimal conditions needed in order to quantify DIC repeatably. Chapter 2 incorporates these findings and implements a sixteen-sample microfluidic collection manifold such that seawater can be captured and stored as a profiling float ascends from 2000 m to the surface and subsequently analyzed once the float returns to its "park depth" (~1000 m), where it remains for over a week. Chapter 1 achieves better than 0.2% repeatability in DIC measurements; the multiplexed collection and analysis in Chapter 2 attains 1%.

Chapters 3 and 4 pertain to *in situ* measurement of seawater pH with the Honeywell Durafet. Well over 100 packages implementing the Durafet have been deployed globally; Chapter 3 lays out best practices for utilizing those packages and validating the resulting data by comparing sensor results to discrete samples and thermodynamically and empirically-derived pH values. Chapter 4 illustrates the use of a Durafet packaged specifically for mobile platforms and surface pH mapping applications.

INTRODUCTION

The Anthropocene

Since the beginning of the Industrial Revolution (*circa* 1750), human activity has increased to the point that it exerts many forces stronger than those of the rest of nature. Nobel laureate Paul Crutzen is credited with popularizing the term "Anthropocene," suggesting that the Earth has entered a geological epoch wherein humanity is a dominant planetary force (*Crutzen*, 2006). A distinct human fingerprint can be found on many parts of the globe, from atmospheric gas concentrations to glaciers to rainforests. While it was once believed that humans had a negligible effect on nature, we now understand that we are capable of altering both local and global patterns. Processes generally thought to occur over so-called geologic time (typically 10,000 years or more) are in many cases accelerating to have timescales of months to decades. For example, changes to atmospheric carbon dioxide concentration that would otherwise be controlled by Milankovitch cycles (slight changes to the Earth's orbit with timescales of 20,000-100,000 years) or geologic activity are now dominated by fossil fuel burning and land-use change with timescales of decades.

2013 saw the passing of a remarkable milestone: after more than 800,000 years during which global atmospheric CO_2 concentrations fluctuated between roughly 200 to 300 ppm (*Luthi et al.*, 2008), in May 2013, the Mauna Loa atmospheric CO_2 mole fraction was reported to be greater than 400 ppm for the first time in human history (https://scripps.ucsd.edu/programs/keelingcurve/). While this threshold may hold no intrinsic planetary significance (that is, the round number 400 doesn't mean more to

planetary physics than, say, 399 or 401), the marked increase in global CO_2 concentration (*i.e.*, the "Keeling Curve" (*Keeling et al.*, 1976)) since the dawn of industrialization is among the clearest signs that humanity is radically altering global processes. There are essentially innumerable other aspects to the Anthropocene (*e.g.*, the impact of fertilizer use on nitrogen and phosphorus cycles, the mining to depletion of rare earth metals for electronic devices, species eradication, sea level rise, etc.), each of which demands significant attention. This thesis focuses on quantifying changes in CO_2, specifically the CO_2 that dissolves in the ocean.

Ocean Carbon Cycle and Anthropogenic Perturbations

CO_2, an acid gas, has been understood to be a greenhouse gas (GHG) for well over a century (*Arrhenius*, 1896). Since 1958, atmospheric CO_2 has been continuously measured in Mauna Loa, Hawaii (*Keeling et al.*, 1976), where the atmosphere is well-mixed, far away from point sources (*e.g.*, megacities). Concomitant with the anthropogenic atmospheric increase is an oceanic increase in CO_2 storage as roughly one-quarter of emissions are now sequestered by the ocean. While this process (and that of CO_2 sequestration by land plants) tempers global warming to some degree, it also drastically changes ocean chemistry through the effect known as ocean acidification (*Doney et al.*, 2009).

Ocean CO_2 content, or marine inorganic carbon, is known to be increasing on average, but the spatiotemporal variability of ocean CO_2 uptake and many natural rates (*e.g.*, air-sea CO_2 flux, photosynthesis, respiration, calcification, carbonate dissolution) have proven difficult to quantify, due largely to the spatial scales over which these

processes occur (*Ciais et al.*, 2013; *Bates et al.*, 2014; *Takahashi et al.*, 2009; *Feely et al.*, 2001). Measurements of the four marine inorganic carbon master variables—total dissolved inorganic carbon (DIC), total alkalinity (TA), partial pressure of CO_2 dissolved in seawater (pCO_2), and pH—are increasingly sought in order to quantify these natural and anthropogenic changes. Inorganic carbon measurements typically come from (1) repeat hydrography cruises which only repeat transects approximately once per decade (*Feely et al.*, 2014), (2) ocean time-series sites, such as the Hawaii Ocean Time-series (HOT) and Bermuda Atlantic Time-series Study (BATS), which provide long and well-maintained time-series but little spatial resolution (*Bates et al.*, 2014; *Church et al.*, 2013), and (3) volunteer observing ships (VOSs) which tend to travel along a relatively narrow range of shipping routes (*e.g.*, *Takahashi et al.* (2009)). These approaches have been tremendously valuable for providing new insights into both natural and anthropogenic changes to oceanic carbon inventories; however, it is simply impossible to observe these changes across the full breadth and depth of the ocean using only the tools and techniques that we currently possess.

Coastal heterogeneity has made observations of near-shore processes even more challenging to interpret (*Duarte et al.*, 2013; *Borges*, 2005). Natural CO_2 system variability in coastal ecosystems far exceeds that in the open ocean, on average (*Hofmann et al.*, 2011), making the task of fully closing coastal carbon budgets quite challenging. Furthermore, it has recently been argued that coastal ecosystems may be responsible for storage of a significant portion of labile carbon (*McLeod et al.*, 2011; *Pendleton et al.*, 2012). As coastal ecosystems are developed for human use and

degraded, this so-called “blue carbon” is rapidly oxidized and lost to the atmosphere, compounding the CO_2 problem in a way similar to terrestrial deforestation. Coastal ecosystems, despite their relatively small spatial extent, are thought to be responsible for a significant percentage of carbon cycling (*Cai*, 2011).

In both the open ocean and coastal ecosystems, the relative paucity of inorganic carbon data limits our ability to resolve changes of interest. Measurements of marine inorganic carbon are critical in order to refine estimates of both natural processes and anthropogenic perturbations such that we can quantify the ocean’s role in continued global change.

High Spatiotemporal Resolution, *In Situ* Monitoring

Shipboard discrete sampling of the marine inorganic carbon system will likely continue to be the primary source for high-fidelity measurements for the forseeable future (*Feely et al.*, 2014); however, due to the sheer size of the ocean and spatiotemporal scales of phenomena of interest, ships will never be sufficient (*Ohman et al.*, 2013). Current ship-based sampling programs are far too infrequent to capture upwelling events, phytoplankton blooms, storms, etc. Sensors, both *in situ* and remote, will be increasingly utilized to fill gaps in space and time between these shipboard surveys (*Byrne et al.*, 2010). Stationary (*i.e.*, moored) and mobile sensors play slightly different but equally important roles in observational oceanography; applications of both will be described here.

This thesis has placed particular emphasis on equipping mobile Argo floats with dissolved inorganic carbon (DIC) analyzers. In the past decade, the climate science

community has relied increasingly heavily on Argo, an international project which maintains a fleet of > 3,000 profiling floats to measure temperature and salinity in the upper 2 km of the ocean (*Roemmich et al.*, 2009; *Gould et al.*, 2004). In particular, Argo has provided valuable insights on the ocean's storage of excess heat due to global warming (*Roemmich et al.*, 2015). The majority of work with Argo to date has involved physical oceanography, however several biogeochemical sensors have been evaluated for use on Argo floats, with oxygen, nitrate, and optical sensors receiving the most attention to date (*Johnson et al.*, 2009; *Gruber et al.*, 2007; *Tengberg et al.*, 2006; *Johnson and Coletti*, 2002; *Bishop et al.*, 2002; *Bishop et al.*, 2004). pH and pCO_2 sensors designed for use within the Argo Program are also under development, but not yet widely implemented (*Johnson et al.*, 2013; *Fiedler et al.*, 2013; *Fietzek et al.*, 2014). Argo's global coverage and routine (profiles to 2 km every ten days) provides a unique opportunity to capture biogeochemical cycles at an unprecedented scale.

Dissertation Outline

Chapters 1 and 2 of this dissertation focus on the design of a Micro-Rosette for autonomous, *in situ* DIC analysis from a profiling float. Autonomous DIC analysis has been achieved in several cases for moored sensors (*Liu et al.*, 2013; *Fassbender et al.*, 2015; *Sayles and Eck*, 2009; *Wang et al.*, 2015) but autonomous profiling DIC analyzers have remained elusive. There are two primary reasons that autonomous instruments for DIC profiles have not yet been achieved: 1) size/power: DIC is the sum of multiple species ($DIC = [CO_{2(aq)}] + [H_2CO_3] + [HCO_3^-] + [CO_3^{2-}]$); its quantification requires pumps, valves, and additional reagents, complicating the apparatus and 2) time: all DIC

analyzers implement an acidification step followed by extraction of CO_2 into a receiving stream; these steps take time (tens of seconds to tens of minutes) that do not lend themselves to on-the-fly measurements necessary for mobile platforms. The Micro-Rosette attempts to overcome these challenges by prioritizing miniaturization of the entire system, especially fluidic components, and by utilizing a unique technique for chemical analysis on profiling floats: capturing discrete samples *in situ* and analyzing them during the float's park cycle (i.e., *ex situ*) in order to circumvent time concerns. The Micro-Rosette is designed to capture multiple microfluidic (tens to hundreds of microliters) seawater samples as the profiling float ascends from 2 km to the surface and subsequently analyze them upon the float's return to an isopycnal at roughly 1 km.

Chapter 1 (submitted to *Analytical Chemistry*) concerns optimization of a microfluidic gas diffusion cell (GDC) for liquid-to-liquid CO_2 extraction in the Micro-Rosette. The results presented here are applicable to all DIC analyzers which implement a liquid-to-liquid extraction step. Twelve unique GDCs were tested, five of which were rigorously evaluated for repeatability in DIC quantification. A primary constraint in GDC evaluation was volume. Sample volumes from 15-500 μL were evaluated, with an emphasis on minimizing volume requirements. 109 unique experiments varied GDC type (planar vs. cylindrical), aspect ratio (surface area of exchanging membrane to reagent volume), sample (*i.e.*, seawater) volume, and diffusion time to optimize the design. 3-D printing was utilized in order to rapidly prototype and evaluate these designs; each manifold was designed, fabricated, and tested in under one month, allowing a thorough intercomparison of unique designs. Ultimately, it was determined

that cylindrical GDCs perform better than their planar counterparts, likely due to the relative ease of increasing the aspect ratio while minimizing overall volume requirements without sacrificing GDC robustness. Most designs achieved better than 1% repeatability in DIC analysis, but only one cylindrical manifold achieved better than 0.2% repeatability over a range of conditions. This cylindrical design is used in the Micro-Rosette design, described in Chapter 2.

In Chapter 2, we evaluate the full assembly of the Micro-Rosette in laboratory, test tank, and oceanographic experiments. The Micro-Rosette, comprising two main instrument housings (an "electronics" controller housing and a "fluidic" seawater collection and analysis housing) is tested for its repeatability and dynamic range in seawater DIC analysis. The Micro-Rosette fluidic housing consists of a sixteen cell microfluidic (100 μL) sample collection manifold, gas diffusion cell, and detector, each custom-designed for this application and described in detail in this chapter. Ultimately, the Micro-Rosette achieves roughly 1% repeatability and 1.5% accuracy for seawater samples ranging from 2000-2500 $\mu mol \cdot kg^{-1}$ and shows viability in oceanographic deployment to 500 m.

Chapter 3 (published in *Methods in Oceanography*) describes best practices for autonomous measurement of seawater pH using the Honeywell Durafet. The Durafet is an off-the-shelf ion selective field effect transistor (ISFET)-based pH sensor. The Durafet has been deployed in multiple configurations and > 100 oceanographic settings from the surface to < 100 m. We describe calibration and validation considerations for this highly stable pH sensor which was first evaluated for oceanographic applications

by *Martz et al.* (2010) and has since been implemented in a variety of ecosystems (*e.g.*, *Hofmann et al.* (2011)). In this work, we cross-compare alternate *in situ* calibration and validation techniques, focusing on the use of discrete samples and co-located, independent CO_2 system sensors with thermodynamic and regional empirical relationships. We investigate multiple sensor failure modes and recommend best practices for preventing. The Durafet is shown to be capable of achieving better than 0.03 pH accuracy, relative to a chosen reference value, over multiple months when it is rigorously calibrated pre-deployment and carefully validated through use of independent pH measurements throughout its deployment.

In Chapter 4, we report on the design of a novel pH and oxygen sensor package for use on mobile platforms (*e.g.*, surface gliders or small vessels). The sensor package, named the "WavepHOx" implements the Honeywell Durafet pH sensor, Aanderaa optode oxygen sensor, and a chloride ion selective electrode. Both the Durafet and optode contain thermistors; the full suite of measured parameters includes pH, dissolved oxygen, and temperature. Multiple deployments are described to illustrate the WavepHOx's utility in high spatiotemporal coastal inorganic carbon monitoring where alternate techniques (*e.g.*, discrete sampling programs or moored sensors) fall short in terms of measurement frequency and/or spatial coverage. The WavepHOx was deployed on a stand-up paddleboard in Mission Bay and La Jolla Cove, CA, USA—in both deployments, resolving a > 0.3 pH change over tens of meters due to natural variability as a result of biological productivity. It was also deployed on a Liquid Robotics Wave Glider. While the WavepHOx is not suited for profiling applications, it

is shown to be a robust instrument package for inorganic carbon mapping, especially in near-shore ecosystems that can be hard to access with ships or profiling floats.

References

Crutzen, P. J., 2006 The "Anthropocene". *Earth System Science in the Anthropocene*, 13-18. doi:10.1007/3-540-26590-2_3

Luthi, D., Le Floch, M., Bereiter, B., Blunier, T., Barnola, J.-M., Siegenthaler, U., Raynaud, D., Jouzel, J., Fischer, H., Kawamura, K. and Stocker, T. F., 2008 High-resolution carbon dioxide concentration record 650,000-800,000[thinsp]years before present. *Nature*, 453, 379-382. doi:10.1038/nature06949

Keeling, C. D., Bacastow, R. B., Bainbridge, A. E., Ekdahl, C. A., Guenther, P. R., Waterman, L. S. and Chin, J. F. S., 1976 Atmospheric carbon dioxide variations at Mauna Loa Observatory, Hawaii. *Tellus*, 28, 538-551. doi:10.1111/j.2153-3490.1976.tb00701.x

Arrhenius, S., 1896 XXXI. On the influence of carbonic acid in the air upon the temperature of the ground. *Philosophical Magazine Series 5*, 41, 237-276. doi:10.1080/14786449608620846

Doney, S. C., Fabry, V. J., Feely, R. A. and Kleypas, J. A., 2009 Ocean acidification: the other CO2 problem. *Ann Rev Mar Sci*, 1, 169-92. doi:10.1146/annurev.marine.010908.163834

Ciais, P., Sabine, C., Bala, G., Bopp, L., Brovkin, V., Canadell, J., Chhabra, A., DeFries, R., Galloway, J., Heimann, M., Jones, C., Quéré, C. L., Myneni, R. B., Piao, S. and Thornton, P., 2013 Carbon and Other Biogeochemical Cycles. *Climate Change 2013: The Physical Science Basis. Contribution of Working Group I to the Fifth Assessment Report of the Intergovernmental Panel on Climate Change*, 465–570. doi:10.1017/CBO9781107415324.015

Bates, N., Astor, Y., Church, M., Currie, K., Dore, J., Gonaález-Dávila, M., Lorenzoni, L., Muller-Karger, F., Olafsson, J. and Santa-Casiano, M., 2014 A Time-Series View of Changing Ocean Chemistry Due to Ocean Uptake of Anthropogenic CO2 and Ocean Acidification. *Oceanography*, 27, 126-141. doi:10.5670/oceanog.2014.16

Takahashi, T., Sutherland, S. C., Wanninkhof, R., Sweeney, C., Feely, R. A., Chipman, D. W., Hales, B., Friederich, G., Chavez, F., Sabine, C., Watson, A., Bakker, D. C.

E., Schuster, U., Metzl, N., Yoshikawa-Inoue, H., Ishii, M., Midorikawa, T., Nojiri, Y., Körtzinger, A., Steinhoff, T., Hoppema, M., Olafsson, J., Arnarson, T. S., Tilbrook, B., Johannessen, T., Olsen, A., Bellerby, R., Wong, C. S., Delille, B., Bates, N. R. and de Baar, H. J. W., 2009 Climatological mean and decadal change in surface ocean pCO2, and net sea–air CO2 flux over the global oceans. *Deep Sea Research Part II: Topical Studies in Oceanography*, 56, 554-577. doi:10.1016/j.dsr2.2008.12.009

Feely, R., Sabine, C., Takahashi, T. and Wanninkhof, R., 2001 Uptake and Storage of Carbon Dioxide in the Ocean: The Global CO2 Survey. *Oceanography*, 14, 18-32. doi:10.5670/oceanog.2001.03

Feely, R. A., L. D. Talley, J. L. Bullister, C. A. Carlson, S. C. Doney, R. A. Fine, E. Firing, N. Gruber, D. A. Hansell, G. C. Johnson, R. M. Key, C. Langdon, A. Macdonald, J. T. Mathis, S. Mecking, F. J. Millero, C. W. Mordy, C. L. Sabine, W. M. Smethie, J. H. Swift, A. M. Thurnherr, R. H. Wanninkhof and Warner, M. J., 2014 The US Repeat Hydrography CO2/Tracer Program (GO-SHIP): Accomplishments from the first decadal survey. A US CLIVAR and OCB Report. 47.

Church, M. J., Lomas, M. W. and Muller-Karger, F., 2013 Sea change: Charting the course for biogeochemical ocean time-series research in a new millennium. *Deep Sea Research Part II: Topical Studies in Oceanography*, 93, 2-15. doi:10.1016/j.dsr2.2013.01.035

Duarte, C. M., Hendriks, I. E., Moore, T. S., Olsen, Y. S., Steckbauer, A., Ramajo, L., Carstensen, J., Trotter, J. A. and McCulloch, M., 2013 Is Ocean Acidification an Open-Ocean Syndrome? Understanding Anthropogenic Impacts on Seawater pH. *Estuaries and Coasts*, 36, 221-236. doi:10.1007/s12237-013-9594-3

Borges, A., 2005 Do we have enough pieces of the jigsaw to integrate CO2 fluxes in the coastal ocean? *Estuaries*, 28, 3-27. doi:10.1007/BF02732750

Hofmann, G. E., Smith, J. E., Johnson, K. S., Send, U., Levin, L. A., Micheli, F., Paytan, A., Price, N. N., Peterson, B., Takeshita, Y., Matson, P. G., Crook, E. D., Kroeker, K. J., Gambi, M. C., Rivest, E. B., Frieder, C. A., Yu, P. C. and Martz, T. R., 2011 High-frequency dynamics of ocean pH: a multi-ecosystem comparison. *PLoS One*, 6, e28983. doi:10.1371/journal.pone.0028983

McLeod, E., Chmura, G. L., Bouillon, S., Salm, R., Björk, M., Duarte, C. M., Lovelock, C. E., Schlesinger, W. H. and Silliman, B. R., 2011 A blueprint for blue carbon: toward an improved understanding of the role of vegetated coastal habitats in sequestering CO2. *Frontiers in Ecology and the Environment*, 9, 552-560. doi:10.1890/110004

Pendleton, L., Donato, D. C., Murray, B. C., Crooks, S., Jenkins, W. A., Sifleet, S., Craft, C., Fourqurean, J. W., Kauffman, J. B., Marba, N., Megonigal, P., Pidgeon, E., Herr, D., Gordon, D. and Baldera, A., 2012 Estimating global "blue carbon" emissions from conversion and degradation of vegetated coastal ecosystems. *PLoS One*, 7, e43542. doi:10.1371/journal.pone.0043542

Cai, W. J., 2011 Estuarine and coastal ocean carbon paradox: CO2 sinks or sites of terrestrial carbon incineration? *Ann Rev Mar Sci*, 3, 123-45. doi:10.1146/annurev-marine-120709-142723

Ohman, M., Rudnick, D., Chekalyuk, A., Davis, R., Feely, R., Kahru, M., Kim, H.-J., Landry, M., Martz, T., Sabine, C. and Send, U., 2013 Autonomous Ocean Measurements in the California Current Ecosystem. *Oceanography*, 26, 18-25. doi:10.5670/oceanog.2013.41

Byrne, R. H., DeGrandpre, M. D., Short, R. T., Martz, T. R., Merlivat, L., McNeil, C., Sayles, F. L., Bell, R. and Fietzek, P., 2010 Sensors and Systems for In Situ Observations of Marine Carbon Dioxide System Variables. *Proceedings of OceanObs'09: Sustained Ocean Observations and Information for Society (Vol. 2)*. doi:10.5270/OceanObs09.cwp.13

Roemmich, D., Johnson, G., Riser, S., Davis, R., Gilson, J., Owens, W. B., Garzoli, S., Schmid, C. and Ignaszewski, M., 2009 The Argo Program: Observing the Global Oceans with Profiling Floats. *Oceanography*, 22, 34-43. doi:10.5670/oceanog.2009.36

Gould, J., Roemmich, D., Wijffels, S., Freeland, H., Ignaszewsky, M., Jianping, X., Pouliquen, S., Desaubies, Y., Send, U., Radhakrishnan, K., Takeuchi, K., Kim, K., Danchenkov, M., Sutton, P., King, B., Owens, B. and Riser, S., 2004 Argo profiling floats bring new era of in situ ocean observations. *Eos, Transactions American Geophysical Union*, 85, 185-191. doi:10.1029/2004EO190002

Roemmich, D., Church, J., Gilson, J., Monselesan, D., Sutton, P. and Wijffels, S., 2015 Unabated planetary warming and its ocean structure since 2006. *Nature Clim. Change*, 5, 240-245. doi:10.1038/nclimate2513

Johnson, K. S., Berelson, W. M., Boss, E., Chase, Z., Claustre, H., Emerson, S. R., Gruber, N., Kortzinger, A., Perry, M. J. and Riser, S. C., 2009 Observing biogeochemical cycles at global scales with profiling floats and gliders prospects for a global array. *Oceanography*, 22, 216-225. doi:10.5670/oceanog.2009.81

Gruber, N., Doney, S., Emerson, S., Gilbert, D., Kobayashi, T., Körtzinger, A., Johnson, G., Johnson, K., Riser, S. and Ulloa, O., 2007 The ARGO-Oxygen Program-A

white paper to promote the addition of oxygen sensors to the international Argo float program.

Tengberg, A., Hovdenes, J., Andersson, H. J., Brocandel, O., Diaz, R., Hebert, D., Arnerich, T., Huber, C., Körtzinger, A., Khripounoff, A., Rey, F., Rönning, C., Schimanski, J., Sommer, S. and Stangelmayer, A., 2006 Evaluation of a lifetime-based optode to measure oxygen in aquatic systems. *Limnology and Oceanography: Methods*, 4, 7-17. doi:10.4319/lom.2006.4.7

Johnson, K. S. and Coletti, L. J., 2002 In situ ultraviolet spectrophotometry for high resolution and long-term monitoring of nitrate, bromide and bisulfide in the ocean. *Deep Sea Research Part I: Oceanographic Research Papers*, 49, 1291-1305. doi:10.1016/S0967-0637(02)00020-1

Bishop, J. K. B., Davis, R. E. and Sherman, J. T., 2002 Robotic Observations of Dust Storm Enhancement of Carbon Biomass in the North Pacific. *Science*, 298, 817-821. doi:10.1126/science.1074961

Bishop, J. K. B., Wood, T. J., Davis, R. E. and Sherman, J. T., 2004 Robotic Observations of Enhanced Carbon Biomass and Export at 55°S During SOFeX. *Science*, 304, 417-420. doi:10.1126/science.1087717

Johnson, K. S., Jannasch, H. W., Coletti, L. J., Carlson, R., Brown, G., Nohava, T., Martz, T. R., Takeshita, Y., Swift, D. and Riser, S. C., 2013 Towards a global ocean pH observing system: First observations with Deep-Sea Durafet pH sensors on profiling floats. *ASLO Aquatic Sciences Meeting*.

Fiedler, B., Fietzek, P., Vieira, N., Silva, P., Bittig, H. C. and Körtzinger, A., 2013 In Situ CO2 and O2 Measurements on a Profiling Float. *Journal of Atmospheric and Oceanic Technology*, 30, 112-126. doi:10.1175/jtech-d-12-00043.1

Fietzek, P., Fiedler, B., Steinhoff, T. and Körtzinger, A., 2014 In situ Quality Assessment of a Novel Underwater pCO2 Sensor Based on Membrane Equilibration and NDIR Spectrometry. *Journal of Atmospheric and Oceanic Technology*, 31, 181-196. doi:10.1175/JTECH-D-13-00083.1

Liu, X., Byrne, R. H., Adornato, L., Yates, K. K., Kaltenbacher, E., Ding, X. and Yang, B., 2013 In situ spectrophotometric measurement of dissolved inorganic carbon in seawater. *Environ Sci Technol*, 47, 11106-14. doi:10.1021/es4014807

Fassbender, A. J., Sabine, C. L., Lawrence-Slavas, N., De Carlo, E. H., Meinig, C. and Maenner Jones, S., 2015 Robust sensor for extended autonomous measurements of surface ocean dissolved inorganic carbon. *Environ Sci Technol*, 49, 3628-35. doi:10.1021/es5047183

Sayles, F. L. and Eck, C., 2009 An autonomous instrument for time series analysis of TCO2 from oceanographic moorings. *Deep Sea Research Part I: Oceanographic Research Papers*, 56, 1590-1603. doi:10.1016/j.dsr.2009.04.006

Wang, Z. A., Sonnichsen, F. N., Bradley, A. M., Hoering, K. A., Lanagan, T. M., Chu, S. N., Hammar, T. R. and Camilli, R., 2015 In Situ Sensor Technology for Simultaneous Spectrophotometric Measurements of Seawater Total Dissolved Inorganic Carbon and pH. *Environ Sci Technol*. doi:10.1021/es504893n

Martz, T. R., Connery, J. G. and Johnson, K. S., 2010 Testing the Honeywell Durafet for seawater pH applications. *Limnology and Oceanography: Methods*, 8, 172-184. doi:10.4319/lom.2010.8.172

CHAPTER 1: CHARACTERIZATION OF GAS DIFFUSION CELL GEOMETRY FOR A MICROFLUIDIC DISSOLVED INORGANIC CARBON ANALYZER

Abstract

Variable gas diffusion cell geometries were tested for the extraction of dissolved inorganic carbon (DIC) from a microfluidic (tens to hundreds of microliters) seawater sample. With a focus on optimization of diffusion cell geometry, we compare five unique diffusion cell designs. Using 3-D printing technology to streamline the prototyping and testing process, we were able to conceive, design, fabricate, and thoroughly evaluate each design over the course of about one month. The five manifolds compared in this work represent a subset of twelve designs total, seven of which failed for various reasons, frequently related to poor membrane sealing within the manifolds. In total, 1,043 DIC measurements were carried out in 109 experiments for the five working manifolds. We find that cylindrical diffusion cell designs offer several advantages over their planar counterparts, most notably the ability to increase the ratio of the exchange membrane's contact surface area to solution volume (the "aspect ratio") without sacrificing channel integrity. Multiple designs approached short-term repeatability of < 1%, but only the cylindrical diffusion cell design allowed for < 0.2% repeatability using less than 200 μL of sample.

Introduction

Atmospheric CO_2 levels are increasing due to human activities; as a result, oceanic dissolved inorganic carbon (DIC = $[CO_{2(aq)}] + [H_2CO_3] + [HCO_3^-] + [CO_3^{2-}]$)

content is as well (*Bates et al.*, 2014; *Sabine and Tanhua*, 2010). In addition to tracking anthropogenic carbon in the ocean, other rationales for measuring DIC include, for example, quantification of marine biological photosynthesis and respiration rates, natural carbon sequestration, and air-sea gas fluxes (*Emerson*, 2014; *Wanninkhof et al.*, 2009; *McLeod et al.*, 2011). Among the four marine CO_2 system master variables (*viz.*, 1) DIC, 2) total alkalinity (TA), 3) pH, and 4) the partial pressure of CO_2 dissolved in seawater (pCO_2)), only DIC and TA are independent from pressure and temperature (when expressed as $\mu mol \cdot kg^{-1}$). This independence allows their use in the direct tracking of biogeochemical changes of a water mass not possible with pH or pCO_2, a particularly valuable trait for use in carbon budgets. Over the past forty years, observations of CO_2 system variables, especially DIC and TA, have been made decadally along several basin-wide cruise transects (*Feely et al.*, 2014), and monthly at a handful of Eulerian time-series stations (*Bates et al.*, 2014). Extensive, yet sporadic underway mapping of surface pCO_2 has also been carried out in the surface ocean using shipboard underway systems (*Takahashi et al.*, 2014). The aim of this work is to aid the development of new autonomous DIC analyzers to fill in the observational gaps remaining in both space and time (*Byrne et al.*, 2010).

Because DIC is a summation of four chemical species, direct electro- or spectro-chemical detection is unlikely, if not impossible. DIC analysis, therefore, employs an acidification step to drive all DIC species to CO_2, requiring pumps, valves, and reagents, and complicating the apparatus. The few *in situ*, autonomous DIC analyzers that have been developed (*Wang et al.*, 2015; *Liu et al.*, 2013; *Sayles and Eck*, 2009; *Fassbender*

et al., 2015) remain at a prototype stage (*Martz et al.*, 2015). Bench-top analyzers routinely achieve 0.1% relative standard deviation (RSD: standard deviation divided by mean) (*Johnson et al.*, 1985; *Johnson et al.*, 1987); autonomous systems have been reported to yield similar results but typically only over several week deployments (*Wang et al.*, 2015; *Liu et al.*, 2013; *Sayles and Eck*, 2009; *Fassbender et al.*, 2015). Here we report results with similar precision and minimized reagent and sample volume requirements with the goal of developing a DIC analyzer suited for long-term oceanographic deployments.

A typical DIC analysis can be broken down into three main steps: 1) acidification of the seawater sample to convert all inorganic carbon species to CO_2, 2) extraction of the CO_2 from the sample, and 3) detection of the extracted CO_2 (after conversion to CO_2, the DIC may be quantified using a variety of techniques including infrared gas analysis, spectrophotometry, and conductometry). CO_2 extraction from the seawater sample can be performed in a variety of ways, depending primarily on the detection scheme. The most commonly used is a liquid-to-gas CO_2 extraction, wherein CO_2 is stripped from an acidified liquid sample by a nitrogen gas stream. The CO_2 is then carried to a detector, such as an infrared gas analyzer (*Goyet and Snover*, 1993; *O'Sullivan and Millero*, 1998). Alternatively, liquid-to-liquid extraction of CO_2 may be accomplished using a gas diffusion cell (GDC) (*Wang et al.*, 2015; *Liu et al.*, 2013; *Sayles and Eck*, 2009; *Martinotti et al.*, 2012; *Hall and Aller*, 1992)—the subject of this work. While several articles have reported on the performance of their chosen GDC in DIC analysis (*Wang et al.*, 2015; *Liu et al.*, 2013; *Sayles and Eck*, 2009; *Martinotti et*

al., 2012; *Hall and Aller*, 1992), a thorough comparison of different GDC designs has not been published.

Here we contrast several common GDC assembly methodologies and geometries that, to our knowledge, have not been rigorously compared on a single system utilizing a common sample introduction, detection, and data acquisition system. Membrane efficiencies (*Plant et al.*, 2009) and permeabilities (*Massey*, 2003) have been published. The purpose of carrying out a systematic comparison of this nature is optimization of a DIC measurement in order to meet the stringent requirements of chemical oceanographers who commonly achieve 0.1% RSD using state of the art equipment (*Johnson et al.*, 1985; *Johnson et al.*, 1987). There are many factors involved in selecting optimal geometry (*e.g.*, entire system volume constraints, pump volume constraints, upstream mixing efficiency, detector signal to noise ratio, etc.); an evaluation of these concerns is necessary to aid future GDC design. The scope of this work is not limited to total dissolved inorganic carbon analysis alone; geometric diffusion cell optimization will be useful in the development of other autonomous sensors (*e.g.*, dissolved inorganic ^{13}C, pCO_2, ammonia).

Theory

In the liquid-to-liquid extraction technique described here, CO_2 diffuses across a gas permeable membrane into a receiving solution of NaOH. CO_2 reacts with OH^- to form CO_3^{2-} ion:

$$CO_2 + 2OH^- \leftrightarrow H_2O + CO_3^{2-} \quad (1).$$

As hydroxide continues to be consumed and pH decreases, carbonate ion reacts with carbon dioxide to form bicarbonate:

$$CO_2 + CO_3^{2-} + H_2O \leftrightarrow 2HCO_3^- \quad (2).$$

The limiting conductivity of hydroxide ion is 199.1 $S \cdot cm^2 \cdot equiv^{-1}$ vs. 69.3 and 44.5 $S \cdot cm^2 \cdot equiv^{-1}$ for carbonate and bicarbonate, respectively (at 25 °C) (*Robinson and Stokes*, 1959). As two moles of hydroxide are consumed in Equation 1, the reduction in limiting conductivity is 259.6 $S \cdot cm^2$ per mole of CO_2; conversion to bicarbonate reduces limiting conductivity by only 154.6 $S \cdot cm^2$ per mole of CO_2. At the receiving solution's high pH (≈12), Equation 1 is favored and relatively little bicarbonate ion is formed. The reader is referred to *Sayles and Eck* (2009) for a more thorough quantification of the various carbonate species as a function of the seawater's DIC, and the resulting change in the receiving solution's conductivity.

The change in conductivity is measured with a capacitively coupled contactless conductivity detector (C^4D). Briefly, C^4D technology is based on the same concept as contacting conductivity wherein drive and pickup electrodes, which are in direct contact with the analyte, input and receive, respectively, a current into or out of the analyte. In both contacting and contactless detectors, the voltage drop across the drive and pickup electrodes, resulting from the solution's resistance (or, inversely, conductance), is measured. The principal difference between the techniques lies in C^4D's use of an electrically insulating material in between the electrodes and the medium (*e.g.*, capillary tubing). This insulator acts as a capacitor in the equivalent circuit. The use of C^4D technology forces a more stringent tradeoff between dynamic range and sensitivity than

contacting conductivity detectors due to the fact that the total impedance between drive and pickup electrodes in C^4D depends on several contributing factors in addition to solution conductance. The total impedance of the C^4D circuit, *Z*, is expressed by:

$$Z = \left[\left(\frac{1}{2\pi f c_{w1}} + R_{NaOH} + \frac{1}{2\pi f c_{w2}}\right)^{-1} + 2\pi f c_s\right]^{-1} \quad (3),$$

where f is frequency of an alternating current (AC) drive signal, c_{w1}, c_{w2}, and c_s are wall 1, wall 2, and stray capacitance, and R_{NaOH} is the resistance of the receiving solution (*i.e.*, NaOH, H_2O, CO_3^{2-}, and HCO_3^-). Wall capacitances refer to the insulating layer of the capillary tubing; stray capacitance depends on the medium (silicone oil in this study) occupying the void space in between the ring electrodes and the outer wall of the tubing. We avoid calculating individual terms here and instead record the detector's output voltage, which is proportional to Z, performing all subsequent analyses with those values. For additional details on C^4D, the reader is referred to *Francisco and do Lago* (2009); *Guijt et al.* (2004); *Kuban and Hauser* (2008), and references therein.

Experimental Section

Apparatus

The methodology follows that of *Hall and Aller* (1992) and *Sayles and Eck* (2009), using Certified Reference Material seawater (CRM Batch 135) obtained from Andrew Dickson's laboratory at Scripps Institution of Oceanography (http://cdiac.esd.ornl.gov/oceans/Dickson_CRM/batches.html). Seawater is acidified with excess 24 mM H_3PO_4 (Mallinckrodt Chemicals 2796-05, Lot J02A06) as it is pumped through a static mixing tee (Figure 1.1, SMT, Analytical Scientific Instruments

P/N 412-0150B). All reagents were stored in Scholle DuraShield bags. H_3PO_4 is always used in quantities sufficient to fully protonate all carbonate species contained in a seawater sample slug, converting DIC to CO_2. Because the sample slug is bracketed by acid, the seawater to acid mixing ratio is not a well-defined constant, but a gradient with the highest value at the center of the slug. CO_2 diffuses across a gas permeable membrane within the gas diffusion cell (Figure 1.1, GDC; described at length below) into a receiving stream (7 mM NaOH; Fisher Scientific S318-500, Lot 125708). The active fluidic components shown in the block diagram (Figure 1.1) are The Lee Co. solenoid valves (LFNX0500800B) and stepper motor-controlled syringe pumps (LPVX0524750B, 750 µL stroke). System automation was accomplished with LabVIEW 2013 Professional Development System using a National Instruments sbRIO-9642, chosen for its abundance of analog and digital I/O ports and rapid prototyping capabilities.

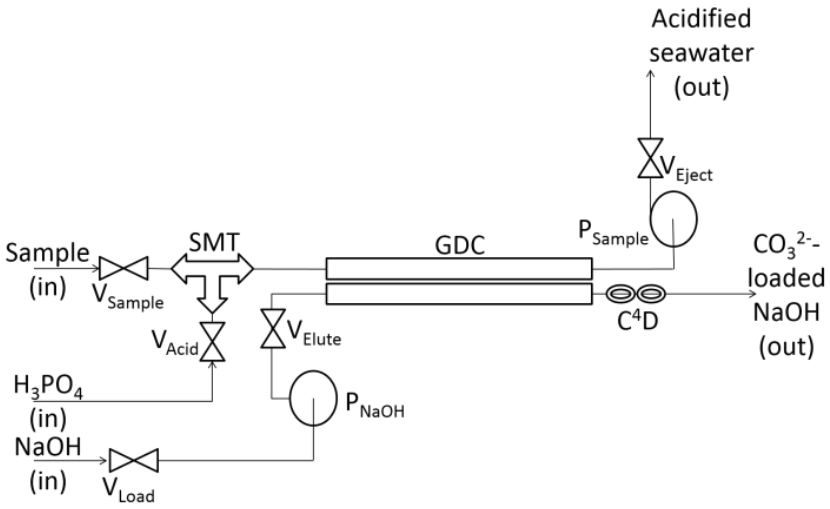

Figure 1.1. Block diagram showing the fluidic circuitry of the bench-top setup. Abbreviations are: variable volume pumps (P_{Sample} and P_{NaOH}), solenoid valves (V_{Sample}, V_{Acid}, V_{Eject}, V_{Load}, and V_{Elute}), static mixing tee (SMT), gas diffusion cell (GDC), and capacitively coupled contactless conductivity detector (C^4D).

GDCs were assembled in five different geometric configurations, grouped broadly into planar or cylindrical (Table 1.1, Figure 1.2). Planar GDCs use two separate plates to sandwich a layer of gas permeable membrane, and are fastened by compression. Cylindrical GDCs consist of a larger tube around a smaller concentric, gas permeable tube. Both designs offer unique advantages and disadvantages with respect to assembly, simplicity, robustness, and gas exchange characteristics. All GDC receiving side volumes were designed to be ≈ 50-70 µL, a volume which allows complete elution of the CO_3^{2-}-loaded NaOH with sufficient baseline stability using less than a single pump stroke (< 750 µL NaOH).

Table 1.1. Geometric descriptions of the five GDCs used in this study. "P" and "C" represent planar and cylindrical GDCs, respectively.

GDC Name	Carrier Vol (µL)	Receiver Vol (µL)	Carrier Contact SA (mm^2)	Receiver Contact SA (mm^2)	Carrier SA:V Aspect Ratio (mm^{-1})	Receiver SA:V Aspect Ratio (mm^{-1})	Membrane Thickness (µm)	Membrane Type
P1	70	70	200.0	200.0	2.9	2.9	81.3	PTFE
P2	150	50	72.5	72.5	0.5	1.5	81.3	PTFE
P3	50	50	72.5	72.5	1.5	1.5	81.3	PTFE
C1	150	50	622.6	331.2	4.2	6.6	279.4	Silicone
C2	150	50	199.9	150.6	1.3	3.0	241.3	Silicone

A planar cell relies on the membrane material itself (Teflon/PTFE, McMaster Carr P/N 6802K77) to serve as a sealing gasket; that is, no additional sealing mechanism is used to keep fluids inside the channels. Three planar GDCs were tested (Table 1.1: P1, P2, P3). P1 is a commercially available unit sold by Global FIA (High Sensitivity Gas Diffusion Unit; P/N HPMSD; HDPE (high-density polyethylene); http://www.globalfia.com/) with 70 µL serpentine tracks. The compression seal on P1 is achieved either by 1) ten socket-head cap screws, washers, and nuts in through-holes around the perimeter or 2) a single aluminum clamping mechanism. P2, P3, C1, and C2

are custom designs (two planar and two cylindrical) designed in-house using SolidWorks 2014 Academic Edition. These GDCs were fabricated using 3-D printing by Solid Concepts, Inc. (http://www.solidconcepts.com/). P2 and P3 were fastened using four screws and nuts around the perimeter. P1 had a 150 µL sample side volume and 50 µL receiving side volume, while P2 contained 50 µL on both sides.

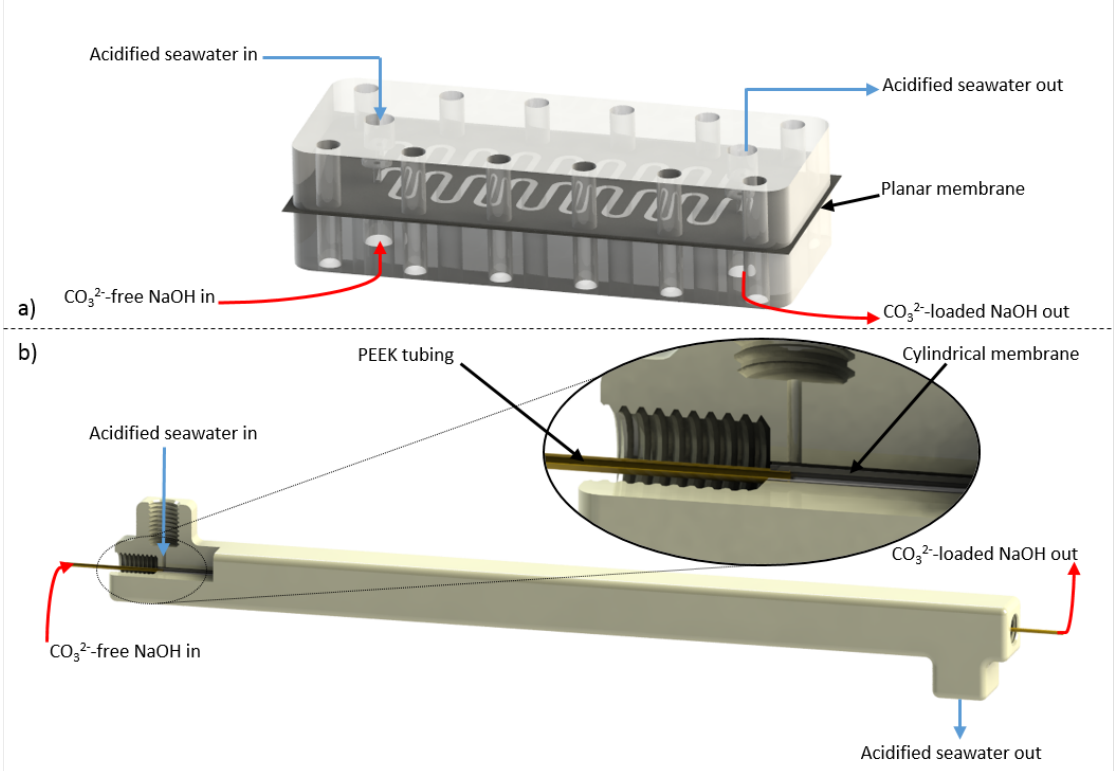

Figure 1.2. Typical assemblies of planar (a) and cylindrical (b) GDCs. ¼-28 inlet and outlet ports were machined or printed into the manifolds for connections to PEEK tubing. Section of cylindrical GDC is cut and magnified to show inner cavity and membrane. See Table 1.1 for dimensions.

C1 and C2 were assembled by fitting a tubular silicone membrane over PEEK tubing. By using PEEK tubing with a slightly larger OD than the silicone tube ID, a compressive seal was created around the PEEK. To promote sealing, a small amount of silicone sealant was applied to the outside of the PEEK tubing immediately prior to

inserting it into the silicone tubing. After waiting 24 hours for the sealant to cure, the tubing assembly was passed through the larger internal cavity of the 3-D printed part. The cylindrical design relies on off-the-shelf HPLC fittings to seal all inlet and outlet ports (and, consequently, hold the PEEK/silicone tubing assembly in place inside the cavity). Internal volume (that is, the volume inside the silicone tubing) can be altered by lengthening or shortening the entire assembly or by using tubing with different dimensions. The annular volume (fluid between the outside of the silicone tubing and inside of the printed cavity) can be altered using the above options or by changing the diameter of the cavity. C1 utilizes 0.025” ID x 0.047” OD Saint-Gobain Standard Bio-Sil over 1/32” OD PEEK while C2 utilizes 0.058” ID x 0.077” OD Saint-Gobain Standard Bio-Sil over 1/16” OD PEEK. Both C1 and C2 were designed with 150 µL sample side volume and 50 µL receiving side volume; their principle differences are the diameter and total length, and therefore aspect ratio (surface area to volume).

Our experimental apparatus implements a capacitively coupled contactless conductivity detector (C^4D, eDAQ ET127, http://wiki.edaq.com/). The C^4D was custom-designed by eDAQ Pty., Ltd., to meet our specifications: dynamic range determined by a maximum conductivity of 7 mM NaOH over a range of temperatures and sufficient sensitivity to detect 0.1% differences in typical seawater DIC values. The C^4D’s differential analog input was sampled at 10 kHz. 1,000 points were averaged and these averages recorded at 10 Hz.

The GDC and C^4D were submerged in silicone oil (Xiameter PMX 200 Silicone Fluid, 20 cS) in a jacketed beaker for temperature control by a recirculating water bath

(Neslab RTE 7). The temperature of the oil bath was held at 20.00±0.05 °C (maximum range over multi-day experiments), which minimized temperature-dependent diffusion and conductivity artifacts.

Procedure

Following Figure 1.3, a measurement cycle consists of the following steps. All steps are performed sequentially, not concurrently. This is therefore considered a stopped-flow system, as opposed to a continuously flowing one. Note that at the end of every pumping step (Steps 1, 3-5, 7-8), the valve which was originally opened in that step is closed and the syringe pump is refilled. 1) The acid valve (V_{Acid}) is opened, and the sample pump (P_{sample}) is used to flush acid through the sample side of the system to remove residual CO_2 from previous runs. 2) A prescribed diffusion time is given to allow the residual CO_2 to diffuse into the receiving stream. 3) The receiving stream elution valve (V_{Elute}) is opened and the receiving side is flushed with the NaOH pump (P_{NaOH}) to remove all remaining CO_2 from the GDC. 4) The sample valve (V_{Sample}) is opened, and an aliquot of seawater is pulled into the mixing tee. 5) V_{Acid} is opened, and acid is again pulled through the system's sample side, thereby pushing the seawater aliquot through the mixing tee and into the GDC. 6) CO_2 diffuses across a gas permeable membrane within the GDC into a NaOH receiving stream. 7) Acid is flushed through the GDC in order to flush out any remaining CO_2 from the sample side and stop the diffusion. 8) V_{elute} is opened and P_{NaOH} elutes the receiving solution, now loaded with CO_3^{2-}, through the C^4D. A primary constraint in system design is the 750 µL single

stroke volume of the variable volume pump selected for this study, which sets the maximum volume of any step in Figure 1.3.

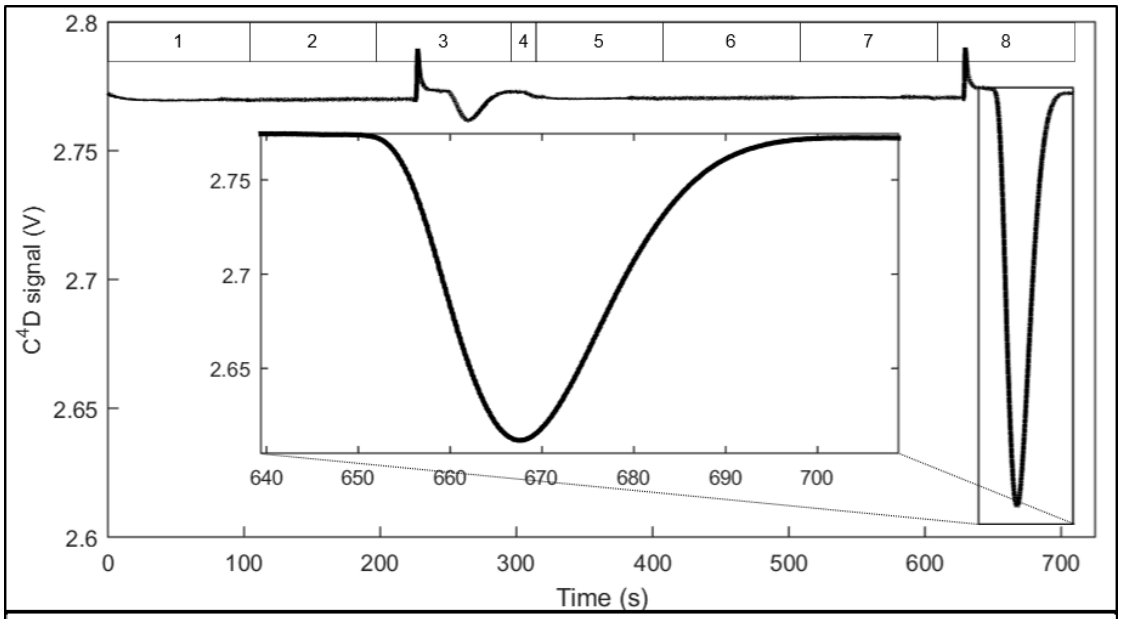

	Step	Vol H_3PO_4 (µL)	Vol NaOH (µL)	Vol Sample (µL)	Time (s)
1	Flush carrier side with H_3PO_4	600	-	-	100
2	Diffuse (rinse)	-	-	-	100-900
3	Flush receiver side with NaOH	-	600	-	100
4	Pull sample into SMT	-	-	0-540	15
5	Pull sample slug from SMT to GDC using H_3PO_4	550	-	-	90
6	Diffuse (sample)	-	-	-	100-900
7	Flush carrier side with H_3PO_4	600	-	-	100
8	Elute NaOH and record C^4D signal	-	600	-	100
Total		**1750**	**1200**	**0-540**	**705-1505**

Figure 1.3. Single sequence illustrating the C^4D response as a function of time. Step 8, CO_3^{2-}-loaded NaOH elution, is magnified in order to highlight the portion of the routine which is analyzed for DIC.

Note two additional salient features in Figure 1.3: 1) a sharp positive upward peak immediately precedes NaOH elution in Steps 3 and 8 and 2) the baseline during elution (again, Steps 3, 8) is slightly higher than during all other steps. The former effect is believed to be the result of the buildup of large pressure gradients at the moment that

the pump is actuated which may cause the PEEK tubing to compress or swell, thereby changing the various capacitances in Equation 3. The latter is the result of slight temperature differences created within the system due to the fact that the reagent bags are not temperature-controlled and the C^4D itself generates heat. Neither of these effects is believed to have any influence on system performance since all analysis uses data from Step 8 after the baseline stabilizes.

Comparison Experiments

Three experimental parameters—GDC type, diffusion time, and sample volume—were varied independently. A total of 1,043 DIC measurements from 109 unique combinations of GDC type, diffusion time, and sample volume are reported (9-10 replicates per experiment). With each GDC described in Table 1.1, we independently varied the sample volume (Figure 1.3, Step 4, 0-540 μL) and diffusion time, (Figure 1.3, Steps 2 and 6, 100-900 s). Seawater was added to the GDC in 15, 30, or 60 μL slugs and given the prescribed amount of diffusion time (Table 1.1). For example, an experiment using 150 μL seawater with a 500 second diffusion time was performed by adding 30 μL acidified seawater and allowing 500 s diffusion (Figure 1.3, Steps 4-6) five times before flushing the sample side and eluting the CO_3^{2-}-loaded NaOH (Figure 1.3, Steps 7-8). In order to determine the system's span, sample volume, as opposed to DIC concentration, is varied as a matter of practicality but the two approaches are considered to be equivalent for our purposes. For a nominal seawater DIC concentration of 2000 $\mu mol \cdot kg^{-1}$ and sample volume of 150 μL, 120-180 μL sample additions, for

example, would represent loading of 1600-2400 $\mu mol \cdot kg^{-1}$ DIC, thereby providing similar information.

Most experimental runs were terminated upon saturation of the National Instruments sbRIO-9642 200 MB memory. As data were recorded constantly throughout the runs for quality control and evaluation purposes, experiments with longer diffusion times filled the memory capacity after fewer runs. The difference between membrane type (material and thickness) utilized in planar vs. cylindrical experiments is addressed in the Results and Discussion.

Figures of Merit

The analytical signal, peak area or "A," is the integral of the trough under the baseline of the elution curve (Figure 1.3, Step 8); however, for diagnostic purposes, we found it useful to record C^4D voltage throughout an entire measurement sequence. The downward trough in conductivity during elution corresponds to the flushing of carbonate with the baseline corresponding to CO_3^{2-}-free NaOH. The baseline is calculated as the line that fits two points: the averages of first and last 100 points (10 seconds) in the elution curve. Peak height was found to be less repeatable than the integral and therefore is not discussed. We report the relative standard deviation (RSD), defined as the standard deviation of repeated elution integrals (s_A) divided by their mean ($\bar{A}$) and multiplied by 100%: $\text{RSD} = \frac{s_A}{\bar{A}} \cdot 100\%$. The analysis was performed using MATLAB R2014a Student Edition.

Results and Discussion

Figure 1.4 presents results from a typical experiment with a variable sample volume (10 replicates per volume increment, 60 measurements total). The standard deviation of peak integral replicates for a given set of conditions was determined to be consistent across all conditions ($s_A \approx 0.01$ V·sec, $n = 10$)—that is, independent of GDC type, diffusion time, or sample volume (or, equivalently, DIC concentration). s_A therefore largely represents indeterminate errors associated with detector baseline noise. Consequently, we fine-tuned the measurement RSD by adjusting peak integral and GDC geometry. Experiments initially increased sample volume in 15 µL steps, but it was eventually determined that most experiments were far from approaching signal saturation. A primary goal of this work was to determine the conditions required to saturate the signal; later experiments utilized 30 or 60 µL increments in sample volume additions.

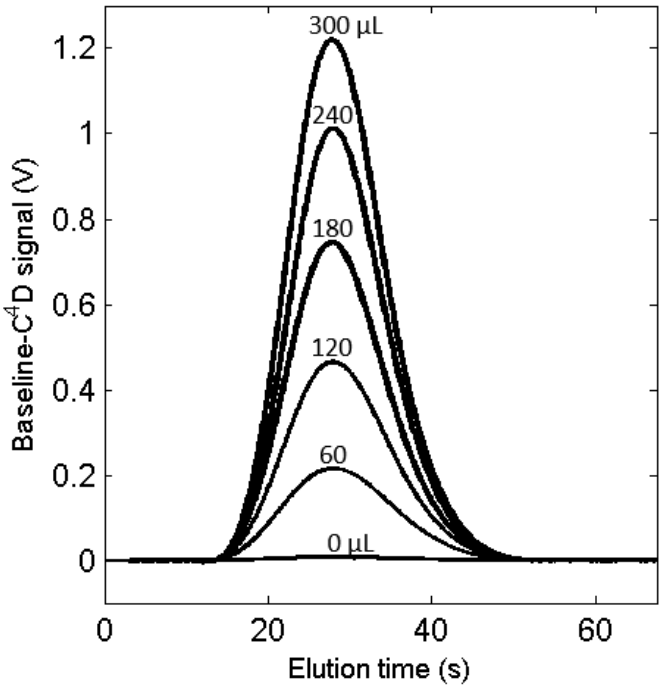

Figure 1.4. Results of elution sequences, shown as each elution curve's baseline minus trough, for sample volumes ranging from 0-300 µL in 60 µL increments. This particular set of experiments utilized the C1 GDC and 900 s diffusion.

Integrating under the peaks for ten replicates each of 109 unique combinations of GDC, diffusion time, and sample volume shows several clear patterns (Figure 1.5). 1) Increasing sample volume linearly increases the integrated signal below 250 µL sample volume for all GDC types and diffusion times. At volumes greater than 250 µL, the integrated signal for C1 begins to saturate around 22 V·sec. This apparent signal saturation is a result of the replacement CO_3^{2-} with HCO_3^-, which has a limiting conductivity closer to that of OH^-. 2) For a given volume, changing the GDC type has the largest influence. The long cylindrical GDC, which has the greatest surface area to volume aspect ratios (Table 1.1), vastly outperforms the other GDCs in terms of sensitivity. 3) Lastly, increasing diffusion time also increases signal strength and

therefore improves RSD. However, the effect of diffusion time over the range tested is not as significant as that of geometry, demonstrated by the clustering of results in Figure 1.6 by GDC type, not diffusion time. On the other hand, given sufficient time, all points in Figure 1.5 should approach the upper curve, representing near quantitative, ≈ 100%, extraction of CO_2 from the acidified sample into the NaOH receiving solution.

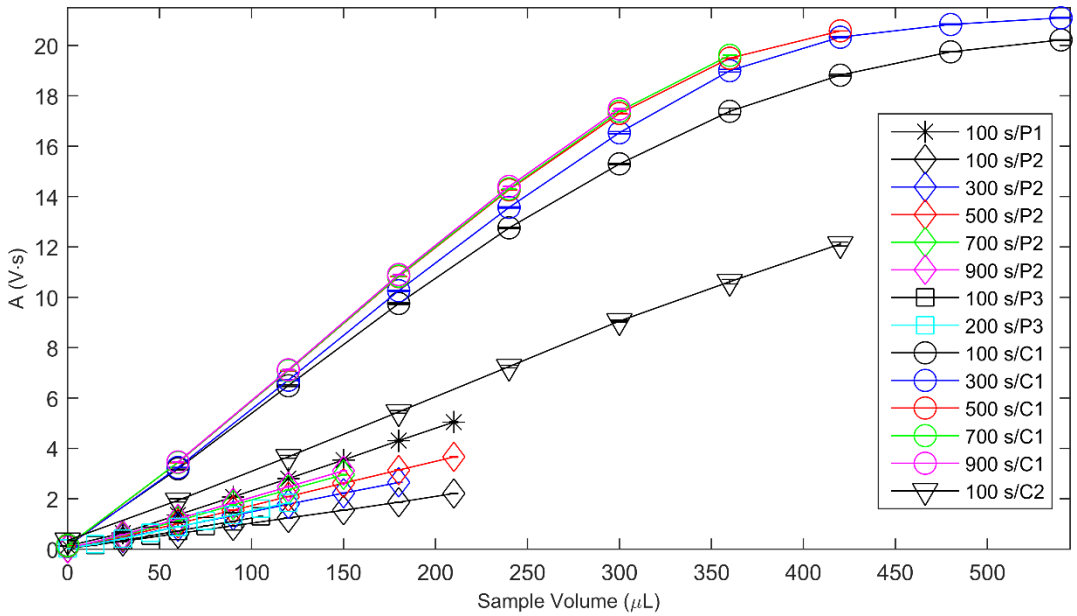

Figure 1.5. Peak integrals, A (mean ± 1 s.d.; *n* = 10), vs. sample volume for 14 unique GDC and diffusion time experiments. Table 1.1 describes the experimental parameters listed in the legend (legend reads: diffusion time/GDC design).

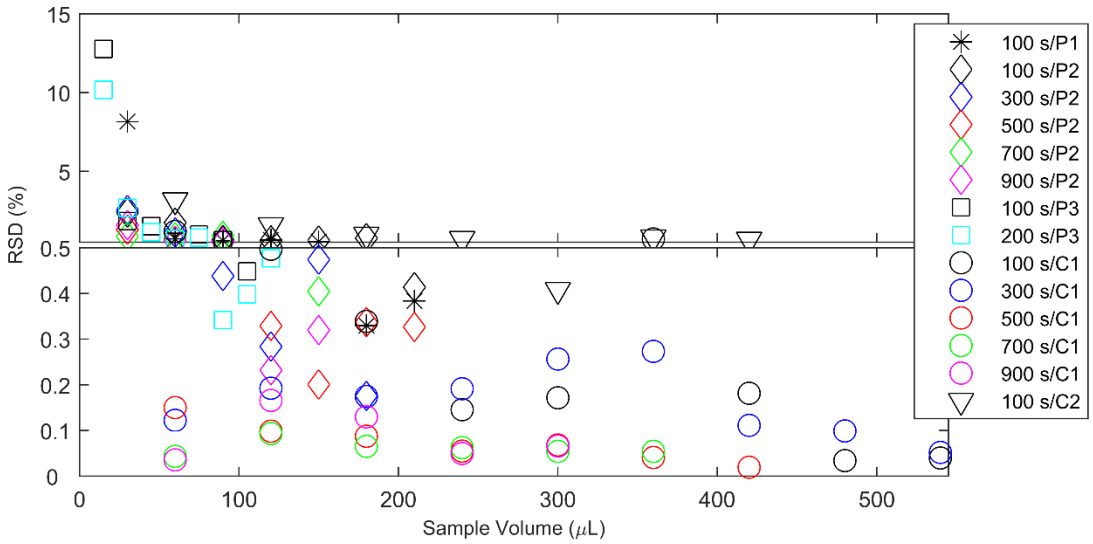

Figure 1.6. RSD plotted as a function of sample volume with scale break at RSD = 0.5% to highlight the best performance. Legend as in Figure 1.5.

The experiments reported here were designed to optimize the sample RSD of DIC measurements in order to achieve measurement precision of use to oceanographers (*i.e.*, < 0.5% RSD, or ≈ 10 μmol·kg^{-1} (*Newton et al.*, 2014)). Figure 1.6 shows RSD for all 109 combinations of GDC type, sample volume, and diffusion time. These results clearly demonstrate the superior performance of the C1 GDC across all volumes and diffusion times.

Conclusions

Microfluidic gas diffusion cells were evaluated in order to compare and contrast the effects of GDC geometry, sample volume, and diffusion time on DIC analysis. 109 unique combinations were tested to optimize the system precision, reported here as relative standard deviation. There are several ways to improve the RSD, namely, increasing A (peak size) or decreasing s_A (*i.e.*, improving repeatability of peak size). From the results described here, we conclude that the former is more complicated as it

depends on the detector signal to noise ratio and pump repeatability, both of which are already quite good and seemingly difficult to improve upon. Increasing the peak size, however, can be done in a variety of different ways, most easily by optimizing the GDC geometry. Increasing diffusion time and total sample volume are also viable alternatives but are not necessarily as desirable when time and volume constraints exist, as is the case for many applications. We hypothesize that a poor GDC aspect ratio (reflecting a large depth to diffusion layer ratio) hinders the diffusion process in a stopped flow system such as the one used in this study, resulting in a non-quantitative transfer of DIC as CO_2 between sample and receiving solution over practical timescales. Non-quantitative transfer compromises RSD and, especially, accuracy due to system memory or lag effects resulting from residual CO_2 remaining in the GDC in between samples.

In addition to the five GDCs evaluated in this study, seven other planar and cylindrical GDCs were constructed but never functioned properly. Typical assembly issues included liquid leaking out of the channels and/or air bubbles leaking into the channels, both leading to system failure. Failed designs included a cylindrical GDC using Bev-A-Line tubing as the outer tubing and HPLC T-fittings to create the inlet/outlet junctions as well as several planar milled PMMA (poly(methyl methacrylate), Figure 2.3) GDCs with through-hole fasteners. Problems with the planar cells likely resulted from uneven sealing surfaces or inconsistent compression across the sealing surface. Even the slightest defect in fabricating the planar sealing surface can result in a failed design and this problem is only compounded by efforts to reduce volume/increase aspect ratio as shallow channels cause large pressure drops during

pumping and are easily clogged by the membrane itself. Cylindrical manifolds, however, typically only leaked at the inlet and outlet ports, suggesting that cylindrical GDCs are robust when care is taken to ensure that threaded ports are properly fabricated and polished. While membrane type and thickness were not explicitly controlled in these experiments, the C2 GDC (which utilized silicone tubing) had similar aspect ratios to the planar GDCs (all of which utilized PTFE membranes). As the C2 GDC performed similarly to the planar GDCs in terms of RSD, we are confident that geometry plays a more significant role than the difference between these two membranes.

The 3-D printed parts described here did not fully utilize the unique advantages of 3-D printing over standard machining capabilities (*e.g.*, larger internal cavities than the through-holes to those cavities, internal meanders, etc.); however, the speed at which parts could be conceived and tested made 3-D printing a desirable approach. For example, machining a GDC like the long cylindrical cell would have been challenging due to the long (166 mm) but narrow (ID = 1.6 mm) channel. Incorporating additional features such as integrated static mixers will be straightforward with rapidly improving 3-D printing technology.

Cylindrical diffusion cells offer several notable advantages over their planar counterparts, including relative ease of sealing to prevent leakage, a high contact surface area/high surface area to volume aspect ratio, and complete enclosure of diffusion membrane. The analysis presented here will aid in the design and fabrication of diffusion cells for dissolved inorganic carbon analyzers and can likely be extended to other systems wherein gas diffusion is integral.

Acknowledgements

This work was supported by NSF-OCE 0961250. PJB was supported by the Department of Defense (DoD) through the National Defense Science and Engineering Graduate (NDSEG) Fellowship Program. The authors wish to thank Yuichiro Takeshita for helpful review of this manuscript and guidance throughout experimentation.

Chapter 1, in full, is currently being prepared for submission for publication of the material. Bresnahan, P.J., and Martz, T.R. The dissertation author was the primary investigator and author of this material.

References

Bates, N., Astor, Y., Church, M., Currie, K., Dore, J., Gonaález-Dávila, M., Lorenzoni, L., Muller-Karger, F., Olafsson, J. and Santa-Casiano, M., 2014 A Time-Series View of Changing Ocean Chemistry Due to Ocean Uptake of Anthropogenic CO2 and Ocean Acidification. *Oceanography*, 27, 126-141. doi:10.5670/oceanog.2014.16

Sabine, C. L. and Tanhua, T., 2010 Estimation of Anthropogenic CO2 Inventories in the Ocean. *Annual Review of Marine Science*, 2, 175-198. doi:10.1146/annurev-marine-120308-080947

Emerson, S., 2014 Annual net community production and the biological carbon flux in the ocean. *Global Biogeochemical Cycles*, 28, 14-28. doi:10.1002/2013gb004680

Wanninkhof, R., Asher, W. E., Ho, D. T., Sweeney, C. and McGillis, W. R., 2009 Advances in quantifying air-sea gas exchange and environmental forcing. *Ann Rev Mar Sci*, 1, 213-44. doi:10.1146/annurev.marine.010908.163742

McLeod, E., Chmura, G. L., Bouillon, S., Salm, R., Björk, M., Duarte, C. M., Lovelock, C. E., Schlesinger, W. H. and Silliman, B. R., 2011 A blueprint for blue carbon: toward an improved understanding of the role of vegetated coastal habitats in sequestering CO2. *Frontiers in Ecology and the Environment*, 9, 552-560. doi:10.1890/110004

Feely, R. A., L. D. Talley, J. L. Bullister, C. A. Carlson, S. C. Doney, R. A. Fine, E. Firing, N. Gruber, D. A. Hansell, G. C. Johnson, R. M. Key, C. Langdon, A. Macdonald, J. T. Mathis, S. Mecking, F. J. Millero, C. W. Mordy, C. L. Sabine, W. M. Smethie, J. H. Swift, A. M. Thurnherr, R. H. Wanninkhof and Warner, M. J., 2014 The US Repeat Hydrography CO2/Tracer Program (GO-SHIP): Accomplishments from the first decadal survey. A US CLIVAR and OCB Report. 47.

Takahashi, T., Sutherland, S. C., Chipman, D. W., Goddard, J. G., Ho, C., Newberger, T., Sweeney, C. and Munro, D. R., 2014 Climatological distributions of pH, pCO2, total CO2, alkalinity, and CaCO3 saturation in the global surface ocean, and temporal changes at selected locations. *Marine Chemistry*, 164, 95-125. doi:10.1016/j.marchem.2014.06.004

Byrne, R. H., DeGrandpre, M. D., Short, R. T., Martz, T. R., Merlivat, L., McNeil, C., Sayles, F. L., Bell, R. and Fietzek, P., 2010 Sensors and Systems for In Situ Observations of Marine Carbon Dioxide System Variables. *Proceedings of OceanObs'09: Sustained Ocean Observations and Information for Society (Vol. 2)*. doi:10.5270/OceanObs09.cwp.13

Wang, Z. A., Sonnichsen, F. N., Bradley, A. M., Hoering, K. A., Lanagan, T. M., Chu, S. N., Hammar, T. R. and Camilli, R., 2015 In Situ Sensor Technology for Simultaneous Spectrophotometric Measurements of Seawater Total Dissolved Inorganic Carbon and pH. *Environmental Science & Technology*, 49, 4441-4449. doi:10.1021/es504893n

Liu, X., Byrne, R. H., Adornato, L., Yates, K. K., Kaltenbacher, E., Ding, X. and Yang, B., 2013 In situ spectrophotometric measurement of dissolved inorganic carbon in seawater. *Environ Sci Technol*, 47, 11106-14. doi:10.1021/es4014807

Sayles, F. L. and Eck, C., 2009 An autonomous instrument for time series analysis of TCO2 from oceanographic moorings. *Deep Sea Research Part I: Oceanographic Research Papers*, 56, 1590-1603. doi:10.1016/j.dsr.2009.04.006

Fassbender, A. J., Sabine, C. L., Lawrence-Slavas, N., De Carlo, E. H., Meinig, C. and Maenner Jones, S., 2015 Robust sensor for extended autonomous measurements of surface ocean dissolved inorganic carbon. *Environ Sci Technol*, 49, 3628-35. doi:10.1021/es5047183

Martz, T. R., K.L. Daly, R.H. Byrne, J.H. Stillman and Turk, D., 2015 Technology for ocean acidification research: Needs and availability. *Oceanography*, 28, 40-47. doi:10.5670/oceanog.2015.30

Johnson, K. M., King, A. E. and Sieburth, J. M., 1985 Coulometric TCO2 analyses for marine studies; an introduction. *Marine Chemistry*, 16, 61-82. doi:10.1016/0304-4203(85)90028-3

Johnson, K. M., Sieburth, J. M., Williams, P. J. l. and Brändström, L., 1987 Coulometric total carbon dioxide analysis for marine studies: Automation and calibration. *Marine Chemistry*, 21, 117-133. doi:10.1016/0304-4203(87)90033-8

Goyet, C. and Snover, A. K., 1993 High-accuracy measurements of total dissolved inorganic carbon in the ocean: comparison of alternate detection methods. *Marine Chemistry*, 44, 235-242. doi:10.1016/0304-4203(93)90205-3

O'Sullivan, D. W. and Millero, F. J., 1998 Continual measurement of the total inorganic carbon in surface seawater. *Marine Chemistry*, 60, 75-83. doi:10.1016/S0304-4203(97)00079-0

Martinotti, V., Balordi, M. and Ciceri, G., 2012 A flow injection analyser conductometric coupled system for the field analysis of free dissolved CO2 and total dissolved inorganic carbon in natural waters. *Anal Bioanal Chem*, 403, 1083-93. doi:10.1007/s00216-012-5762-8

Hall, P. J. and Aller, R. C., 1992 Rapid, small-volume, flow injection analysis for SCO2, and NH4+ in marine and freshwaters. *Limnology and Oceanography*, 37, 1113-1119. doi:10.4319/lo.1992.37.5.1113

Plant, J. N., Johnson, K. S., Needoba, J. A. and Coletti, L. J., 2009 NH4-Digiscan: an in situ and laboratory ammonium analyzer for estuarine, coastal and shelf waters. *Limnology and Oceanography: Methods*, 7, 144-156. doi:10.4319/lom.2009.7.144

Massey, L. K., 2003 Appendix II - Permeation Rates. *Permeability Properties of Plastics and Elastomers (Second Edition)*, 535-552. doi:10.1016/B978-188420797-6.50097-8

Robinson, R. A. and Stokes, R. H., 1959 Electrolyte Solutions (2nd Revised Edition); Appendix 6.1.

Francisco, K. J. and do Lago, C. L., 2009 A compact and high-resolution version of a capacitively coupled contactless conductivity detector. *Electrophoresis*, 30, 3458-64. doi:10.1002/elps.200900080

Guijt, R. M., Evenhuis, C. J., Macka, M. and Haddad, P. R., 2004 Conductivity detection for conventional and miniaturised capillary electrophoresis systems. *Electrophoresis*, 25, 4032-57. doi:10.1002/elps.200406156

Kuban, P. and Hauser, P. C., 2008 A review of the recent achievements in capacitively coupled contactless conductivity detection. *Anal Chim Acta*, 607, 15-29. doi:10.1016/j.aca.2007.11.045

Newton, J., Feely, R. A., Jewett, E. B., Williamson, P. and Mathis, J., 2014 Global Ocean Acidification Observing Network: Requirements and Governance Plan.

CHAPTER 2: DEVELOPMENT OF A MICRO-ROSETTE FOR *IN SITU* MEASUREMENT OF DISSOLVED INORGANIC CARBON ON PROFILING FLOATS

Abstract

We have constructed a multi-sampler instrument, named "Micro-Rosette," capable of collecting and storing microfluidic seawater samples and analyzing dissolved inorganic carbon (DIC) content. The Micro-Rosette is intended exclusively for use on autonomous profiling floats such as those in the Argo Program. The proof-of-concept for this device is presented here through a series of tests including benchtop, test tank, and work at-sea. The initial design captures sixteen 100 µL seawater samples for subsequent analysis. A 16 channel profile/analysis cycle requires 28 mL H_3PO_4, 19 mL NaOH, and 60 kJ of power. Internal volume (driving the reagent volume requirement) was scaled for a capacity of 100 total profiles, corresponding to about three years of operation on-board a profiling float operating at ten day profile intervals. In addition to the proof-of-concept, we lay out a path for integrating a prototype Micro-Rosette into a profiling float.

Introduction

The rate of anthropogenic carbon dioxide release to the atmosphere is well understood (IPCC, 2013), but natural carbon fluxes and human perturbations to oceanic processes need to be better constrained. For example, the ocean's CO_2 yearly uptake rate estimates have error bars of 20-50% (*Takahashi et al.*, 2009; *Ciais et al.*, 2013) and

the sign (let alone magnitude) of open ocean net community productivity is disputed (*Ducklow and Doney*, 2013; *Williams et al.*, 2013; *Duarte et al.*, 2013). The ocean is a substantial sink of anthropogenic carbon dioxide; constraining ocean carbon cycles is a critical component of observing and predicting global change.

While measurement inaccuracy contributes to these uncertainties (*Bockmon and Dickson*, 2015), the greater factor is the ocean's spatiotemporal heterogeneity and sheer size. Even with the advent of highly accurate analytical techniques for marine inorganic carbon parameters (*Dickson et al.*, 2007), existing datasets are severely limited by the ocean's breadth. Inorganic carbon measurements typically come from (1) repeat hydrography cruises which repeat transects approximately once per decade (*Feely et al.*, 2014), (2) ocean time-series sites, such as the Hawaii Ocean Time-series (HOT) and Bermuda Atlantic Time-series Study (BATS), which provide long and well-maintained time-series but no spatial resolution (*Bates et al.*, 2014; *Church et al.*, 2013), and (3) volunteer observing ships (VOSs) which cover vast spatial scales along shipping routes but provide poor temporal resolution (*e.g.*, *Takahashi et al.* (2009)).

Autonomous profiling floats offer a unique opportunity to capture ocean dynamics at significantly higher spatiotemporal resolution. Specifically, the international Argo Program (http://www.argo.ucsd.edu)—a fleet of > 3,500 Lagrangian floats which profile the upper 2,000 m and report near real-time temperature, salinity, and depth data (*Roemmich et al.*, 2009)—provides an ideal platform to drastically improve spatiotemporal resolution of ocean biogeochemical data. Several biogeochemical sensors have been evaluated for use on profiling floats, with oxygen,

nitrate, and optical sensors receiving the most attention to date (*Johnson et al.*, 2009; *Gruber et al.*, 2007; *Tengberg et al.*, 2006; *Johnson and Coletti*, 2002; *Bishop et al.*, 2002; *Bishop et al.*, 2004). pH and pCO_2 sensors designed for use on profiling floats are also under development, but not yet widely implemented (*Johnson et al.*, 2013; *Fiedler et al.*, 2013; *Fietzek et al.*, 2014).

Beyond the spatiotemporal coverage made possible through the Argo Program, the float cycle lends itself well to the analysis of any parameter that requires a finite analysis time due to a rate-limited chemical reaction or diffusion step. The measurement of Dissolved Inorganic Carbon, or DIC ($DIC = [CO_2] + [H_2CO_3] + [HCO_3^-] + [CO_3^{2-}]$) is a prime example of a chemical measurement that would be extremely challenging to carry out at low power at the nominal ~1 Hz required by a moving platform. The incorporation of other wet chemical analyzers on-board profiling floats has proven difficult due to inherent time, volume, and power constraints. Mooring-based DIC analyzers require minutes to a full hour and consume 2-20 mL of reagent to analyze a single sample (*Fassbender et al.*, 2015; *Wang et al.*, 2015; *Liu et al.*, 2013; *Sayles and Eck*, 2009). *Bandstra et al.* (2006) report a comparatively fast-response (6 s e-folding time) underway DIC analyzer but, due to its high sample and carrier gas flow rates (20 and 900 $mL \cdot min^{-1}$, respectively), this technology is not well-suited for adaptation to profiling floats. In general, slowly-responding and reagent-volume-intensive systems do not lend themselves well to mobile platforms. The Micro-Rosette overcomes these two challenges by 1) implementing a true microfluidic sample volume (~100 μL), thereby reducing overall reagent volume and 2) capturing discrete samples *in situ* during

the profiling float's ascent and analyzing them *ex situ* during the float's park cycle, circumventing all issues associated with response time. Critical to the Micro-Rosette concept is the fact that Argo floats remain at their park depth for over one week. The time-intensive and temperature sensitive chemical analysis step of our proposed measurement takes advantage of this prolonged period of mechanical inactivity and thermal stability.

Operating Principles

The Micro-Rosette has three main states, each corresponding to a particular portion of the profiling float cycle: 1) idle/pressure equilibration (during descent), 2) seawater collection (during ascent), and 3) DIC analysis (at park depth). Note that since seawater samples from a given ascent are not analyzed until the float returns to park depth, the Micro-Rosette data transmitted from the surface will be a full cycle behind other sensors onboard the float.

State 1, pressure equilibration, simply opens multiple valves every ten seconds in order to expose the entire system to ambient pressure and therefore relieve pressure gradients inside the Micro-Rosette.

During State 2, the float's ascent from 2,000 m to the surface at approximately 10 $cm \cdot s^{-1}$, the Micro-Rosette receives the profiling float's pressure signal. Upon passing prescribed thresholds, a given valve within the valve manifold (described below) is opened and the seawater pump actuated in order to aspirate a 100 µL seawater sample. The valve is closed once the sample is fully aspirated and the sample pump is primed in preparation for the subsequent sample. This process is repeated for each cell within the

valve manifold (n = 16). Samples are aspirated at 5 $\mu L \cdot s^{-1}$, corresponding to ~2 m vertical resolution for nominal profiling float ascent rates (0.1 m/s). The configuration tested in this work stores unaltered seawater samples. However, as discussed below, the next-generation Micro-Rosette will acidify samples immediately upon collection. A valve manifold is being developed for pre-storage acidification and will be described briefly in the Conclusion.

State 3, DIC analysis, occurs at the float's park depth (*i.e.*, on an isopycnal) and follows the methodology of *Hall and Aller* (1992) and *Sayles and Eck* (2009). Analysis can be further broken down into three main steps: 1) acidification of the seawater sample to convert all inorganic carbon species to CO_2, 2) extraction of the CO_2 from the sample to a dilute sodium hydroxide receiving medium, and 3) detection of the extracted CO_2 in the receiving medium. CO_2 extraction from the seawater sample can be performed in a variety of ways, depending primarily on the detection scheme. The most commonly used form is a liquid-to-gas CO_2 extraction, wherein CO_2 is stripped from an acidified liquid sample by a nitrogen gas stream which carries the CO_2 to an infrared gas analyzer (*Goyet and Snover*, 1993; *O'Sullivan and Millero*, 1998). Alternatively, liquid-to-liquid extraction of CO_2 may be accomplished using a gas diffusion cell (GDC) (*Wang et al.*, 2015; *Liu et al.*, 2013; *Sayles and Eck*, 2009; *Hall and Aller*, 1992; *Martinotti et al.*, 2012); this methodology is examined in detail in Chapter 1 (*Bresnahan and Martz*, (submitted)) and utilized in this work.

Here we describe the mechanical, electrical, and analytical chemical design criteria for the Micro-Rosette. We compare multiple detectors for use in the prototype

and evaluate it through a series of laboratory, test tank, and shipboard deployments. Finally, we discuss remaining modifications necessary to realize successful operation of a Micro-Rosette on a profiling float.

Methods

Reagents

Reagents include 24 mM H_3PO_4 (Mallinckrodt Chemicals 2796-05, Lot J02A06), 7 mM NaOH (Fisher Scientific S318-500, Lot 125708), and Certified Reference Material (CRM) Batch 135 or 139, as noted for each experiment (certified DIC = 2036.96 $\mu mol \cdot kg^{-1}$ or 2023.23 $\mu mol \cdot kg^{-1}$, respectively) obtained from Andrew Dickson's laboratory at Scripps Institution of Oceanography (http://cdiac.esd.ornl.gov/oceans/Dickson_CRM/batches.html). Each is stored in a 3 L Scholle DuraShield bag. $NaHCO_3$ (Fisher Scientific S233-500, Lot 086683) and KCl (Fisher Scientific P217-500, Lot 111342) are also used. 44.2 mM $NaHCO_3$ is used to spike sample solutions, as described below, in order to test the Micro-Rosette's response over a range of sample DIC. KCl solutions ranging from 3.5-20.9 M (0.5-3.0 $mS \cdot m^2 \cdot mol^{-1}$ at 298 K (*Atkins and De Paula*, 2006)) were utilized to evaluate conductivity detectors without running the entire DIC analysis routine.

For bench-top testing, reagents are held 1 m above the Micro-Rosette in order to ensure that the syringe pumps are never pulling against a substantial pressure gradient. During oceanographic deployments, reagent bags were housed in a flooded 15 L plastic storage container which was fastened to the ship's rosette frame as described below.

Micro-Rosette Assembly

The Micro-Rosette components were assembled into test housings for proof-of-concept. The proof-of-concept setup comprises main housings (Figure 2.1): an electronics housing (Figure 2.1b) and a fluidics housing (Figure 2.1c)—connected by six underwater communication and power cables. The principal rationale for utilizing two separate housings for proof-of-concept is that the components within the fluidics housing must be held at ambient pressure in order to avoid creating significant, and likely damaging, pressure gradients across the fluidic circuitry while, contrarily, the components inside the electronics housing, such as the microcontroller, cannot be pressurized. All experiments reported here utilize the bulkier proof-of-concept Micro-Rosette. However, as discussed in the Conclusions, a functional profiling float Micro-Rosette requires repackaging these systems into one or two smaller housings (~ 1-2 L), mated to a float.

The fluidics housing is a 60×31×16.95 cm^3 (31.5 L) aluminum box, filled with silicone oil and connected to an external oil-filled bladder (Xiameter PMX 200 Silicone Fluid, 20 cS) for pressure compensation. The fluidics housing contains all fluidic components required for DIC collection, storage, and analysis: pumps, valves, valve manifold, gas diffusion cell, and conductivity detector. The valve manifold, gas diffusion cell, and conductivity detector are described in detail in the following subsections. Reagents are connected to the fluidics housing via feed-through adapters (IDEX P/N U-500) built into the fluidics housing walls.

The electronics housing, conversely, is a thick aluminum cylindrical pressure housing, held at atmospheric pressure. It contains a 36 V battery pack, microcontroller (a National Instruments sbRIO 9642), the three DC-to-DC power converters required to modulate voltage inputs to the various electronic and fluidic components. The National Instruments sbRIO (single-board Reconfigurable Input/Output) operates LabVIEW software and is used to control all microfluidic components. Two-way communication between the sbRIO and PC was maintained at all times. During a shipboard hydrocast, the Micro-Rosette communicated with the ship's SBE 911plus with which we had constant contact via a PC on deck; during all bench-top and test tank experiments, the Micro-Rosette communicated directly with a PC.

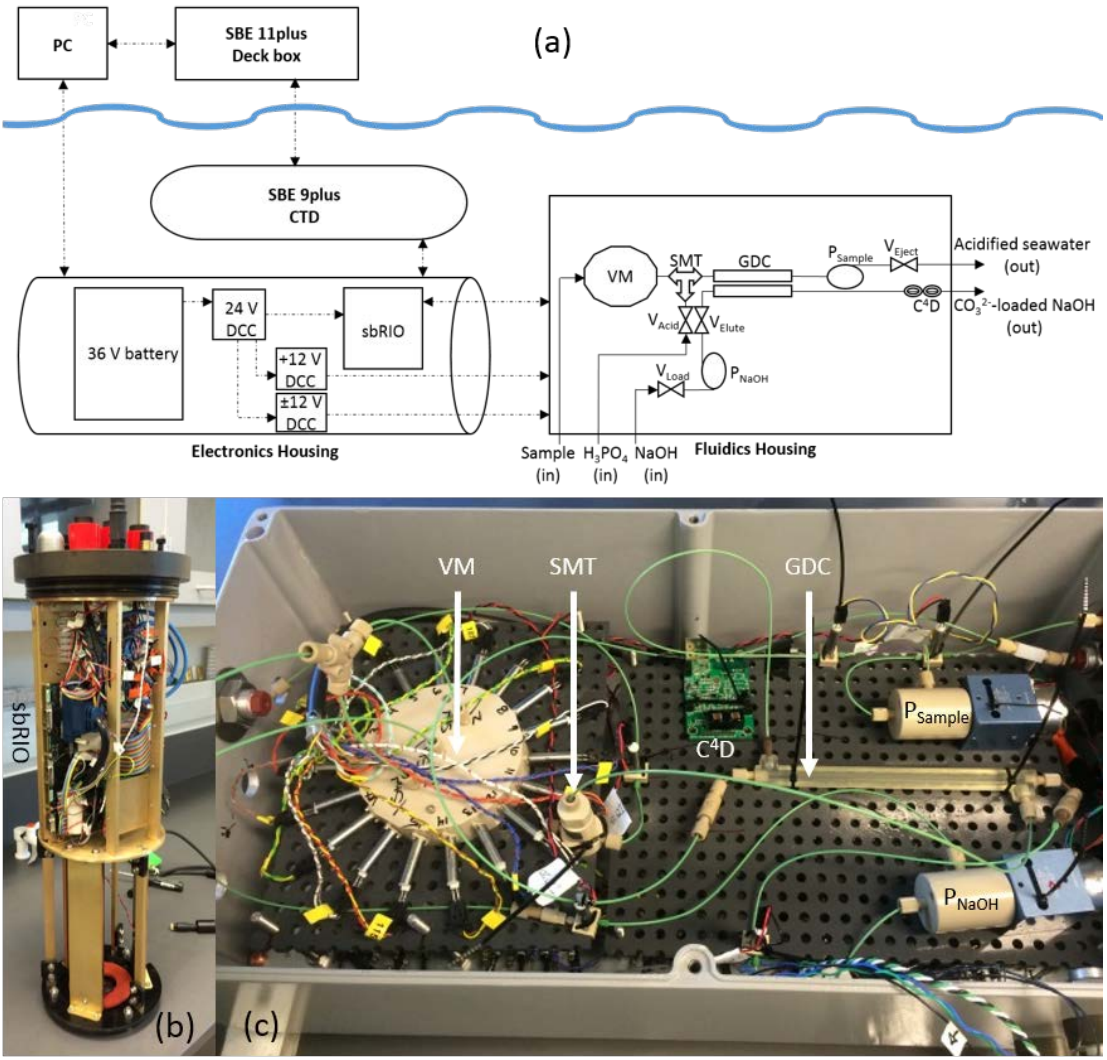

Figure 2.1. (a) Block diagram of prototype Micro-Rosette, (b) electronics, and (c) fluidics housings. In (a), solid and dashed lines denote fluid flow and electrical signals, respectively. PC and SBE 11plus are always in air; fluidics and electronics housings are submerged during test tank and ocean tests. Electronics housing (b) includes: 36 V battery pack (not shown), microcontroller (sbRIO), and 24 V, 12 V, and ±12 V DC-to-DC power converters (DCC, on back side of electronics housing). The fluidics housing (c) encloses the valve manifold (VM), static mixing tee (SMT), gas diffusion cell (GDC), pumps (P_{Sample} and P_{NaOH}), additional solenoid valves (V_{Acid}, V_{Eject}, V_{Load}, and V_{Elute}), static mixing tee (SMT), gas diffusion cell (GDC), and capacitively coupled contactless conductivity detector (C^4D). The valve manifold contains the sixteen sample valves (V_0-V_{15}) as well as two additional valves for incorporation of onboard standards (V_{std1}, V_{std2}). Valves are not labeled in (c) to improve clarity.

Valve Manifold

As the Micro-Rosette ascends through the water column, sixteen discrete samples are collected into the valve manifold (Figure 2.2) at prescribed depths. Seawater is pulled through a common inlet, then through a specified channel by a 750 μL stepper motor-controlled syringe pump (The Lee Co., P/N LPVX0524750B). Channels are selected by opening the solenoid valve (The Lee Co., P/N LFNX0500800B) corresponding to the given channel. The syringe pumps and valves were modified by the manufacturer by drilling a hole through their housings such that the otherwise air-filled cavities are filled with silicone oil for pressure compensation. After filling channels and returning to park depth, the analysis routine begins and each sample is analyzed by sequentially selecting each of the sixteen channels. In addition to the sixteen seawater samples, the valve manifold has two additional inlets for reference seawater-based calibrations. These reference inlets and corresponding valves are not utilized during the ascent/fill routine—only during analysis.

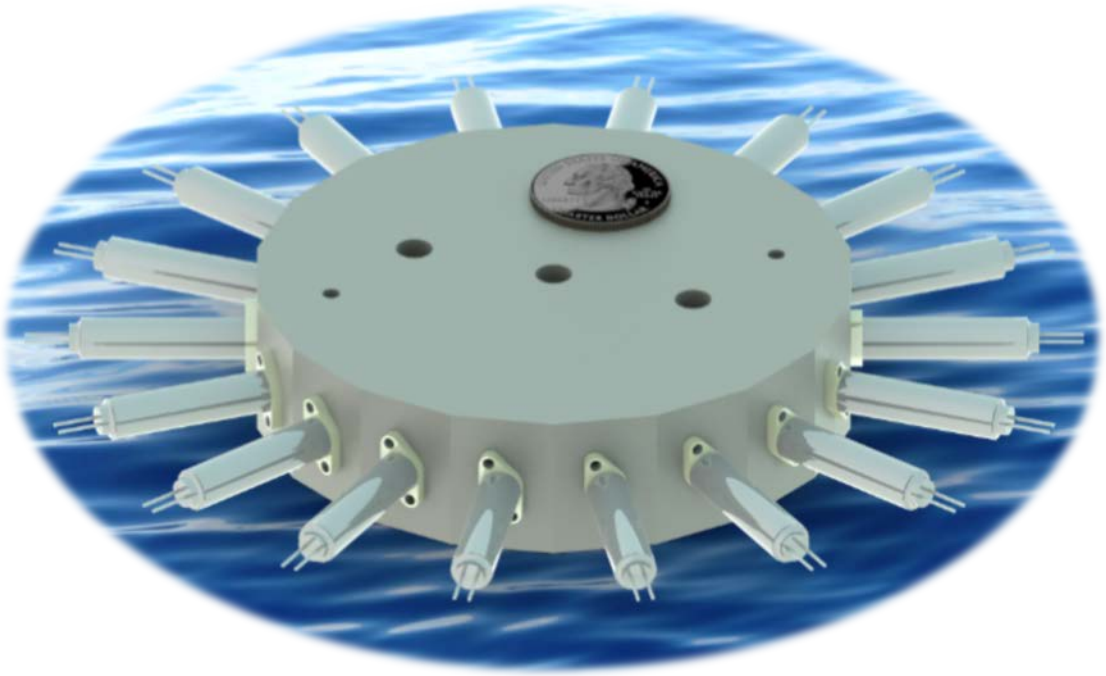

Figure 2.2. Valve manifold. Each valve corresponds to a 100 µL storage cell.

Gas Diffusion Cell

Gas diffusion cells (GDCs) are discussed in depth in Chapter 1; here we use the so-called C1 GDC (Figure 2.3), a cylindrical design with a 0.063" ID and a gas diffusion membrane of 0.025" ID x 0.047" OD Saint-Gobain Standard Bio-Sil tubing. The sample side volume is 150 µL; receiving side volume is 50 µL. In the liquid-to-liquid extraction technique described here, CO_2 diffuses across a gas permeable membrane into a receiving solution of NaOH. CO_2 reacts with OH^- to form predominantly CO_3^{2-} ion:

$$CO_2 + 2OH^- \leftrightarrow H_2O + CO_3^{2-} \quad (1).$$

The limiting conductivity of hydroxide ion is 199.1 $S \cdot cm^2 \cdot equiv^{-1}$ vs. 69.3 $S \cdot cm^2 \cdot equiv^{-1}$ for carbonate (at 25 °C) (*Robinson and Stokes*, 1959).

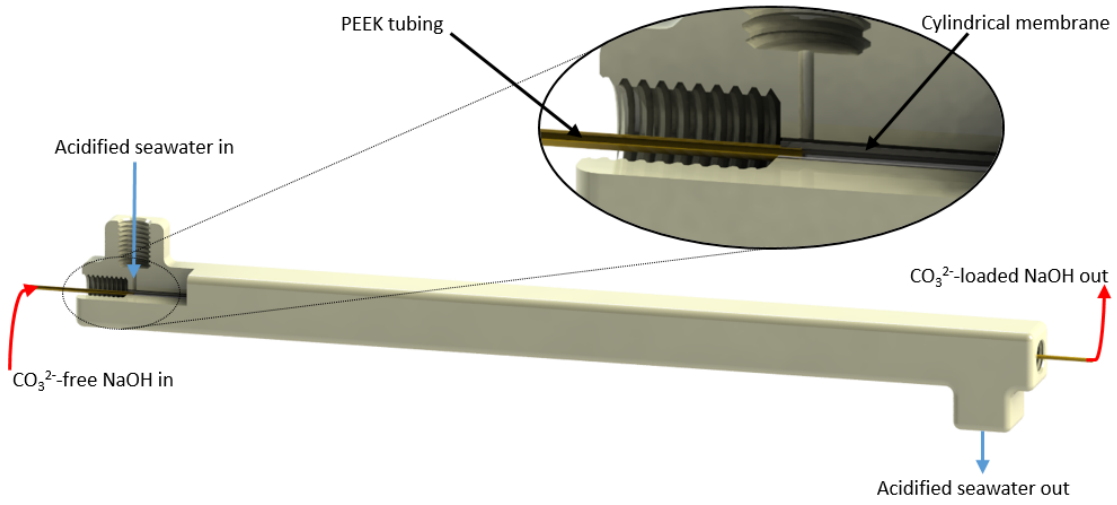

Figure 2.3. Cylindrical GDC. ¼-28 inlet and outlet ports were machined or printed into the manifolds for connections to PEEK tubing. Schematic is cut and magnified to show inner cavity and membrane.

Capacitively Coupled Contactless Conductivity Detector (C^4D)

The change in conductivity is measured with a capacitively coupled contactless conductivity detector (C^4D), the theory of which is described in Chapter 1 and *Francisco and do Lago* (2009); *Guijt et al.* (2004); *Kuban and Hauser* (2008), and references therein. Several C^4Ds ("SIO1," "ER125/ET125," and "ET127") were tested for use in the Micro-Rosette and are briefly described here. All detectors consist of the following components: excitation electronics, detector electronics, the conducting electrodes, and the insulator material. All C^4D results were collected by passing the solution through 1/16" OD, 0.03" ID PEEK tubing with the tubing wall serving as the insulator. While the proof-of-concept Micro-Rosette has 1 detection channel for *n* sample channels, the prototype Micro-Rosette will use a multiplexed design with *n* unique detection channels, to be discussed in the Conclusions.

C^{4}D Impedance Spectroscopy

Impedance spectroscopy refers to the evaluation of a detector over a range or spectrum of input conditions in order to determine the system's total impedance, Z (*e.g.*, sweeping over a range of excitation frequencies and peak-to-peak voltages as well as solution conductivities):

$$Z = \left[\left(\frac{1}{2\pi f \mathrm{c_{w1}}} + \mathrm{R_{NaOH}} + \frac{1}{2\pi f \mathrm{c_{w2}}}\right)^{-1} + 2\pi f \mathrm{c_s}\right]^{-1} \quad (2),$$

where f is frequency of an alternating current (AC) drive signal, c_{w1}, c_{w2}, and c_s are wall 1, wall 2, and stray capacitance, and R_{NaOH} is the resistance of the receiving solution (*i.e.*, NaOH, H_2O, CO_3^{2-}, and HCO_3^-). Wall capacitances refer to the insulating layer of the capillary tubing; stray capacitance depends on the medium (silicone oil in this study) occupying the void space in between the ring electrodes and the outer wall of the tubing.

The first C^{4}D system tested was built in-house and is referred to as SIO1. This device consists of an excitation board (EXB) utilizing direct digital synthesis (DDS) technology to generate programmable 1-10,000 kHz sine waves (SIO1 did not have the ability to tune peak-to-peak voltage; V_{pp} = 1 V). The sine wave was passed to a drive/pickup board (DPB) where it was fed through a multiplexer to a selected channel, based on the water sample being analyzed. This signal then traveled to the drive electrode, through the insulator, analyte, and back through the insulator to the pickup electrode, and ultimately back to the DPB. The received sinusoidal current was converted to a D/C voltage on the DPB and recorded by the sbRIO's analog input channel. The components of both the EXB and DPB were chosen in close consultation

with UCSD's Physics Shop, programmed and evaluated at Scripps, and laid out onto printed circuit boards (PCBs) by the Physics Shop. The drive and pickup electrodes were 5 mm long 1/16" ID copper tubing (McMaster-Carr P/N 8967K86) positioned 3 mm apart, surrounding the 1/16" OD PEEK tubing used to carry the analyte. While SIO1 was designed with sixteen parallel excitation/pickup channel pairs, results using only channel 1 are discussed.

Two additional C^4D designs were evaluated, both manufactured by eDAQ Pty., Ltd. The first, a combination bench-top detector (ER125) and headstage designed to accommodate 1/16" OD PEEK tubing (ET125) was programmable over a range of excitation frequencies (50-1,200 kHz) and peak-to-peak voltages (3-100 V_{pp}). The tests performed with SIO1 (*i.e.*, C^4D measurements on KCl solutions ranging from 3.5-20.9 M) were repeated over the ER125/ET125 combination's full frequency and full voltage ranges. The second eDAQ C^4D (ET127) was custom-designed to meet our specifications: a dynamic range determined by a maximum conductivity of 7 mM NaOH over a range of temperatures, sufficient sensitivity to detect 0.1% differences in typical seawater DIC values, and pressure tolerance to > 2000 dbar. This system is now described at http://wiki.edaq.com/index.php/Measuring_Total_Dissolved_Inorganic_Carbon_of_Seawater_using_Flow_Injection_Analysis_and_C4D. It utilizes a 220 kHz excitation signal in all experiments here, although frequency can be tuned from 20-700 kHz with a set of jumpers on the printed circuit board or an analog voltage input. Peak-to-peak excitation voltage is 5 V; the detector side gain can be amplified with a programmable

gain amplifier (PGA) to 1x, 10x, or 100x, but only 1x is used here. The ET127 was pressure-tested (unpowered) to 2000 dbar in the Scripps Hydraulics Laboratory's pressure chamber. Its electronic performance was reassessed upon incorporation in the Micro-Rosette assembly to demonstrate its pressure tolerance.

Unless otherwise noted, all conductivity analyses were performed using the custom eDAQ C^4D for reasons described below. C^4D voltages are recorded at 10 Hz. Each recorded data point is an average of 1,000 samples, sampled at the sbRIO analog-to-digital converter's (ADC's) maximum frequency of 100 kHz.

DIC Analysis Evaluation Procedure

Utilizing the ET127 for all subsequent experiments, we describe the measurement of seawater DIC. The basic procedure follows Chapter 1 (*Bresnahan and Martz*, (submitted)), with several modifications. Chapter 1 describes single-cell measurements, whereas we evaluate use of the full sixteen valve manifold within the Micro-Rosette assembly here. All experiments here involve filling the full valve manifold prior to beginning analysis in order to mimic the procedure that was implemented during the shipboard hydrocast and will be implemented during deployments onboard profiling floats. After the valve manifold is filled, the analysis cycle begins.

A single measurement cycle consists of the following steps, similar to Chapter 1. Step 1 is unique to the full Micro-Rosette analysis procedure: 1) the valve corresponding to the cell to be analyzed (one of V_0-V_{15}) is opened and the sample pump (P_{sample}) is used to prime the tubing between the valve manifold and static mixing tee

with 84 µL sample. 2) The acid valve (V_{Acid}) is opened, and P_{sample} is used to flush 600 µL acid through the sample side of the system to remove residual CO_2 from previous runs. 3) 900 s diffusion time is given to allow the residual CO_2 to diffuse into the receiving stream. 4) The receiving stream elution valve (V_{Elute}) is opened and the receiving side is flushed with 600 µL NaOH (using P_{NaOH}) to remove all remaining CO_2 from the GDC. 5) The sample valve (same valve from V_0-V_{15} as Step 1) is opened, and a 75 µL aliquot of seawater is pulled into the static mixing tee. 6) V_{Acid} is opened, and 450 µL acid is pulled through the system's sample side, pushing the seawater aliquot through the SMT and loading it into the GDC. 7) CO_2 diffuses across a gas permeable membrane within the GDC into a receiving stream for 900 s. 8) 600 µL acid is flushed through the GDC in order to flush out any remaining CO_2 from the sample side and stop the diffusion. 9) P_{NaOH} and V_{elute} are used to elute the receiving stream (600 µL) through a conductivity detector. This process is repeated for each sample valve in the valve manifold. Each full run through the valve manifold lasts approximately twenty hours. The single-cell DIC measurements described in Chapter 1 and impedance spectroscopy experiments described here consumed the majority of evaluation time; the following proof-of-concept bench-top and test tank experiments were performed in the eight weeks prior to the at-sea tests. Additional laboratory testing will be necessary to fully characterize the system, as discussed in the Conclusions.

Proof-of-Concept Experiments

Bench-Top

The GDC and C^4D were submerged in silicone oil in a jacketed beaker for temperature control by a recirculating water bath (Neslab RTE 7). The temperature of the oil bath was held at 20±0.05 °C (maximum range over multi-day experiments), which eliminated temperature-dependent diffusion and conductivity artifacts. All experiments flush the valve manifold cells with 750 µL sample—far in excess of the entire calculated internal volume of a single path through a single cell (100 µL cell volume + 100 µL inlet tubing volume)—in order to minimize contamination from prior samples in a given cell.

In bench-top experiments, we test the instrument's span, or response over a range of DIC, by spiking the inlet seawater with 750 µL aliquots of 44.2 mM $NaHCO_3$ after a specified number runs (either every other or every fourth run, as described in Results and Discussion). Seawater and $NaHCO_3$ volumes were chosen to increase DIC from the CRM's certified value of 2036.96 to approximately 2500 $\mu mol \cdot kg^{-1}$. In a final bench-top evaluation, we spike the seawater progressively with volumes of $NaHCO_3$ such that the seawater's calculated DIC covers the range expected for the oceanographic deployment to 500 m (described below; data from *Takeshita et al.* (2015)).

Test Tank

We next evaluate the Micro-Rosette's performance in a 6000 L tank of seawater that had been previously filtered and then sterilized by ozonation. Importantly, whereas the GDC and C^4D were previously temperature-controlled in a jacketed beaker during

bench-top tests, during the following experiments, they are contained in the oil-filled fluidics housing, now subject to natural temperature variability. Due to the large mass of water in the test tank, temperature variability during these experiments is determined to be low: < 0.2 °C range during each twenty hour experiment. In the first test tank experiment, no modifications were made to seawater chemistry. In a second experiment, approximately 7 g dry ice ($CO_{2(s)}$) was added to the tank after each of samples 0-12 was collected by the Micro-Rosette. Dry ice was added during the valve manifold filling routine. After each dry ice addition, the Micro-Rosette was idle for twelve minutes to allow the tank to mix. Discrete samples were collected during both experiments and analyzed on a custom NDIR-based DIC analyzer (*O'Sullivan and Millero*, 1998), calibrated with CRM Batch 139. The bench-top analyzer's precision has been determined to be ±3.5 $\mu mol \cdot kg^{-1}$ (standard deviation of replicates).

Figure 2.4. Micro-Rosette fastened to bottom of R/V Sproul's rosette frame, along with 16 Niskin bottles.

At-Sea

The final experiment was a shipboard hydrocast to 500 m. The Micro-Rosette was fastened to the ship's rosette frame (Figure 2.4). The Micro-Rosette communicated with the ship's CTD (SBE 9plus), which was also fastened to the rosette frame, via serial commands and responses, allowing an operator on the ship to trigger the filling of individual Micro-Rosette cells at depths of interest during a roughly two hour profile from 500 m to the surface. Sixteen Niskin bottles were closed at the same depths where Micro-Rosette cells were filled for subsequent comparison. This experiment was designed to come as close as feasible to mimicking a profiling float's routine; however, the rosette stopped at each collection depth for the full time of collection and the Micro-Rosette analysis procedure was performed (unattended) on the ship's deck following the collection profile, not at a "park depth" as would be the case during a float deployment.

Criteria and Figures of Merit

Ultimately, the main evaluation criteria are repeatability of DIC measurements and the ability to characterize the instrument's response across a range of physical conditions (*e.g.*, temperature and depth) and the full range of seawater DIC. Additional criteria pertaining to individual components within the system are described as well.

As in Chapter 1, the analytical signal which quantifies DIC is the integral, or peak area (A), of the trough under the baseline of the elution curve (Step 9 of DIC Analysis Evaluation Procedure). The downward trough in conductivity during elution corresponds to the flushing of carbonate with the baseline corresponding to CO_3^{2-}-free

NaOH. The baseline is calculated as the line that fits two points: the averages of first and last 100 points (10 seconds each) in the elution curve. Where replicates were analyzed, we also report the relative standard deviation (RSD_A), defined as the standard deviation of repeated elution integrals (s_A) divided by their mean ($\bar{A}$) and multiplied by 100%:

$$RSD_A = \frac{s_A}{\bar{A}} \cdot 100\% \quad (3).$$

In order to expedite characterization of the C^4D signal, a series of measurements was made on KCl solutions spanning the expected range of NaOH conductivities encountered during DIC analysis. The advantage of this approach is that it allows a thorough and much more rapid evaluation of the performance limits of the detector without the need to carry out DIC measurements which require many additional steps such as long equilibration time. After measuring the conductivity of a series of KCl solutions, the detector response is converted into a $\%RSD_{C4D}$ in terms of DIC as follows:

$$\%RSD_{C4D} = s_{VC4D} \cdot \frac{\Delta\kappa}{\Delta VC4D} \cdot \frac{\Delta DIC}{\Delta\kappa} \cdot \frac{100\%}{2000\ \mu mol \cdot kg^{-1}} \quad (4),$$

where κ is conductivity and $\frac{\Delta\kappa}{\Delta VC4D}$ is calculated as the slope of solution conductivity vs. C^4D voltage in the neighborhood of 0.7 $mS \cdot cm^{-1}$, the conductivity expected for a 3:1 ratio of seawater to NaOH receiving solution volumes at nominal seawater DIC (2000 $\mu mol \cdot kg^{-1}$) and 20 °C. $\frac{\Delta DIC}{\Delta\kappa}$ is calculated with the conductivity model described by *Sayles and Eck* (2009). $\frac{\Delta DIC}{\Delta\kappa} = 7150 \frac{\mu mol \cdot kg^{-1}}{mS \cdot cm^{-1}}$, again at nominal seawater DIC, and is defined as a constant for these calculations. This methodology implicitly takes into

account the detector's dynamic range at the conductivity of interest; a simple ratio of standard deviation of the electrical signal to its mean would not. All analysis was performed using MATLAB R2014a Student Edition for this proof-of-concept. The prototype Micro-Rosette will perform on-board analysis.

Results and Discussion

C^4D Impedance Spectroscopy Results

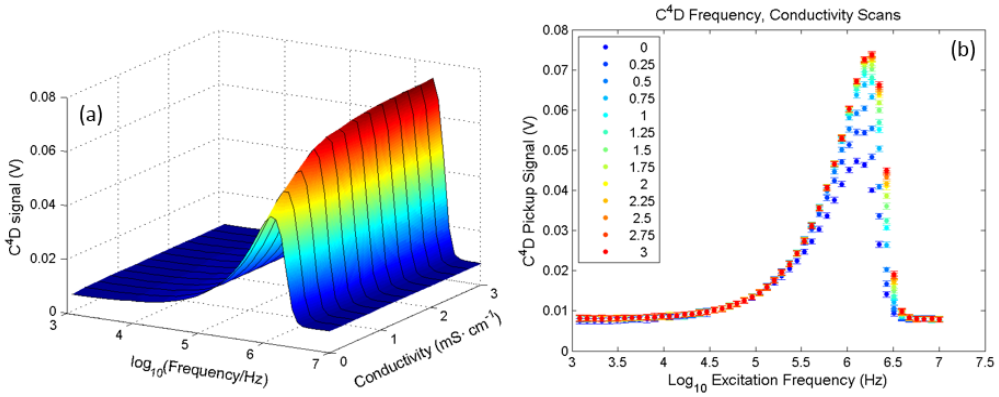

Figure 2.5. (a) SIO1 detector signal across a range of excitation frequencies (10^3-10^7 Hz) and conductivity (0-3 mS·cm^{-1}). Color illustrates C^4D signal and corresponds to C^4D signal range as seen in z-axis. (b) Same, on two-dimensional plot with error bars (±1s.d.) and color in legend representing conductivity (mS·cm^{-1}).

We first evaluate the use of SIO1 using impedance spectroscopy (Figure 2.5). The detector's dynamic range increases substantially at excitation frequencies between 1-3 MHz. This feature is apparent in the increased slope of detector response vs. conductivity at a constant frequency in Figure 2.5a and in the greater range of detector response at constant frequency in Figure 2.5b. The greatest dynamic range, 33.8 mV is found at 1.8 MHz. Detector noise (s_{VC4D} = 0.7 mV) is consistent across all frequency/conductivity conditions, resulting in RSD = 21%, following Equation 5—roughly two full orders of magnitude worse than necessary for this application.

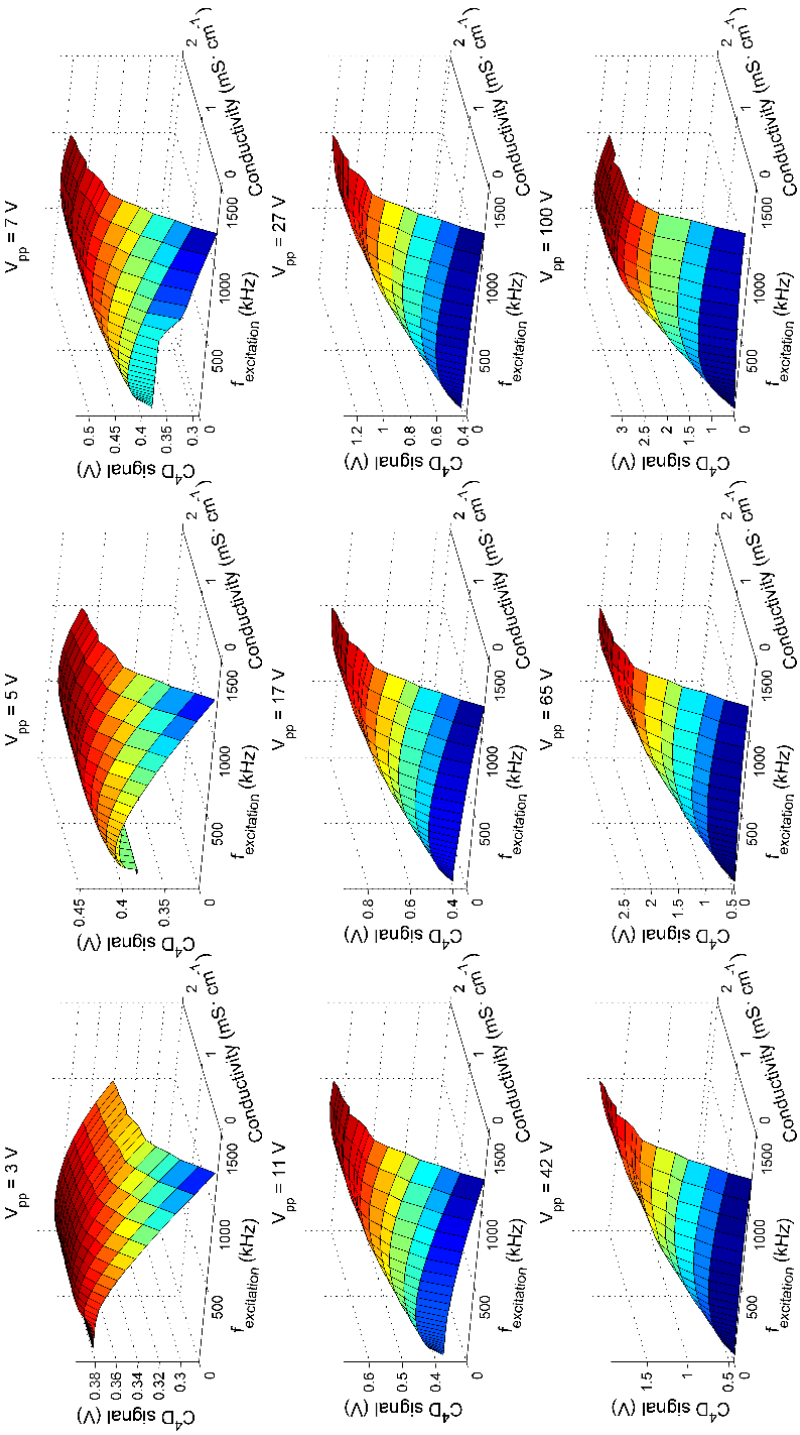

Figure 2.6. Frequency and conductivity scans, as in Figure 2.5, with eDAQ 1/16" C^4D headstage. Excitation voltage is also varied, V_{pp} = 3-100 V. Color illustrates C^4D signal corresponding to range seen in z-axis of each subplot.

Results from the ER125 impedance spectroscopy tests are presented in Figure 2.6 and Table 2. Excitation frequencies as low as 50 kHz were used but resulted in very high $\%RSD_{C4D}$ values; therefore, results at frequencies below 500 kHz are not shown in Table 2, which shows the $\%RSD_{C4D}$ across excitation voltage at the higher end of the excitation frequency range. Generally, as both frequency and voltage increase, the $\%RSD_{C4D}$ improves; however, at the highest voltages/frequency combinations, the C^4D signal saturates, reducing the detector response's linearity and deteriorating the $\%RSD_{C4D}$.

Table 2.1. Theoretical $\%RSD_{C4D}$, calculated using Equation 5, as a function of excitation frequency and peak-to-peak voltage (V_{pp}).

		Frequency (kHz)						
		560	**636**	**722**	**820**	**931**	**1057**	**1200**
Vpp (V)	**3**	71.72%	27.74%	15.53%	10.04%	6.99%	6.14%	5.03%
	5	18.79%	9.52%	5.35%	3.93%	3.03%	2.31%	1.89%
	7	7.77%	5.10%	3.34%	2.46%	2.04%	1.41%	1.26%
	11	4.50%	2.63%	1.92%	1.25%	0.95%	0.83%	0.74%
	17	2.61%	1.62%	1.10%	0.80%	0.62%	0.53%	0.48%
	27	1.62%	0.79%	0.68%	0.50%	0.38%	0.52%	1.04%
	42	2.77%	0.54%	0.41%	0.24%	0.19%	0.17%	0.12%
	65	0.52%	0.42%	0.30%	0.24%	0.16%	0.14%	0.15%
	100	0.47%	0.43%	0.30%	0.31%	0.32%	0.55%	1.00%

Frequency and voltage sweeping with SIO1 and ER125/ET125 systems informed the design of the custom ET127. Factory settings (220 kHz, 5 V peak-to-peak excitation) were never altered and the ET127 performed at better than 0.1% RSD_{C4D} across a range of solution conductivity upon arrival (results not shown). Due to the superiority of the ET127, the SIO1 and ER125/ET125 were retired and all following DIC analyses were carried out with the ET127. The ET127 functioned as expected after submersion to 2000 dbar in the Hydraulics Laboratory pressure chamber, although a

thorough characterization of the pressure dependence of the signal has not been carried out.

Bench-Top Results

Single-cell (*i.e.*, no valve manifold) DIC measurements using the optimized C^4D are described in depth in Chapter 1 (*Bresnahan and Martz,* (submitted)). Here we evaluate the performance of the fully assembled Micro-Rosette. Initial testing assessed the Micro-Rosette's span by spiking the sample solution with $NaHCO_3$ (Figure 2.7). The sample solution's DIC was increased after every-other valve manifold cell was filled (Figure 2.7a). Results indicate that programming and fluidic configuration used in this test captures the increasing DIC, but with a lagging response due to sample carry-over. This lag is evident in that the peak integrals do not exactly track the step changes in DIC but instead ramp up more slowly. In order to more quantitatively assess the duration of this lag, we spiked the sample after every fourth valve manifold cell was filled (Figure 2.7b). Peak integrals stabilize by the third to fourth runs at a given DIC step. In the final bench-top experiment (Figure 2.7c), we spike the sample with $NaHCO_3$ volumes calculated to change DIC to the concentrations expected over a 500 m profile in the Southern California Bight.

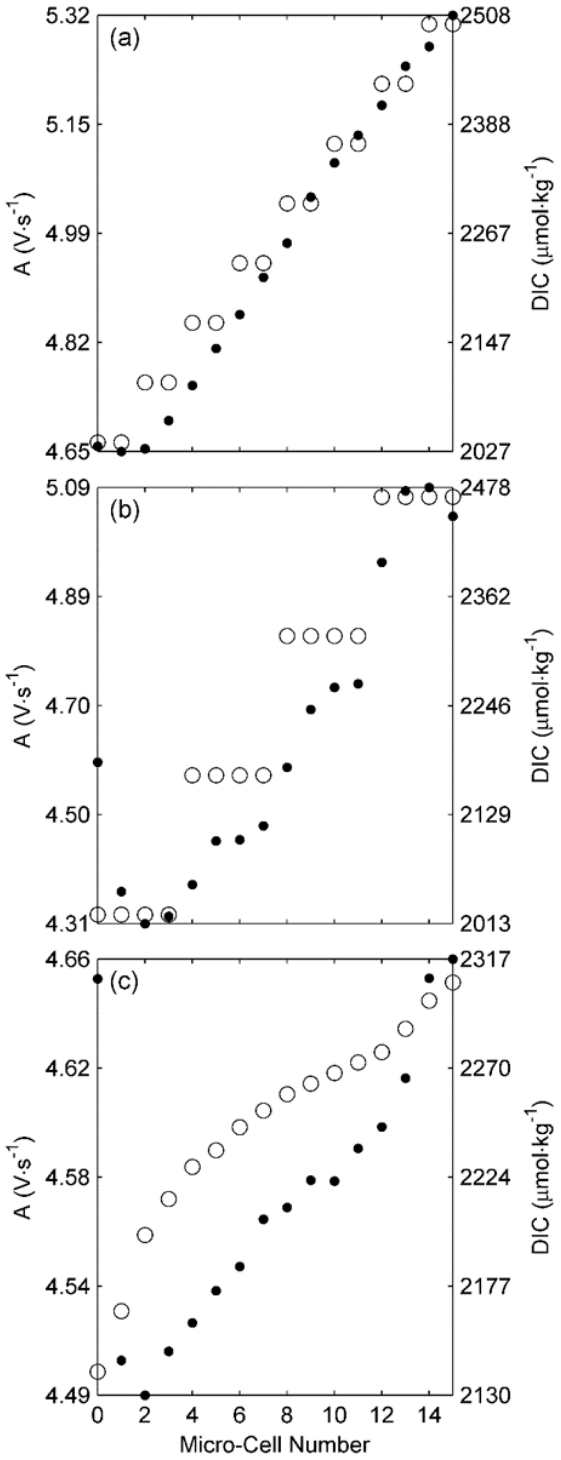

Figure 2.7. Bench-top experiments with $NaHCO_3$ spikes (a) every-other run, (b) every fourth run and (c) every run. Filled circles represent peak integrals, A; open circles are known DIC, calculated from volumetric additions of $NaHCO_3$ to the sample. The range was chosen to mimic a local profile to 500 m.

These bench-top experiments suggest that flush volumes and/or diffusion times during rinse steps are insufficient to remove residual effects from prior samples. Potential carry-over could result from: poor flushing of the SMT or GDC in between runs, GDC "memory" wherein residual CO_2 is adsorbed onto the GDC polymer itself or insufficiently removed from the membrane, and/or contamination among samples within the valve manifold. As discussed in Chapter 1, quantitative transfer of CO_2 from the sample to receiving solution results in superior repeatability; it is also likely that quantitative CO_2 transfer would alleviate any GDC memory effects. Prior to the test tank deployments, the flushing sequence was modified slightly—an additional acid and base rinsing step was added—although due to time constraints prior to the at-sea test, this effect of this modification on carry-over was not carefully characterized on the bench-top.

Test Tank Results

Two experiments were performed in the Scripps Test Tank in order to assess the Micro-Rosette's repeatability and its response to increasing DIC (Figure 2.8). In the first experiment (Figure 2.8a), the tank chemistry was not perturbed. Bench-top NDIR-based analysis of bottles collected during the Micro-Rosette's filling phase resulted in DIC = 2037.5±3.4 $\mu mol \cdot kg^{-1}$—or bench-top analyzer %RSD = 0.17% (n = 9). The Micro-Rosette's response was A = 4.752±0.047 V·s, $\%RSD_A$ = 0.99% (n = 16). Single cell measurements in Chapter 1, for comparison, repeatedly achieved $\%RSD_A < 0.1\%$. The degradation in performance here likely results from slight differences in the valve manifold cells, poorer temperature control in the tank compared to in the jacketed beaker

used on the bench-top, and, perhaps, small natural gradients in the tank. While volume delivery is controlled by a precise syringe pump and small differences in cell geometry shouldn't dominate the signal, additional experiments (not shown) have demonstrated that small cell-to-cell variability does in fact exist and is repeatable, suggesting that each cell needs to be calibrated individually, which was not feasible with the Micro-Rosette's current configuration. This shortcoming will be discussed in the Conclusions section.

Next, $CO_{2(s)}$ was added to the Scripps Test Tank throughout the Micro-Rosette's sample collection phase (Figure 2.8b). The first two bottle sample values were lost due to operator error but the remainder show that the Micro-Rosette responded to the trend in the tank's DIC. A two point calibration (based on a CRM and the last point in Figure 8b) brings the mean difference between bottle and Micro-Rosette to $\Delta DIC = 0.6 \pm 32.5$ $\mu mol \cdot kg^{-1}$, RSD = 1.48% (n = 14). While some of the discrepancy between the Micro-Rosette and bottle samples is attributable to small gradients in the tank created by adding $CO_{2(s)}$, it is likely that the previously described sensor lag accounts for a substantial portion. It can been seen in Figure 2.8b that even after the tank DIC stops increasing (samples 13-15), the Micro-Rosette response continues increasing. It is likely that the anomalously high peak areas in Figure 8b (*e.g.*, samples 4 and 8) are the result of random errors and natural gradients created by the addition of $CO_{2(s)}$.

It is also noteworthy that a full experimental run takes approximately twenty hours; therefore the higher the sample number, the more prone that sample is to contamination via diffusion from other cells in the valve manifold. In an ocean

deployment, biological activity—namely, respiration—could also be an important factor, but it is not expected to play a role in analysis of sterilized tank seawater.

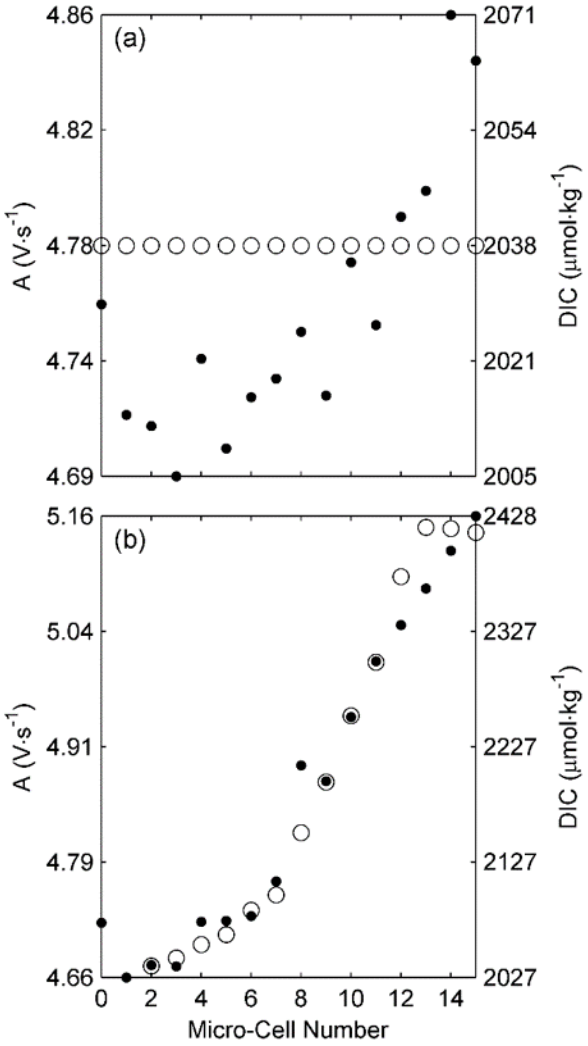

Figure 2.8. Test tank experiments: (a) no modification to tank chemistry and (b) dry ice spike. Filled circles represent peak integrals, A; open circles illustrate tank DIC, measured on bottles. Micro-Cell Number is the number within the valve manifold cell being analyzed.

An additional feature observed in all Micro-Rosette experiments (Figure 2.7 and Figure 2.8) is that the first run of each has a higher peak integral than the subsequent run, even though in all experiments, DIC was either maintained throughout or increased as a function of sample number, theoretically mandating that the first peak integral be

either identical or lower—but never higher—than subsequent runs. We hypothesize that this inflated first peak integral results from the short time between the filling and analysis routines: as the Micro-Rosette cells are filled, seawater is constantly flowing across the GDC and transferring CO_2 to the membrane and receiving side. Prior to beginning the analysis cycle, the GDC is flushed with acid and base on sample and receiving sides, respectively, but these anomalously high initial peaks suggest that the flush volume and/or flush time were insufficient to clear the GDC of residual CO_2 from the filling cycle.

At-Sea Results

The last Micro-Rosette evaluation reported here was the shipboard hydrocast to 500 m. Throughout this deployment, the Micro-Rosette communicated with the ship's SBE 11plus, thereby indicating proper mechanical and electrical operation from 500 m to the surface. This accomplishment alone made the shipboard measurements a worthwhile, however, the samples captured during this test were compromised during the on-deck analysis period due to an air bubble trapped in the receiving side flow path. This unfortunate circumstance likely resulted from an air bubble in the NaOH reagent inlet bag resulting from the repeated assembly and disassembly of the Micro-Rosette while the system was fastened to the ship's rosette. Admittedly, the ocean deployment was not a 100% success, yet it generated a tremendous amount of useful information that will help move the Micro-Rosette project forward. For example, the hydrocast provides the first solid results establishing that all of the components in the fully assembled Micro-Rosette work mechanically to at least 500 m. Furthermore, we do not

expect air bubbles to play a significant role in the future as the Micro-Rosette will remain fully submerged for its deployment lifetime on profiling floats and better care will be taken to ensure the removal of air pockets from reagent bags prior to subsequent deployments.

Conclusions

The proof-of-concept tests for the Micro-Rosette successfully captured and sequentially analyzed sixteen discrete 100 µL seawater samples in bench, tank, and at-sea tests. While the precision and accuracy of (1% and 1.5%, respectively) are unsatisfactory for "climate-quality" marine inorganic carbon datasets, the progress made on single channel measurements (Chapter 1) demonstrate that a future prototype version of the Micro-Rosette should be able to approach 0.1% repeatability and precision. The Micro-Rosette shows great promise for resolving event-scale phenomena (*e.g.*, phytoplankton blooms), seasonal cycles, and upper ocean profiles, all of which regularly change DIC in excess of tens to hundreds of $\mu mol \cdot kg^{-1}$ over the respective time and space scales within which the Micro-Rosette is designed to function. We expect that with this foundation, progress can be made quickly toward improving the system's %RSD and calibration.

In order to successfully operate on a profiling float, it is evident that both cell-to-cell variability and response lag must be addressed. In order to minimize cell-to-cell variability, it will be necessary to calibrate each cell independently with integrated standards. Response lag results from what appears to be system memory, perhaps due to CO_2 adsorption onto the GDC's polymeric walls or poor flushing of the silicone

membrane itself. Alternatively, the fluidic circuitry could have poorly flushed “dead volumes,” such as in the mixing tee or diffusion cell. Future experiments will increase reagent flush volumes and diffusion times in order to determine if this memory effect can be resolved by varying easily-tuned experimental parameters. Diffusion time for experiments described here was selected based on results from Chapter 1, wherein it was determined that especially at lower sample volumes (< 100 µL), increasing diffusion time improves %RSD. Due to time constraints (a proof-of-concept deployment cruise deadline), it was not possible to vary diffusion time to significantly longer periods during the multichannel tests, but future testing will increase diffusion time in an attempt to alleviate the GDC memory effect through quantitative CO_2 transfer from sample to receiving solution.

One of the primary lessons learned from the results presented here is that separate collection and diffusion stages within the Micro-Rosette is problematic, especially since samples are exposed to each other through common inlet and outlet ports. During a profile such as the one shown in Figure 2.8b, samples with DIC differences of > 400 $\mu mol \cdot kg^{-1}$ coexist within the valve manifold, creating substantial gradients and, therefore, potential for cross-sample diffusion/contamination. A new single collection and diffusion manifold has been designed to overcome this challenge (Figure 2.9). The design, already fabricated via 3D printing but not yet evaluated, allows for immediate acidification of samples as they are collected during the Micro-Rosette’s profile. Samples are then stored within a multiplexed gas diffusion cell—that is, one GDC per sample collected—allowing for CO_2 transfer to begin immediately upon

sample collection. Samples are acidified immediately upon collection (such that a low pH sample is stored in contact with a fresh solution of NaOH until analysis at park depth) or during the park/analysis routine, which could be as long as twenty-four hours after collection. It is preferable to acidify immediately in order to halt biological activity within the sample; furthermore, it has been shown that immediate sample acidification of seawater samples in DIC analyzers reduces biofouling (*Liu et al.*, 2013). As the initial valve manifold design did not allow for pre-storage acidification, results from the latter technique are described here.

This new design will lead to additional complications, such as: 1) an increased number of failure points due to the necessity of assembling more diffusion membranes, which have occasionally proven difficult to seal 2) and a different calibration routine due to the fact that seawater is metered volumetrically but collected across significant density changes. The volumetric seawater collection is not an issue in the current design due to the fact that more seawater is collected during profiling than is used during analysis. Analysis in the current design is also performed using volumetric additions, but on an isopycnal, such that seawater mass delivered to the GDC should be identical from cell to cell. Contrarily, in the multiplexed design, all collected seawater is necessarily analyzed, meaning that there will be differences in seawater mass (and therefore moles of DIC, even if concentration ($\mu mol \cdot kg^{-1}$) across multiple samples is identical) delivered to the GDC. However, we suspect that the effect of mass difference will be a second order effect that can be addressed once a functional prototype begins capturing data in the field at sites with well-known vertical structure (e.g. HOT, BATS).

We therefore feel that the added complexity is necessary and will result in improved accuracy, resulting from reduced cross-sample contamination and the ability to carefully calibrate each cell with onboard standards. Ultimately, we intend to incorporate a multiplexed C^4D as well, such that all sample and receiving solution streams remain separated throughout, further increasing complexity but reducing contamination. As in Chapter 1, the relatively recent ability to print these parts is key to the success of the multiplexed prototype envisioned.

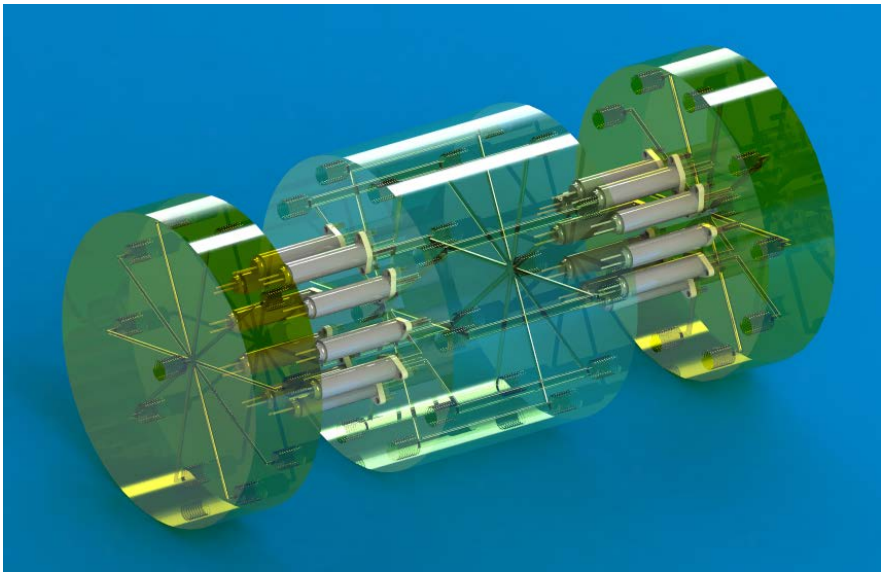

Figure 2.9. The Micro-Rosette manifold used to multiplex seawater collection, acidification, and diffusion. This design implements ten distinct, radially-symmetric storage/diffusion cells with common pumps and a detector. Later designs may be expanded several-fold to provide greater vertical sampling resolution.

Finally, we illustrate the concept of a prototype Micro-Rosette utilizing the multiplexed GDC attached to a SOLO II float (Figure 2.10). Future versions would integrate all systems shown into a single housing, but results described here and this next design represent a large step forward for marine inorganic carbon monitoring.

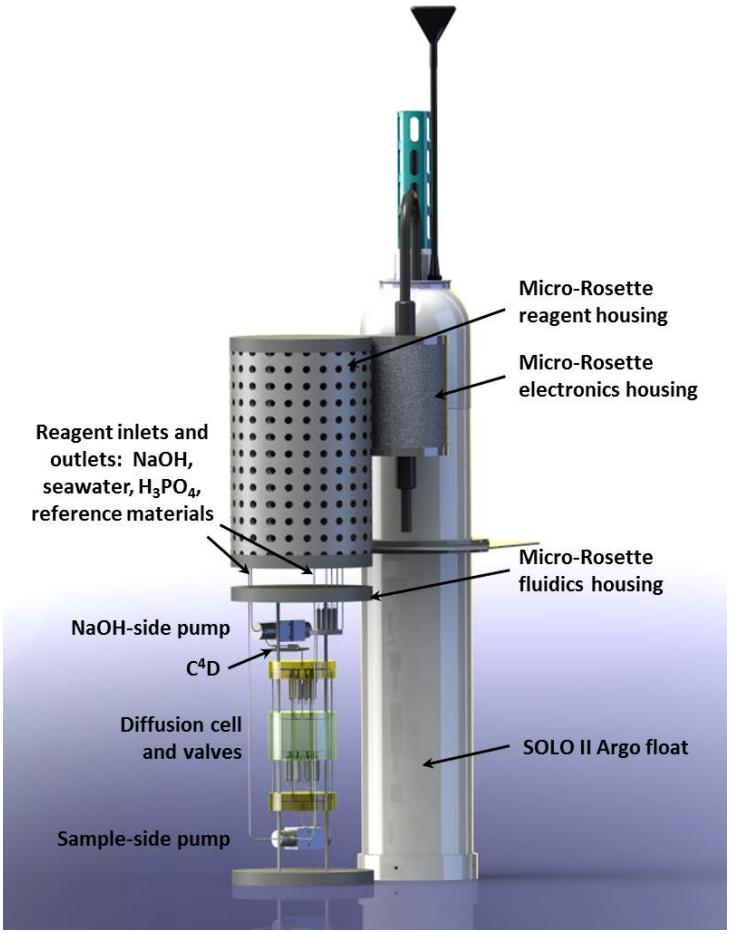

Figure 2.10. Conceptual schematic of the Micro-Rosette integrated into a profiling float. For scale, the SOLO-II has an overall length of 1.3 m (4'4"). For the prototype shown, the float is modified as little as possible. Fluidics housing is shown without external encasement in order to detail internal components.

Acknowledgements

This work was supported by NSF-OCE 0961250. PJB was supported by the Department of Defense (DoD) through the National Defense Science and Engineering Graduate (NDSEG) Fellowship Program.

Chapter 2, in part, is currently being prepared for submission for publication of the material. Bresnahan, P.J., Martz, T.R., de Almeida, J.L., Maguire, P., Ward, B. The dissertation author was the primary investigator and author of this material.

References

IPCC, 2013 Climate Change 2013: The Physical Science Basis. Contribution of Working Group I to the Fifth Assessment Report of the Intergovernmental Panel on Climate Change. 1535.

Takahashi, T., Sutherland, S. C., Wanninkhof, R., Sweeney, C., Feely, R. A., Chipman, D. W., Hales, B., Friederich, G., Chavez, F., Sabine, C., Watson, A., Bakker, D. C. E., Schuster, U., Metzl, N., Yoshikawa-Inoue, H., Ishii, M., Midorikawa, T., Nojiri, Y., Körtzinger, A., Steinhoff, T., Hoppema, M., Olafsson, J., Arnarson, T. S., Tilbrook, B., Johannessen, T., Olsen, A., Bellerby, R., Wong, C. S., Delille, B., Bates, N. R. and de Baar, H. J. W., 2009 Climatological mean and decadal change in surface ocean pCO2, and net sea–air CO2 flux over the global oceans. *Deep Sea Research Part II: Topical Studies in Oceanography*, 56, 554-577. doi:10.1016/j.dsr2.2008.12.009

Ciais, P., Sabine, C., Bala, G., Bopp, L., Brovkin, V., Canadell, J., Chhabra, A., DeFries, R., Galloway, J., Heimann, M., Jones, C., Quéré, C. L., Myneni, R. B., Piao, S. and Thornton, P., 2013 Carbon and Other Biogeochemical Cycles. *Climate Change 2013: The Physical Science Basis. Contribution of Working Group I to the Fifth Assessment Report of the Intergovernmental Panel on Climate Change*, 465–570. doi:10.1017/CBO9781107415324.015

Ducklow, H. W. and Doney, S. C., 2013 What is the metabolic state of the oligotrophic ocean? A debate. *Ann Rev Mar Sci*, 5, 525-33. doi:10.1146/annurev-marine-121211-172331

Williams, P. J., Quay, P. D., Westberry, T. K. and Behrenfeld, M. J., 2013 The oligotrophic ocean is autotrophic. *Ann Rev Mar Sci*, 5, 535-49. doi:10.1146/annurev-marine-121211-172335

Duarte, C. M., Regaudie-de-Gioux, A., Arrieta, J. M., Delgado-Huertas, A. and Agusti, S., 2013 The oligotrophic ocean is heterotrophic. *Ann Rev Mar Sci*, 5, 551-69. doi:10.1146/annurev-marine-121211-172337

Bockmon, E. E. and Dickson, A. G., 2015 An inter-laboratory comparison assessing the quality of seawater carbon dioxide measurements. *Marine Chemistry*, 171, 36-43. doi:10.1016/j.marchem.2015.02.002

Dickson, A. G., Sabine, C. L. and Christian, J. R., 2007 Guide to best practices for ocean CO2 measurements. *PICES Special Publication 3*, 191.

Feely, R. A., L. D. Talley, J. L. Bullister, C. A. Carlson, S. C. Doney, R. A. Fine, E. Firing, N. Gruber, D. A. Hansell, G. C. Johnson, R. M. Key, C. Langdon, A. Macdonald, J. T. Mathis, S. Mecking, F. J. Millero, C. W. Mordy, C. L. Sabine, W. M. Smethie, J. H. Swift, A. M. Thurnherr, R. H. Wanninkhof and Warner, M. J., 2014 The US Repeat Hydrography CO2/Tracer Program (GO-SHIP): Accomplishments from the first decadal survey. A US CLIVAR and OCB Report. 47.

Bates, N., Astor, Y., Church, M., Currie, K., Dore, J., Gonaález-Dávila, M., Lorenzoni, L., Muller-Karger, F., Olafsson, J. and Santa-Casiano, M., 2014 A Time-Series View of Changing Ocean Chemistry Due to Ocean Uptake of Anthropogenic CO2 and Ocean Acidification. *Oceanography*, 27, 126-141. doi:10.5670/oceanog.2014.16

Church, M. J., Lomas, M. W. and Muller-Karger, F., 2013 Sea change: Charting the course for biogeochemical ocean time-series research in a new millennium. *Deep Sea Research Part II: Topical Studies in Oceanography*, 93, 2-15. doi:10.1016/j.dsr2.2013.01.035

Roemmich, D., Johnson, G., Riser, S., Davis, R., Gilson, J., Owens, W. B., Garzoli, S., Schmid, C. and Ignaszewski, M., 2009 The Argo Program: Observing the Global Oceans with Profiling Floats. *Oceanography*, 22, 34-43. doi:10.5670/oceanog.2009.36

Johnson, K. S., Berelson, W. M., Boss, E., Chase, Z., Claustre, H., Emerson, S. R., Gruber, N., Kortzinger, A., Perry, M. J. and Riser, S. C., 2009 Observing biogeochemical cycles at global scales with profiling floats and gliders prospects for a global array. *Oceanography*, 22, 216-225. doi:10.5670/oceanog.2009.81

Gruber, N., Doney, S., Emerson, S., Gilbert, D., Kobayashi, T., Körtzinger, A., Johnson, G., Johnson, K., Riser, S. and Ulloa, O., 2007 The ARGO-Oxygen Program-A white paper to promote the addition of oxygen sensors to the international Argo float program.

Tengberg, A., Hovdenes, J., Andersson, H. J., Brocandel, O., Diaz, R., Hebert, D., Arnerich, T., Huber, C., Körtzinger, A., Khripounoff, A., Rey, F., Rönning, C., Schimanski, J., Sommer, S. and Stangelmayer, A., 2006 Evaluation of a lifetime-based optode to measure oxygen in aquatic systems. *Limnology and Oceanography: Methods*, 4, 7-17. doi:10.4319/lom.2006.4.7

Johnson, K. S. and Coletti, L. J., 2002 In situ ultraviolet spectrophotometry for high resolution and long-term monitoring of nitrate, bromide and bisulfide in the ocean. *Deep Sea Research Part I: Oceanographic Research Papers*, 49, 1291-1305. doi:10.1016/S0967-0637(02)00020-1

Bishop, J. K. B., Davis, R. E. and Sherman, J. T., 2002 Robotic Observations of Dust Storm Enhancement of Carbon Biomass in the North Pacific. *Science*, 298, 817-821. doi:10.1126/science.1074961

Bishop, J. K. B., Wood, T. J., Davis, R. E. and Sherman, J. T., 2004 Robotic Observations of Enhanced Carbon Biomass and Export at 55°S During SOFeX. *Science*, 304, 417-420. doi:10.1126/science.1087717

Johnson, K. S., Jannasch, H. W., Coletti, L. J., Carlson, R., Brown, G., Nohava, T., Martz, T. R., Takeshita, Y., Swift, D. and Riser, S. C., 2013 Towards a global ocean pH observing system: First observations with Deep-Sea Durafet pH sensors on profiling floats. *ASLO Aquatic Sciences Meeting*.

Fiedler, B., Fietzek, P., Vieira, N., Silva, P., Bittig, H. C. and Körtzinger, A., 2013 In Situ CO2 and O2 Measurements on a Profiling Float. *Journal of Atmospheric and Oceanic Technology*, 30, 112-126. doi:10.1175/jtech-d-12-00043.1

Fietzek, P., Fiedler, B., Steinhoff, T. and Körtzinger, A., 2014 In situ Quality Assessment of a Novel Underwater pCO2 Sensor Based on Membrane Equilibration and NDIR Spectrometry. *Journal of Atmospheric and Oceanic Technology*, 31, 181-196. doi:10.1175/JTECH-D-13-00083.1

Fassbender, A. J., Sabine, C. L., Lawrence-Slavas, N., De Carlo, E. H., Meinig, C. and Maenner Jones, S., 2015 Robust sensor for extended autonomous measurements of surface ocean dissolved inorganic carbon. *Environ Sci Technol*, 49, 3628-35. doi:10.1021/es5047183

Wang, Z. A., Sonnichsen, F. N., Bradley, A. M., Hoering, K. A., Lanagan, T. M., Chu, S. N., Hammar, T. R. and Camilli, R., 2015 In Situ Sensor Technology for Simultaneous Spectrophotometric Measurements of Seawater Total Dissolved Inorganic Carbon and pH. *Environmental Science & Technology*, 49, 4441-4449. doi:10.1021/es504893n

Liu, X., Byrne, R. H., Adornato, L., Yates, K. K., Kaltenbacher, E., Ding, X. and Yang, B., 2013 In situ spectrophotometric measurement of dissolved inorganic carbon in seawater. *Environ Sci Technol*, 47, 11106-14. doi:10.1021/es4014807

Sayles, F. L. and Eck, C., 2009 An autonomous instrument for time series analysis of TCO2 from oceanographic moorings. *Deep Sea Research Part I: Oceanographic Research Papers*, 56, 1590-1603. doi:10.1016/j.dsr.2009.04.006

Bandstra, L., Hales, B. and Takahashi, T., 2006 High-frequency measurements of total CO2: Method development and first oceanographic observations. *Marine Chemistry*, 100, 24-38. doi:10.1016/j.marchem.2005.10.009

Hall, P. J. and Aller, R. C., 1992 Rapid, small-volume, flow injection analysis for SCO2, and NH4+ in marine and freshwaters. *Limnology and Oceanography*, 37, 1113-1119. doi:10.4319/lo.1992.37.5.1113

Goyet, C. and Snover, A. K., 1993 High-accuracy measurements of total dissolved inorganic carbon in the ocean: comparison of alternate detection methods. *Marine Chemistry*, 44, 235-242. doi:10.1016/0304-4203(93)90205-3

O'Sullivan, D. W. and Millero, F. J., 1998 Continual measurement of the total inorganic carbon in surface seawater. *Marine Chemistry*, 60, 75-83. doi:10.1016/S0304-4203(97)00079-0

Martinotti, V., Balordi, M. and Ciceri, G., 2012 A flow injection analyser conductometric coupled system for the field analysis of free dissolved CO2 and total dissolved inorganic carbon in natural waters. *Anal Bioanal Chem*, 403, 1083-93. doi:10.1007/s00216-012-5762-8

Bresnahan, P. J. and Martz, T. R., (submitted) Characterization of gas diffusion cell geometry for a microfluidic dissolved inorganic carbon analyzer.

Atkins, P. and De Paula, J., 2006 Physical Chemistry, Eighth Edition.

Robinson, R. A. and Stokes, R. H., 1959 Electrolyte Solutions (2nd Revised Edition); Appendix 6.1.

Francisco, K. J. and do Lago, C. L., 2009 A compact and high-resolution version of a capacitively coupled contactless conductivity detector. *Electrophoresis*, 30, 3458-64. doi:10.1002/elps.200900080

Guijt, R. M., Evenhuis, C. J., Macka, M. and Haddad, P. R., 2004 Conductivity detection for conventional and miniaturised capillary electrophoresis systems. *Electrophoresis*, 25, 4032-57. doi:10.1002/elps.200406156

Kuban, P. and Hauser, P. C., 2008 A review of the recent achievements in capacitively coupled contactless conductivity detection. *Anal Chim Acta*, 607, 15-29. doi:10.1016/j.aca.2007.11.045

Takeshita, Y., Frieder, C. A., Martz, T. R., Ballard, J. R., Feely, R. A., Kram, S., Nam, S., Navarro, M. O., Price, N. N. and Smith, J. E., 2015 Including high frequency variability in coastal ocean acidification projections. *Biogeosciences Discuss.*, 12, 7125-7176. doi:10.5194/bgd-12-7125-2015

CHAPTER 3: BEST PRACTICES FOR AUTONOMOUS MEASUREMENT OF SEAWATER PH WITH THE HONEYWELL DURAFET

Methods in Oceanography 9 (2014) 44–60

Contents lists available at ScienceDirect

Methods in Oceanography

journal homepage: www.elsevier.com/locate/mio

Full length article

Best practices for autonomous measurement of seawater pH with the Honeywell Durafet

Philip J. Bresnahan Jr.[a], Todd R. Martz[a,*], Yuichiro Takeshita[a], Kenneth S. Johnson[b], Makaila LaShomb[a]

[a] Scripps Institution of Oceanography, University of California San Diego, 9500 Gilman Drive, La Jolla, CA 92093, USA

[b] Monterey Bay Aquarium Research Institute, 7700 Sandholdt Road, Moss Landing, CA 95039, USA

GRAPHICAL ABSTRACT

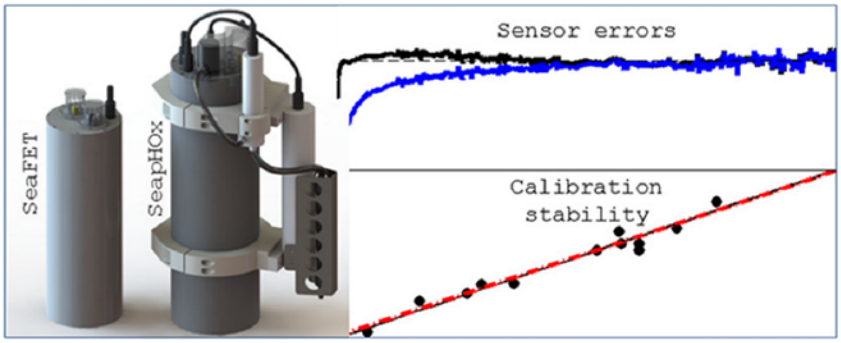

ARTICLE INFO

Article history:
Received 18 April 2014
Received in revised form
20 August 2014
Accepted 25 August 2014

ABSTRACT

Performance of autonomous pH sensors is evaluated by comparing *in situ* data to independent bench-top measurements of pH and to co-located pH, O_2, and pCO_2 sensors. While the best practice is always to deploy a properly calibrated sensor, the lengthy time period required for sensor conditioning and calibration often results in sensor deployment without comprehensive calibration. Quality control (QC) procedures are examined to determine the errors

* Corresponding author. Tel.: +1 858 534 7466.
E-mail address: trmartz@ucsd.edu (T.R. Martz).

http://dx.doi.org/10.1016/j.mio.2014.08.003

Keywords:
pH
Sensor
Calibration
ISFET
Acidification

associated with different *in situ* calibration approaches and lay a framework for best practices. Sensor packages employing the Honeywell Durafet remained stable across multiple deployments for over nine months. However, sensor performance was often limited by biofouling. Regional empirical relationships for estimating carbonate system parameters are shown to enable identification of otherwise indistinguishable sensor offset and drift when multiple sensor types are co-located. Uncertainty is determined by calibration approach and must be quantified on a case-by-case basis. Our results indicate that the Durafet is capable of accuracy, relative to a chosen reference, of better than 0.03 pH units over multiple months. Accuracy is improved when a robust shore-side calibration is performed, an independent means of QC is available throughout a deployment, and effective biofouling prevention measures are taken.

1. Introduction

A recent trend in ocean acidification (OA) research involves utilizing natural settings in order to incorporate the variability inherent in nature (Hofmann et al., 2011; Kline et al., 2012). Although Standard Operating Procedures (SOPs) have been established for CO_2 bottle analyses (Dickson, 2007) and laboratory-based OA experiments (Riebesell et al., 2010), no standard protocols are in place for calibration and validation of the sensors used to characterize the natural settings of *in situ* experiments, despite their increasing prevalence (e.g. Byrne et al., 2009; Cullison Gray et al., 2011; Easley et al., 2013; Frieder et al., 2012; Liu et al., 2006; Martz et al., 2010; Seidel et al., 2008; Yu et al., 2011). In addition to OA studies, a number of equally important applications for quantitative biogeochemical studies exist for pH sensors (e.g. Emerson et al., 2011; Martz et al., 2014) that would benefit from documented validation and quality control (QC) protocols. Furthermore, pH measurements used to investigate specific processes – from climate trends to organismal responses – should always carry a statement of the uncertainty in the number reported. Establishing data QC protocols is of paramount importance and must be addressed before the relationship between observed pH and biogeochemical thresholds or biological "tipping points" is reported.

The initial accuracy of a stable sensor is limited by the calibration approach. Trust in pre- and post-calibrations (i.e., setting calibration constants before sensors are deployed or after they are recovered) of any marine chemical sensor relies on two hard to satisfy criteria: (1) sensors must be calibrated in a similar physical setting (*viz.*, similar temperature, salinity, pressure) to that of the study location and (2) sensors must not undergo significant (re)conditioning in their new environments. It is always preferred to rigorously calibrate a sensor before deployment, but this may require facilities and time that are not available. Honeywell provides an initial factory calibration of every Durafet sensor on the NBS pH scale, but provides no statement of calibration accuracy or stability, recommending that the user perform the canonical NBS buffer standardization employed widely for all glass electrodes. Because the NBS pH scale is not recommended for seawater pH measurements (Marion et al., 2011), at minimum, the Honeywell factory calibration must be recalibrated on the appropriate pH scale (e.g., the seawater scale, total hydrogen ion scale) before use in most oceanographic applications. Examples of such conversions are provided in the Supplementary data (see Appendix A). Due to these complications, it is sometimes preferred to calibrate an operating Durafet to a field measurement after the sensor is deployed. This practice also serves to validate laboratory calibration. Clearly, the calibration sample must coincide in time and space with a sensor measurement—a challenging demand in dynamic environments. Here, we evaluate the utility of *in situ* calibrations via bottle samples as well as independent, co-located sensors linked through regional empirical relationships.

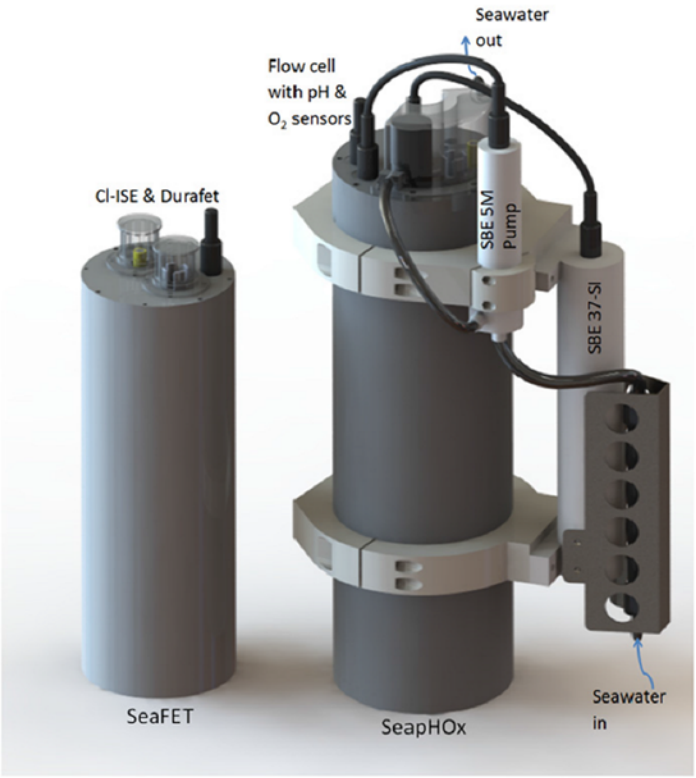

Fig. 1. SeaFET and SeapHOx sensor packages.

Specifically, we utilize the relationships derived by Alin et al. (2012) who report estimates for marine inorganic carbon parameters below the mixed layer in the CalCOFI Sampling Region (27°*N*–37°*N*) based on oxygen, temperature, salinity, and density.

While a sensor with a self-calibrating mechanism is desirable for obvious reasons, such systems are quite rare due to the complexity of automating the calibration process. The MAPCO$_2$ is currently the only sensor capable of measuring a CO_2 system variable with self-calibration (Friederich et al., 1995). The Durafet's demonstrated stability and longevity (Martz et al., 2010, present study) warrant its continued use without self-calibration capability and heeding the recommendations set forth here will likely augment data quality for the Durafet and other systems with no self-calibration. Based on a number of deployment examples, we outline a set of best practices that we have found useful for rejecting bad data and estimating uncertainty. The analysis techniques and recommendations described will prove helpful for the ocean chemical sensor community at large and Durafet sensor users in particular.

2. Materials and methods

2.1. Sensors

Ion Sensitive Field Effect Transistor (ISFET) pH sensors used in this work were deployed in a variety of configurations. The "SeaFET" design consists of a Honeywell Durafet and a solid-state chloride ion selective electrode (Cl-ISE) (Martz et al., 2010) whereas the "SeapHOx" is an integrated sensor package consisting of a Durafet, Cl-ISE, oxygen sensor (Aanderaa Data Instruments 3835 Optode), and a conductivity-temperature sensor (Sea-Bird Electronics SBE 37), all plumbed into a pumped flow stream (Fig. 1). The SeaFET has been commercialized by Satlantic, L.P.

Unlike potentiometric glass electrodes, the ISFET sensor is an active electronic device, based on Metal Oxide Semiconductor Field Effect Transistor (MOSFET) technology. When exposed to solution, the oxide coating of the MOSFET's conduction channel exchanges protons, giving rise to an interface potential that is measured as a voltage between the source of the MOSFET and a reference electrode. For further details the reader is referred to Bergveld (2003). In both the SeaFET and SeapHOx, the ISFET voltage is recorded relative to two independent reference electrodes: an *internal* Ag/AgCl reference with a liquid junction and a junctionless *external* Cl-ISE, referred to hereafter as E_{INT} and E_{EXT}, respectively (Martz et al., 2010).

Nominal voltage ranges in seawater are $E_{INT} \approx 0.03$ to 0.1 V, $E_{EXT} \approx -0.95$ to -0.8 V. Corresponding pH^{INT} and pH^{EXT} values are derived from E_{INT} and E_{EXT}, respectively. The dual reference electrode design is not a requirement. Due to the classic difficulty of achieving a stable potentiometric reference (Culberson, 1981), we elected to build a system with two independent reference electrodes (Martz et al., 2010). In our opinion, the external reference provides a theoretical improvement due to the fact that the liquid junction potential of the internal reference is unquantifiable and therefore adds uncertainty to the pH^{INT} value. However, we have also found by experience that the internal reference electrode is of the highest quality and, under many circumstances, appears to remain nearly as stable as the external reference. Retaining two reference electrodes thus provides a simple check during data QC: differences between pH^{INT} and pH^{EXT} serve as an indicator of sensor malfunction or fouling.

The approach to biofouling prevention has evolved along with our continued implementation of the *in situ* Durafet sensor. SeaFET biofouling prevention is passive: seawater is exchanged across a copper mesh screen enclosing the sensors. Improvements to the original SeaFET design include the incorporation of a flow cell over the sensors and inclusion of 70:30 Cu–Ni alloy tubing, which has proven superior to the original Cu mesh. SeaFET data discussed herein utilize the former design with Cu mesh screen. The pumped flow circuit of the SeapHOx takes advantage of the tributyltin biocide plugs located at the inlet and outlet of the conductivity cell of the SBE 37. The enclosures for both packages block most light, reducing biofouling and mitigating the direct impact of light on sensor response, which can be substantial for an ISFET. See Supplementary data (Appendix A) for further discussion of biofouling.

2.2. pH calculation

In the following section, we lay out the derivation of equations necessary for calculation of pH and calibration constants relative to both reference electrodes from sensor voltages, temperature, and salinity. For the proton-sensitive ISFET and chloride-sensitive reference electrodes, the Nernst equation gives

$$E = E^* - S \times \log(a_H a_{Cl}), \text{ where} \tag{1}$$

$$S = \frac{RT}{F} \times \ln 10, \quad \text{and} \tag{2}$$

$$\log(a_H a_{Cl}) = \log(\gamma_H \gamma_{Cl}) + \log(m_H m_{Cl}) = \log(\gamma_H \gamma_{Cl} m_{Cl}) - \text{pH}. \tag{3}$$

E is the measured sensor voltage, $R = 8.3145\ \text{Jmol}^{-1}\text{K}^{-1}$, $F = 96,487\ \text{Cmol}^{-1}$, T is temperature in Kelvin, and a_H and a_{Cl} are the proton and chloride ion activities. γ and m represent activity coefficients and molality, respectively. Note that with the exception of the calculation of the Nernst slope, S, hereafter T represents °C.

Rearranging Eq. (1) to solve for the calibration constant, E^*, and inserting the right-hand side of Eq. (3) yields

$$E^* = E + S \times [\log(\gamma_H \gamma_{Cl} m_{Cl}) - \text{pH}]. \tag{4}$$

Here we begin distinguishing between internal and external values. In solving for E^*_{INT}, we group $\{E^* - S \times [\log(\gamma_H \gamma_{Cl} m_{Cl})]\}$ in Eq. (4) and rename this term E^*_{INT} such that

$$E^*_{INT}(T) = E_{INT}(T) - S(T) \times \text{pH}_{tot}(T); \tag{5}$$

$$E^*_{INT,25} = E^*_{INT}(T = 25\,^\circ\text{C}) = E^*_{INT}(T) + \frac{dE^*_{INT}}{dT}(25\,^\circ\text{C} - T). \tag{6}$$

E_{EXT} responds to the activity of HCl, a_{HCl}, in seawater. In order to account for the changing chloride ion concentration and activity coefficients due to varying environmental conditions (*e.g.*, temperature and salinity), we calculate $\log(\gamma_H \gamma_{Cl} m_{Cl})$ explicitly (Dickson, 2007; Khoo et al., 1977) and combine this with pH on the free hydrogen ion concentration scale:

$$E^*_{EXT}(T) = E_{EXT}(T) + S \times \log(\gamma_H \gamma_{Cl} m_{Cl}) - S \times pH_{free}; \quad (7)$$

$$E^*_{EXT,25} = E^*_{EXT}(T = 25\,^\circ C) = E^*_{EXT}(T) + \frac{dE^*_{EXT}}{dT}(25\,^\circ C - T). \quad (8)$$

$E_{INT}(T)$, $E_{EXT}(T)$, and pH(T) are the recorded voltage and pH at the calibration point. Our standard practice involves transforming the pH_{free} derived from E_{EXT} to pH_{tot} as a final step during data processing, in order to compare pH^{EXT} to pH^{INT}. A Matlab script to calibrate the Durafet and calculate pH from recorded voltages, temperature, and salinity is provided in Supplementary data (see Appendix A).

2.3. Calibration

Experience indicates that the Durafet and Cl-ISE remain stable over multiple months when deployed continuously in seawater. Subsequent work, including this study, establishes that (1) the Durafet sensors repeatedly demonstrate a 100% Nernstian response (Takeshita et al., submitted for publication) and (2) exhibit a stable and repeatable potential at a given temperature, salinity, and pH, with a highly linear and stable response to temperature. Across multiple sensors, the reference potential at a given temperature (e.g., 25°C: E^*_{25}), is expected to vary by $\sim$ 1% and the temperature coefficient dE^*/dT by $\sim$ 10% (Martz et al., 2010). A 10% difference in dE^*/dT introduces errors of <0.015 pH over the temperature range observed in these studies; therefore, an average dE^*/dT is used for all sensors (values are reported by Martz et al. (2010)). The findings of Martz et al. (2010) and data below demonstrating long-term sensor stability justify a single-point calibration approach under most circumstances. The Durafet's highest achievable accuracy (better than 0.01) may require analysis of the value and stability of dE^*/dT for individual sensors.

The single-point calibration, specific to each reference electrode, defines the intercept (E^*) in a line of pH vs. sensor voltage (E) at *in situ* calibration conditions (Eq. (4) for general case; 5 and 7 for internal and external references, respectively). The calibration point is thus specified as a sensor voltage at a particular pH, temperature, and salinity; sensor voltages are extended over a range of pH, temperature, and salinity by assuming a 100% Nernst slope and a constant dE^*/dT. Due to the inter-sensor variability, E^*, corrected to a standard temperature, is described better as a "calibration constant" than as a "standard potential". It is essential to note that while pH calibration is carried out on the total scale for E^*_{INT}, it *must* be carried out on the free scale for E^*_{EXT} as the free proton concentration must be known to calculate the logarithm term in Eq. (7). For a thorough description of the various pH scales and inter-conversions, the reader is referred to Marion et al. (2011).

2.4. Characteristic electrode responses

As discussed by Martz et al. (2010) the external reference electrode exhibits a sensitive yet predictable response to salinity while the internal reference responds little to salinity over the ranges observed in this study (32.8–34.2 on the practical salinity scale (PSS-78) in oceanic deployments). Due to the unmeasurable liquid junction potential, pH^{INT} has a poorly characterized (yet small) salinity response that leads to increasing errors as salinity departs from that at the time of calibration. Although this error in pH^{INT} is presumed to be small over narrow salinity ranges, this may not be the case during large salinity variations. The thermodynamic uncertainty due to the liquid junction potential cannot be ignored when the sensor is deployed in coastal locations with significant freshwater input or large temperature variability. However, in test tank experiments over the salinity range 30–36, we are unable to identify an effect on the liquid junction potential and therefore recommend no salinity correction for the pH^{INT} under typical seawater conditions, as described in Results and discussion. Upon first contact with seawater, pH sensor voltages relative to both reference electrodes exhibit an asymptotic drift. This conditioning period arises from several sources: (1) achieving a stable flow of ions across

the liquid junction of the internal reference electrode (nominally hours), (2) replacement of Cl^- with Br^- in the solid solution of AgCl of the Cl-ISE (nominally days), (3) an ISFET conditioning component, related to the initial power-up of the chip, the exact basis of which is not fully understood (nominally 1 day), and (4) a pressure effect on the ISFET and internal reference electrode through changes in the liquid junction potential that may become important if the sensor is deployed more than ~20 m below the surface (nominally 1 h). Factors 1–3 can be addressed by operating the pH sensor continuously in seawater (never powering off the ISFET) for one week prior to deployment and taking care to keep the sensor wetted in natural seawater during transport. Unfortunately, as discussed below, these preconditioning procedures are often ignored due to the time constraints of the deployment window, resulting in sensor drift during the first days of a deployment. The fourth aspect of conditioning (a pressure effect) is problematic to characterize as it appears to be sensor specific and not necessarily repeatable. Using the Durafet sensor for profiling applications in the 0–80 m range (rated depth) is therefore discouraged. However, as shown here, Durafets have been successfully operated beyond 80 m; the key to a successful deployment rests in selecting an appropriate reference pH once the sensor is deployed and conditioned at depth.

2.5. Ancillary data

Prior to deployment, Aanderaa optodes underwent a two-point correction (zero and atmospheric saturation), in accordance with the manufacturer's recommendations, to account for changes in the factory calibration. The surface pCO_2 measurements made by the PMEL MAPCO$_2$ systems were calibrated using span gases to achieve accuracy of better than 5 μatm (Friederich et al., 1995).

pH sensor measurements are compared to (1) measurements carried out on discrete samples, pH^{disc}, using standard bench top procedures (Dickson, 2007), (2) other co-located pH sensors and analyzers, and (3) other co-located chemical sensors used to derive empirical pH values with the regional relationships from Alin et al. (2012) and thermodynamic equations from the program CO2SYS for Matlab (Van Heuven et al., 2011). The pH estimated from observed oxygen and temperature ($pH^{est}_{O_2} = pH(O_2, T)$) is reported to have a root mean squared error of 0.024 pH units relative to measurements made using bottle samples in the 2005–2011 NACP West Coast Cruise dataset (Alin et al., 2012). $pH^{est}_{O_2}$ is therefore only calculated in the region delineated by that work. $TA^{est} = TA(T, S)$ is also calculated using the regional relationships from Alin et al. (2012) and, where pCO_2 data were available (from a PMEL MAPCO$_2$ sensor), they are combined to calculate $pH^{est}_{pCO_2} = pH(pCO_2, TA^{est})$. Combining the error in TA^{est} (6.4 μmolkg^{-1}) and pCO_2 (less than 5 μatm), we estimate a propagated error of less than 0.01 pH units using CO2SYS.

pH anomalies are reported as ΔpH^{i-j} where i and j refer to the pH terms described above (e.g., $\Delta pH^{INT-disc} = pH^{INT} - pH^{disc}$). Sensor offset (i.e., intercept), c_0, and slope, c_1, relative to a reference pH value (pH^{disc}, $pH^{est}_{O_2}$, or $pH^{est}_{pCO_2}$) are calculated from a Model II least squares fit (Peltzer, 2007) of property–property plots (namely, pH^{sensor} vs. $pH^{reference}$).

2.6. Study sites

Data are presented from deployments under controlled laboratory conditions and at three field sites, each selected based on the availability of an independent validation approach (Table 1).

A SeaFET was co-located with an SBE-16 CTD and an Aanderaa optode in two consecutive mooring deployments (total sampling period of eighteen months) at 88 m on the Del Mar Buoy. The only configuration change between deployments was the refilling of the Durafet's internal reference electrolyte gel and replacement of the ceramic frit liquid junction. During this time, the 88 m sensors remained continuously beneath the surface mixed layer, providing an excellent setting in which to evaluate the empirical relationship for $pH^{est}_{O_2}$. In addition, four standard ship-based hydrocasts were carried out in close proximity to the 88 m sensors.

Seawater tanks at Scripps Institution of Oceanography were used to capture the conditioning process of two SeapHOx sensors. The conditioning experiment consisted of a 20 day deployment of new, unconditioned sensors in a 6000 L tank of seawater that had been previously filtered and then

Table 1
Deployment details.

Site	Regime	Lat. (°N)	Lon. (°W)	Sensor depth (m)	Bottom depth (m)	Sensor package(s)	Validation approach(es)
Del Mar Buoy (DMB, U. Send, SIO)	Near-shore	32.93	117.32	88	100	SeaFET, Optode, CTD	4 discrete samples, $pH^{est}_{O_2}$
Scripps Test Tank (SIO)	Laboratory	32.87	117.25	1	1	SeapHOx	Continuous spectrophotometric pH
Monterey Bay (L20, MBARI)	Near-shore	36.81	121.83	1	19	1 MBARI Durafet (also referred to as SeaFET0), 2 SeaFETs, 1 SeapHOx, 1 SAMI-pH	13 discrete samples, co-located pH sensors
California Current Ecosystem (CCE-2, U. Send, SIO)	Coastal Upwelling	34.32	120.82	1	770	SeapHOx, MAPCO$_2$	$pH^{est}_{pCO_2}$

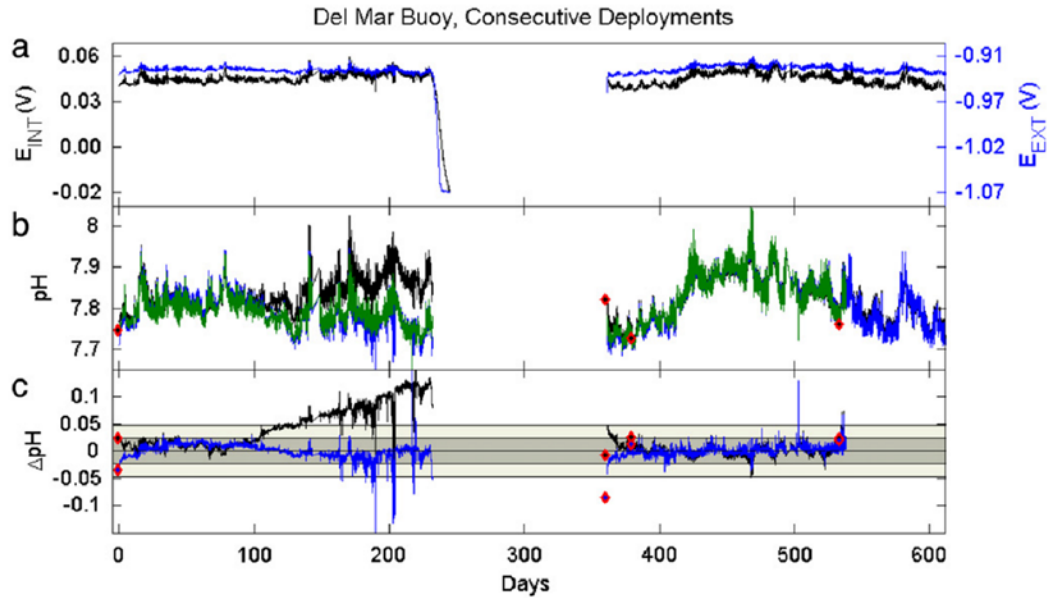

Fig. 2. Del Mar Buoy pH time-series beginning on 25-Jun-2011. (a) Raw sensor voltages for internal (black) and external (blue) reference electrodes show two consecutive deployments with a four-month gap. (b) pH is calculated using the internal and external reference electrodes and estimated from oxygen and temperature ($pH^{est}_{O_2}$, green). Discrete sample values are black diamonds with red edges. (c) Anomalies for pH^{INT} (black) and pH^{EXT} (blue) are shown relative to $pH^{est}_{O_2}$ (solid lines) and discrete samples (filled diamonds, red edges) with σ (dark gray) and 2σ (light gray) shaded regions, where standard error in $pH^{est}_{O_2}$ as reported by Alin et al. (2012) is 0.024 pH units. The optode failed on 15-Dec-2012 but the SeaFET functioned until 28-Feb-2013, leaving the pH time-series without a $pH^{est}_{O_2}$ value for the last 75 days. (For interpretation of the references to color in this figure legend, the reader is referred to the web version of this article.)

sterilized by ozonation. An automated spectrophotometric pH analyzer continuously measured pH on the tank water while the sensors were deployed. The effect of salinity on pH^{INT} and pH^{EXT} was assessed by diluting test tank salinity through discrete fresh water additions; finally, two SeapHOx packages were pressurized to discern the pressure effects on the Durafet and ISE.

The L20 mooring in Monterey Bay, CA, operated from July 12 to November 2, 2010, providing nearly four months of continuous sensor data from five independent pH sensors (Figure S1). Thirteen discrete bottle samples were collected using a 1 L bottle from a small boat during this period. Bottles were transported unpoisoned to the lab where pH was measured within 1 h. pH^{disc} was calculated from spectrophotometric pH (Clayton and Byrne, 1993) at 20°C and adjusted to *in situ* temperature using a constant slope of -0.015 pH°C^{-1}. Uncertainty in pH is dominated by use of unpurified pH indicator dye, which may result in errors up to 0.02 (Liu et al., 2011).

At the California Current Ecosystem coastal upwelling mooring (CCE-2) 1 m site, in addition to the SeapHOx, a PMEL MAPCO$_2$ sensor measured pCO_2. Here we employ empirical and thermodynamic relationships to calculate $pH^{est}_{pCO_2}$. The CCE moorings offer a rare opportunity to compare several co-located chemical sensors in a well-characterized region of the coastal ocean, significantly improving the ability to QC sensor data.

3. Results and discussion

3.1. Del Mar Buoy

The DMB data (Fig. 2) illustrate a complete cycle of sensor conditioning, drift, failure, maintenance, and redeployment. The SeaFET failure on 13-Feb-2012 (day 230) due to exhaustion of the battery pack is easily identified by examination of the raw sensor voltage (Fig. 2(a)). Upon deployment, a discrete

bottle sample was captured at 88 m from a rosette cast approximately 100 m away from the mooring and several hours after the sensor was situated at 88 m depth. Due to the lack of pre-conditioning for this particular sensor, the discrete sample could not be used as a calibration point. Upon examination of the pH values (Fig. 2(b)), it is evident that one or both of the pH signals began to drift around day 100 of the deployment. Anomalies relative to $pH_{O_2}^{est}$ (Fig. 2(c)) were minimized by setting E^* between days 20 and 50 of the deployment (after electrode conditioning and before the onset of detectable drift). These results strongly suggest a drift in the internal reference electrode.

The mooring was recovered on 25-May-2012 (day 332). The SeaFET electrodes were cleaned, including replacement of the Durafet's internal reference electrolyte gel and liquid junction, and the sensor was stored in air until redeployment on 24-Jun-2012. E^* values derived in the first deployment were applied to the redeployed SeaFET without adjustment. As seen in the right-hand portion of the time-series (Fig. 2(b), (c)), the pH calibration derived several months earlier held to better than 0.01 pH units (standard deviation of the anomaly time-series around an average anomaly of 0.002) for both reference electrodes throughout the second deployment. This result justifies the recommendation to define (and leave unchanged) E^* following a careful shoreside calibration (i.e., after the conditioning period). While in this particular case (that is, the DMB deployment), the calibration constants were calculated during deployment, by extension, this finding applies to pre-deployment calibrations, particularly since this sensor was returned to shore and then redeployed and shown to exhibit no bias. The drift observed in pH^{INT} during the first deployment of this sensor is attributed to the depletion of the internal electrolyte gel, or possibly a blockage of the liquid junction, as surmised from the sensor's return to a near-zero anomaly in the second deployment after replacement of the reference gel and liquid junction.

3.2. Scripps Test Tank

3.2.1. Salinity effect

In Fig. 3, we see the effect of rapidly changing salinity. The SeapHOx electrodes used in this experiment had already been conditioned. The spectrophotometric pH analyzer malfunctioned during this experiment, precluding the calculation of anomalies relative to an independent stable reference pH value. pH^{INT} and pH^{EXT} calculated using recorded salinity track each other closely in the long term (days) with a maximum anomaly magnitude of 0.005. This result is promising, demonstrating that the reference electrodes recondition similarly to new salinity. However, on the short term (minutes), there is a differing response time between the two calculated pH values that is exposed in sharp downward spikes in the $\Delta pH^{EXT-INT}$ anomaly time-series (Fig. 3(e) blue) that line up with the small step changes in salinity (Fig. 3(b)). Closer examination of the time-series suggests that these spikes are present in pH^{EXT}, not pH^{INT} and, furthermore, that they do not appear in the E_{EXT} time-series (Fig. 3(c)).

As the spikes are only present in calculated pH^{EXT} and not E_{EXT}, these larger anomalies must come from the dependence of pH^{EXT} on salinity, suggesting that the SeapHOx flow cell was not fully flushed in a single pumping cycle. This conclusion comes about from the observation that, for qualitatively smooth step changes in both salinity and E_{EXT}, the only remaining cause of spikiness in pH^{EXT} is effectively a true chemical mismatch between the water that the easily flushed conductivity-temperature sensor sampled and that which the more slowly flushed flow-cell-contained sensors (Durafet, ISE, and optode) sampled. In other words, the conductivity-temperature sensor sampled "new" seawater after the first pump cycle when fresh water was mixed into the tank but the pH sensor flow cell still contained seawater from the previous sample. The solution to this operational problem is a higher flush volume (achieved through longer pumping time and/or higher flow rate—engineering issues that have been addressed in the SeapHOx configuration). Importantly, the fact that these spikes result from configuration issues and not kinetic differences in electrode response times suggests that the spikes can be ignored insofar as chemical responses are concerned, making the $\Delta pH^{EXT-INT}$ anomaly negligible relative to calibration accuracy.

The anomaly based on calculation of pH using the experiment's average salinity (Fig. 3(e), green), increases by an order of magnitude, perhaps an obvious effect since pH^{EXT} is a function of salinity while

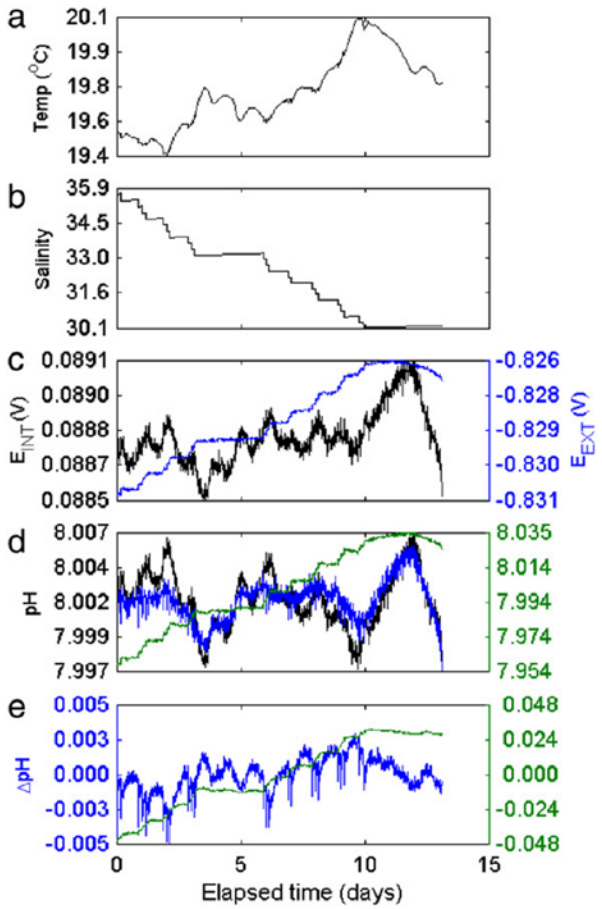

Fig. 3. The salinity of the Scripps Test Tank was changed from 35.9 to 30.1 by adding batches of fresh water at multiple intervals over fourteen days. Panels (a) and (b) show temperature and salinity, respectively. Panel (c) shows recorded E^{INT} and E^{EXT}. The left *y*-axis of panel (d) shows pH^{INT} (black) and pH^{EXT} (blue) calculated using the recorded salinity; the right axis shows pH^{EXT} (green) recalculated using the experiment's average salinity of 32.3. Panel (e) illustrates pH anomalies of $\Delta pH^{EXT-INT}$ (left axis, blue) using the recorded salinity in the calculation of pH^{EXT}; $\Delta pH^{EXT-INT}$ is shown (right axis, green) using the average salinity in the calculation of pH^{EXT}. (For interpretation of the references to color in this figure legend, the reader is referred to the web version of this article.)

pH^{INT} is not. The anomaly resulting from calculation of pH^{EXT} using an average salinity reinforces the need to deploy Durafet sensors with conductivity-temperature sensors. Because sensor performance has not been evaluated below $S = 30$ we are unable to provide recommendations for operating the sensor at lower salinities.

3.2.2. *Pressure effect*

Two SeapHOx sensors were pressurized from 0 to 35 dbar at the Scripps Test Tank Facility (Fig. 4). Pressure is shown to have the same first-order effect on all pH sensors tested: increasing pressure results in a decreasing pH signal. However, each sensor and reference electrode behaves slightly differently. *In situ* pH demonstrates that the effect of pressure on the carbonate system equilibrium constants is insufficient to account for the observed changes in sensor pH. We avoid publishing pressure coefficients for the Durafet and ISE because the effect of pressure is strongly sensor dependent (ISFET and/or reference electrodes), and a clear sign of hysteresis is observed. We therefore discourage profiling applications with the Durafet sensor packages, as noted in Materials and methods.

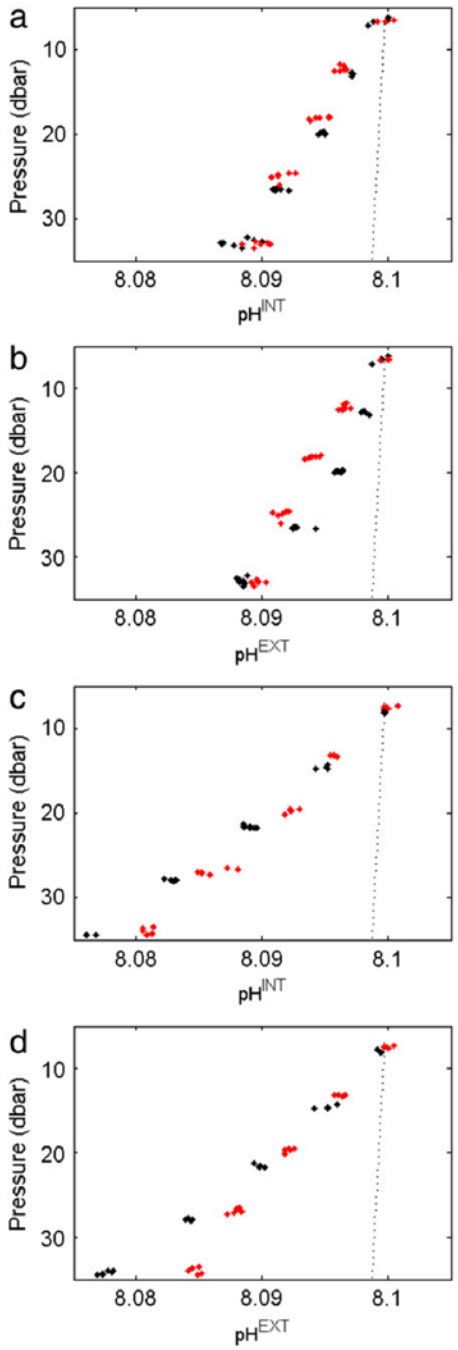

Fig. 4. Effect of pressurizing two SeapHOx sensor packages (SP041 (a, b) and SP040 (c, d)). Calculated sensor pH from increasing and decreasing pressure are shown as red and black dots, respectively. The in situ pH, calculated assuming constant TA and DIC, is represented by the black dotted lines.

3.2.3. Electrode conditioning

Fig. 5(a) clearly illustrates the sensor conditioning period. E^* was calculated using a spectrophotometric pH value at the end of the time-series. While the anomaly between pH^{INT} and

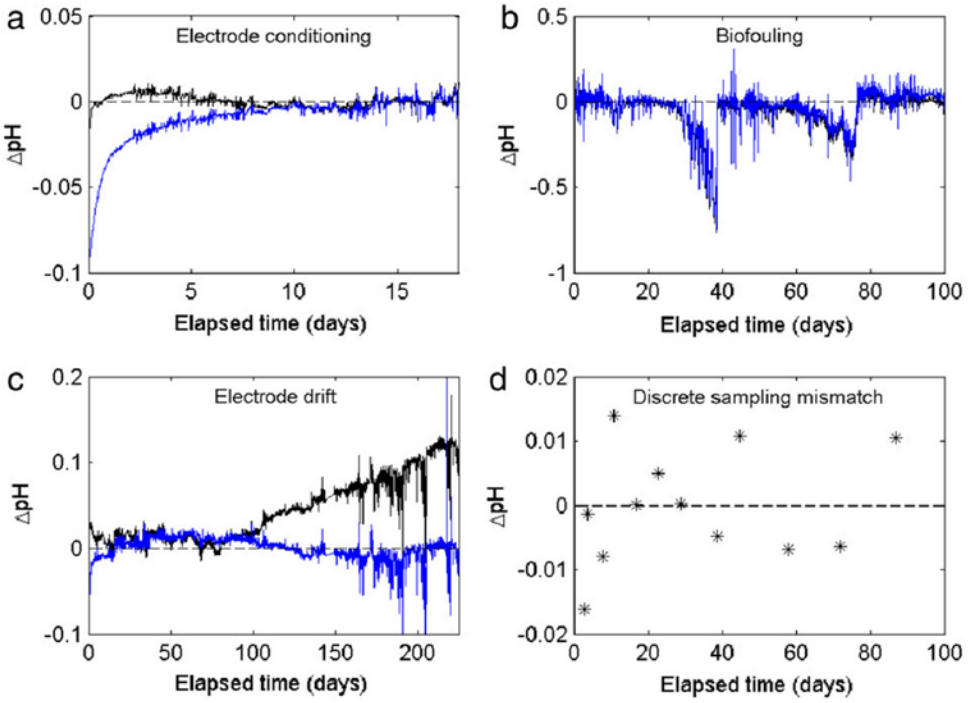

Fig. 5. Composite of anomaly time-series from (a) Scripps Test Tank SeapHOx, (b) L20 Mooring SeaFET2, (c) Del Mar Buoy SeaFET, and (d) L20 Mooring SeapHOx. Black and blue represent $\Delta pH^{INT-ref}$ and $\Delta pH^{EXT-ref}$, respectively. Reference pH values are (a) spectrophotometric, (b) pH^{INT} from a stable SeapHOx, (c) $pH^{cst}_{O_2}$, and (d) discrete sample values. Black dashed lines represent a zero anomaly. Note that *y*-axis limits differ among the four deployments, indicating that there can be significant differences in the magnitudes of various errors. (For interpretation of the references to color in this figure legend, the reader is referred to the web version of this article.)

spectrophotometric pH very quickly approaches zero at the beginning of the deployment (several hour warm-up period), pH^{EXT} takes substantially longer (approximately eight days) to condition. This anomaly is not an issue once reference electrodes are conditioned to seawater, or more specifically, its bromide concentration.

3.3. MBARI L20

Results from the L20 deployment are shown in Figs. 5(b) and 6(a). No detectable drift was observed in the SeapHOx pH^{INT} relative to the discrete samples, within the sampling error. Accordingly, the SeapHOx pH^{INT} was calibrated to minimize the anomaly relative to discrete samples; that is, E^* was adjusted to force the mean $\Delta pH^{sensor-disc}$ to zero. All SeaFETs were calibrated to minimize their mean anomaly relative to SeapHOx pH^{INT} for the first five days of the deployment, before the onset of any detectable sensor drift. The resulting time-series from only one SeaFET is shown here, but all SeaFETs responded similarly, with biofouling dominating the anomaly signal on the week to month time scale (Figure S1). The L20 data illustrate how discrepancies can arise when calibrating to individual discrete samples. The time-series anomaly shown in Fig. 5(d) depicts the offset between sensor and discrete sample values that results when E^* is set using an average value to minimize the $\Delta pH^{INT-disc}$ anomaly. This anomaly results from: (1) significant environmental pH gradients combined with small spatiotemporal mismatch between sensor and discrete sample and/or (2) errors in the discrete sample analysis. Closer analysis of the L20 time-series (Supplementary data, Appendix A) suggests that spatiotemporal mismatch is the dominant control; in a dynamic near-shore ecosystem, a small sampling discrepancy could certainly contribute (unbiased) anomalies of this magnitude. By choosing a single calibration constant based on multiple discrete samples, the error is substantially reduced.

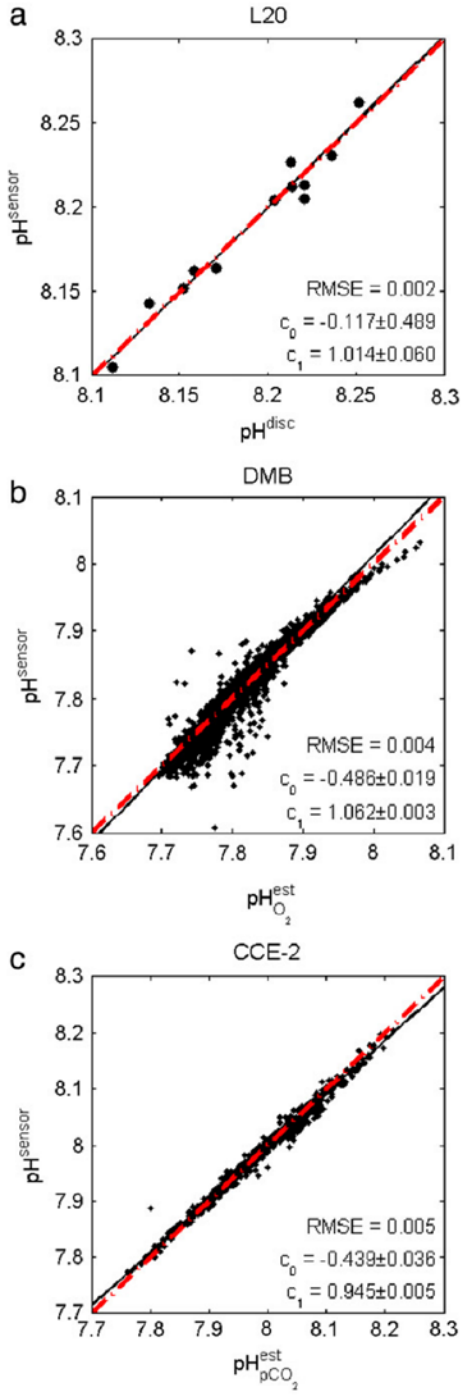

Fig. 6. Property–property plots of sensor pH vs. an independently measured (a) or estimated (b, c) reference pH. Data come from the (a) L20 deployment pH^{INT} vs. discrete sample pH, (b) Del Mar Buoy 88 m pH^{EXT} vs. $pH^{est}_{O_2}$, and (c) CCE-2 surface pH^{INT} vs. $pH^{est}_{pCO_2}$. Dashed red lines represent 1:1 ($pH^{sensor} = pH^{ref}$) and solid black lines are Model II least squares fits. In each plot, only one (stable) sensor pH is chosen. L20 (a) pH^{EXT} and DMB (b) pH^{INT} are not displayed here due to inaccuracies described in the text. CCE-2 (c) pH^{EXT} is not shown in order to simplify figure but agree closely with pH^{INT}.

3.4. California Current Ecosystem mooring: CCE-2

Several independent pH measurement techniques were employed at the CCE-2 1 m location, allowing a robust cross-comparison. Fig. 6(c) displays the property–property relationship between sensor pH^{INT} and $pH^{est}_{pCO_2}$, emphasizing the value of using an independent analyzer for an additional CO_2 system master variable. The SeapHOx calibration point was chosen to minimize the anomaly relative to $pH^{est}_{pCO_2}$, which is based on the internally-calibrated $MAPCO_2$ sensor.

3.5. Quality control

Our results demonstrate a critical dependence of sensor accuracy on choice of QC technique employed. In physically and biogeochemically dynamic environments, where it is challenging to capture synchronized discrete samples, alternate methods have been observed to disagree by greater than 0.1 pH units. At L20, SeapHOx sensors observed average pH changes of 0.023 pH $\cdot$ hr^{-1} but recorded instantaneous rates at least a full order of magnitude greater; calibrating to a sample with even slight spatiotemporal mismatch in such an environment can introduce significant errors. Moreover, the random anomalies in Fig. 5(d) suggests that resetting the calibration constant to match each discrete value would impart an artificial variability in calculated pH with a magnitude of $\sim$0.015 pH units and a frequency equal to the discrete sampling frequency. The recommendation to use an unchanging calibration for a given sensor is further supported by the DMB deployments, throughout which E^* is unchanged while results converge to near-zero anomalies following redeployment. These deployments suggest that, often, the electrode calibration constant remains stable and the pH anomaly arises from sampling mismatch. In summary, we recommend first eliminating sensor data with identifiable drift using a time-series anomaly plot followed by correcting data to more reliable contemporaneous pH measurements. If and only if the reference pH is trustworthy, E^* is calculated such that the average anomaly between sensor and reference is minimized.

While these steps seem obvious now, we note that a number of sensor users have independently suggested applying a variety of corrections: forcing the sensor data to agree with every discrete sample (either through step or linear changes in E^*, despite lack of evidence to support such variability in E^*), attempting to correct uncorrectable (unconditioned, drifting, fouled, or faulty) data, or endeavoring to correct sensor data to bottle measurements of questionable quality.

3.6. Sensor redundancy

The DMB data provide a compelling reason to deploy multiple biogeochemical sensors. The availability of two reference electrodes, an oxygen sensor, and an empirical relationship between pH and O_2 allowed pH sensor data to be salvaged from the first deployment. Without the oxygen data, it would have been impossible to pinpoint the source of pH sensor drift between the ISFET, internal reference, and external reference electrodes. The drift in pH^{INT} relative to pH^{EXT} would have signaled a problem with the system and both pH values would have been flagged as 'bad'. This type of scenario is sometimes encountered by researchers who deploy a SeaFET with no additional co-located sensors. In these cases, the time-series anomaly of pH between the two independent reference electrodes is a useful tool, as it can help to identify sensor problems such as the onset of fouling.

Without independent validation based on bottle samples, additional sensors, or post-calibration, the output of any sensor must be skeptically viewed. Simply put, in a situation where a single pH electrode (ISFET, glass, etc.) is deployed with a single reference electrode in the absence of additional biogeochemical sensors or discrete samples to provide data QC, the resulting pH time-series should be viewed as unsubstantiated. We acknowledge that these requirements add complexity to sensor deployments but suggest that the returns in data quality are worth the effort. The Durafet sensor packages offer resolution that cannot practically be matched by discrete sampling programs and have gained popularity due to their ease of use and low cost. More complex and expensive systems may eventually provide pH data of higher quality that require less data QC, but it is doubtful that the

oceanographic community would accept data from any pH sensor as "climate quality" in the absence of independent validation.

In addition to pH and O_2, co-location of a third sensor for an additional CO_2 parameter provides an even more detailed approach to QC. Fig. 6(c) illustrates this, using the CCE-2 pH and pCO_2 sensor data. Due to the use of a measured carbonate parameter, (*viz.*, pCO_2) in $pH^{est}_{pCO_2}$, there is a discernibly tight relationship with sensor-based pH. Not surprisingly, the plot of sensor pH vs. $pH^{est}_{O_2}$ (Fig. 6(b)) exhibits greater scatter due to decoupling between oceanic O_2 and CO_2, likely as the result of the vastly different rates of O_2 and CO_2 air–sea gas exchange at the surface (Sarmiento and Gruber, 2006) or possibly due to variability in organismal CO_2:O_2 stoichiometry (Martz et al., 2014).

4. Conclusions

In this work we have shown that simple comparisons between contemporaneous measurements by biogeochemical sensors can reveal offset and drift in the sensors that would otherwise be undetectable. The nature and versatility of the QC approach employed depends on the number and type of co-located sensors and discrete samples. Actively flushed (i.e., pumped) sensor packages show far greater stability than passively flushed packages, with the former remaining stable in a wide variety of environments on timescales approaching one year, and the latter often succumbing to biofouling within one month. Below the euphotic zone, the flushing scheme appears to be less important, with both packages remaining stable for greater than nine months.

Two examples of successful operation of the Durafet sensor at depths of ~90 m, slightly deeper than the rated tolerance of 100 psi, have been discussed. As more SeapHOx sensors are deployed below the mixed layer, the empirical equations relating pH and O_2 will surely provide an excellent backdrop for setting *in situ* calibration points and data QC. In turn, the sensors may provide insight into situations or locations where the empirical equations may not hold. We note that the Durafet sensor has recently been redesigned to operate at depths up to 2000 m and it is expected that the "Deep-Sea Durafet" will become commercially available in the future (Johnson et al., 2013).

It is shown that biofouling, rather than sensor drift or battery lifetime, often determines the timescale of usable data. In the worst cases, where passively flushed sensors were deployed in highly productive coastal environments, fouling compromised pH data within days to weeks (Fig. 5(b)). At the same location, the actively flushed SeapHOx exhibited no detectable drift over four months (Fig. 6(a)). Below the euphotic zone, however, the passively flushed SeaFET showed no sign of biofouling after more than 8 months (Fig. 2). Furthermore, biofouling appears to have a stronger temporal response than sensor drift. While a drifting internal reference electrode in the first DMB deployment causes an anomaly increase of ~0.01 $pHweek^{-1}$ (Fig. 5(c)), SeaFET biofouling at L20 is shown to increase the anomaly faster than 0.5 $pHweek^{-1}$ (Fig. 5(b), Figure S1).

Best practices summary

1. Preceding deployment, operate sensors in natural seawater until initial sensor drift due to conditioning stops (approximately 5–10 days), with daily samples in order to observe the predeployment conditioning period; repeat this process following deployment for validation. Power the ISFET continuously during this period.
2. Best practices require a careful shore-side calibration point based on discrete sample(s) following the conditioning period.
3. Store sensors in seawater between deployments.
4. Prevent biofouling as permitted, especially within the euphotic zone.
   i. Utilize an actively flushed flow scheme that minimizes light.
   ii. Incorporate a Sea-Bird instrument with tributyltin plugs into the flow scheme.
   iii. Wrap sensor housings with tape (McMaster-Carr P/N 6029T98) and paint with EP-SN1 or similar antifouling paint.
   iv. When using passively flushed SeaFET sensors, incorporate a 70:30 Cu–Ni alloy tube into a flow stream around the Durafet and ISE.
5. When practical, take frequent discrete samples alongside a sensor throughout a deployment in order to establish an error estimate in the sensor data.

6. Deploy co-located, independent sensors such as redundant pH, pCO_2, and O_2 sensors.
7. Estimate pH from regional empirical (Alin et al., 2012) and/or thermodynamic relationships (e.g., CO2SYS.m; Van Heuven et al., 2011).
8. Assess and control pH^{sensor} data quality with pH^{disc} and pH^{est} using the following plots:
   i. *time-series anomaly* to first identify and then eliminate periods of ostensible sensor conditioning, drift, and failure.
   ii. *property–property* to examine agreement between pH^{sensor} and an independent reference pH (through the intercept, c_0, and slope, c_1). Property–property plots are useful for quality assessment; that is, a c_0 significantly different from 0 and/or c_1 from 1 indicates bias in the sensor and/or reference pH used for comparison.
9. Apply a single calibration point, chosen to minimize the anomaly relative to a trustworthy reference pH throughout the deployment. In particular, it is not recommended to force sensor data to agree with multiple individual bottle samples as this imparts sampling error to the sensor time series.
10. Establish an error envelope for the sensor time-series. The accuracy of the sensor time-series can be no better than the reference to which it is calibrated or validated (e.g., 0.024 when using $pH^{est}_{O_2}$ below the mixed layer in the region described by Alin et al. (2012), ~0.01 when using $pH^{est}_{pCO_2}$; uncertainty relative to discrete samples is estimated from the error of the anomaly time-series).

The contrast in conditions across multiple deployments has provided the opportunity to assess several important nuances in chemical sensor performance, leading to information that will help improve future data sets. While an outright sensor failure is easily detected, discerning the gradual effect of fouling or drift can be very difficult. Clearly, the combination of pH, pCO_2, and O_2 sensor data with the empirical equations provides a robust cross-check via the pH anomaly and property–property plots, allowing the QC analyst to detect the onset of subtle problems.

Acknowledgments

This work was supported by: the California Current Acidification Network (C-CAN), with support from the Gordon and Betty Moore Foundation Award 2748, NSF Award 0961250, and the David & Lucile Packard Foundation. PJB was supported by the Department of Defense (DoD) through the National Defense Science & Engineering Graduate Fellowship (NDSEG) Program. We thank Hans Jannasch, Luke Coletti, Josh Plant and Virginia Elrod for assistance with the work at L20, Uwe Send's group for maintaining the DMB & CCE-2 moorings, Scripps Ship Operations & Marine Technical Support for their assistance deploying and recovering the DMB & CCE-2 moorings, the NOAA PMEL Carbon Program for supplying $MAPCO_2$ data, and Douglas Alden for building and maintaining the Scripps Test Tank.

Appendix A. Supplementary data

The effects of biofouling are explored further in the attached Supplementary data. pH on the three most commonly reported scales is calculated as functions of the other two scales. Matlab code is provided for sensor calibration and calculation of pH from recorded voltages. Supplementary material related to this article can be found online at http://dx.doi.org/10.1016/j.mio.2014.08.003.

References

Alin, S.R., Feely, R.A., Dickson, A.G., Hernández-Ayón, J.M., Juranek, L.W., Ohman, M.D., Goericke, R., 2012. Robust empirical relationships for estimating the carbonate system in the southern California Current System and application to CalCOFI hydrographic cruise data (2005–2011). J. Geophys. Res. 117. http://dx.doi.org/10.1029/2011JC007511.

Bergveld, P., 2003. Thirty years of ISFETOLOGY: What happened in the past 30 years and what may happen in the next 30 years. Sensors Actuators B 88, 1–20. http://dx.doi.org/10.1016/S0925-4005(02)00301-5.

Byrne, R.H., Degrandpre, M.D., Short, R.T., Martz, T.R., Merlivat, L., McNeil, C., Sayles, F.L., Bell, R., Fietzek, P., 2009. Sensors and Systems for In Situ Observations of Marine Carbion Dioxide System Variables. OceanObs'09.

Clayton, T.D., Byrne, R.H., 1993. Spectrophotometric seawater pH measurements: total hydrogen ion concentration scale calibration of m-cresol purple and at-sea results. Deep Sea Res. Part I Oceanogr. Res. Pap. 40, 2115–2129. http://dx.doi.org/10.1016/0967-0637(93)90048-8.

Culberson, C., 1981. Direct potentiometry, in: Whitfield, M., Jagner, D. (Eds.), Marine Electrochemistry: A Practical Introduction. pp. 187–262.

Cullison Gray, S.E., DeGrandpre, M.D., Moore, T.S., Martz, T.R., Friederich, G.E., Johnson, K.S., 2011. Applications of in situ pH measurements for inorganic carbon calculations. Mar. Chem. 125, 82–90. http://dx.doi.org/10.1016/j.marchem.2011.02.005.

.A.G. Dickson, C.L. Sabine, and J.R. Christian (Eds.), 2007. Guide to Best Practices for Ocean CO2 Measurements, PICES Spec. ed.

Easley, R.A., Patsavas, M.C., Byrne, R.H., Liu, X., Feely, R.A., Mathis, J.T., 2013. Spectrophotometric measurement of calcium carbonate saturation states in seawater. Environ. Sci. Technol. 47, 1468–1477. http://dx.doi.org/10.1021/es303631g.

Emerson, S., Sabine, C., Cronin, M.F., Feely, R., Cullison Gray, S.E., DeGrandpre, M., 2011. Quantifying the flux of $CaCO_3$ and organic carbon from the surface ocean using in situ measurements of O_2, N_2, pCO_2, and pH. Global Biogeochem. Cycles 25, GB3008. http://dx.doi.org/10.1029/2010GB003924.

Friederich, G.E., Brewer, P.G., Herlien, R., Chavez, F.P., 1995. Measurement of sea surface partial pressure of $C0_2$ from a moored buoy. Deep Sea Res. Part I Oceanogr. Res. Pap. 42, 1175–1186. http://dx.doi.org/10.1016/0967-0637(95)00044-7.

Frieder, C.A., Nam, S.H., Martz, T.R., Levin, L.A., 2012. High temporal and spatial variability of dissolved oxygen and pH in a nearshore California kelp forest. Biogeosciences 9, 3917–3930. http://dx.doi.org/10.5194/bg-9-3917-2012.

Hofmann, G.E., Smith, J.E., Johnson, K.S., Send, U., Levin, L.A., Micheli, F., Paytan, A., Price, N.N., Peterson, B., Takeshita, Y., Matson, P.G., Derse Crook, E., Kroeker, K.J., Cristina Gambi, M., Rivest, E.B., Frieder, C.A., Yu, P.C., Martz, T.R., 2011. High-frequency dynamics of ocean pH: a multi-ecosystem comparison. PLoS One 6 http://dx.doi.org/10.1371/journal.pone.0028983.

Johnson, K.S., Jannasch, H.W., Coletti, L.J., Carlson, R., Brown, G., Nohava, T., Martz, T.R., Takeshita, Y., Swift, D., Riser, S.C., 2013. Towards a global ocean pH observing system: First observations with Deep-Sea Durafet pH sensors on profiling floats, in: ASLO Aquatic Sciences Meeting. New Orleans, LA.

Khoo, K.H., Ramette, R.W., Culberson, C.H., Bates, R.G., 1977. Determination of hydrogen ion concentrations in seawater from 5 to 40°C: standard potentials at salinities from 20 to 45 per mil. Anal. Chem. 49, 29–34. http://dx.doi.org/10.1021/ac50009a016.

Kline, D.I., Teneva, L., Schneider, K., Miard, T., Chai, A., Marker, M., Headley, K., Opdyke, B., Nash, M., Valetich, M., Caves, J.K., Russell, B.D., Connell, S.D., Kirkwood, B.J., Brewer, P., Peltzer, E., Silverman, J., Caldeira, K., Dunbar, R.B., Koseff, J.R., Monismith, S.G., Mitchell, B.G., Dove, S., Hoegh-Guldberg, O., 2012. A short-term in situ CO_2 enrichment experiment on Heron Island (GBR). Sci. Rep. 2, 413. http://dx.doi.org/10.1038/srep00413.

Liu, X., Patsavas, M.C., Byrne, R.H., 2011. Purification and characterization of meta-cresol purple for spectrophotometric seawater pH measurements. Environ. Sci. Technol. 45, 4862–4868. http://dx.doi.org/10.1021/es200665d.

Liu, X., Wang, Z.A., Byrne, R.H., Kaltenbacher, E.A., Bernstein, R.E., 2006. Spectrophotometric measurements of pH in-situ: laboratory and field evaluations of instrumental performance. Environ. Sci. Technol. 40, 5036–5044. http://dx.doi.org/10.1021/es0601843.

Marion, G.M., Millero, F.J., Camões, M.F., Spitzer, P., Feistel, R., Chen, C.-T.A., 2011. pH of seawater. Mar. Chem. 126, 89–96. http://dx.doi.org/10.1016/j.marchem.2011.04.002.

Martz, T.R., Connery, J.G., Johnson, K.S., 2010. Testing the honeywell durafet for seawater pH applications. Limnol. Oceanogr. Methods 8, 172–184. http://dx.doi.org/10.4319/lom.2010.8.172.

Martz, T.R., Send, U., Ohman, M.D., Takeshita, Y., Bresnahan, P.J., Kim, H.-J., Nam, S., 2014. Dynamic variability of biogeochemical ratios in the Southern California current system. Geophys. Res. Lett. 41, 2496–2501. http://dx.doi.org/10.1002/2014GL059332.

Peltzer, E., 2007. Model II least squares fit: lsqfitma.m, http://www.mbari.org/staff/etp3/regress/lsqfitma.m.

Riebesell, U., Fabry, V.J., Hansson, L., Gattuso, J.-P. (Eds.), 2010. Guide to Best Practices for Ocean Acidification Research and Data Reporting. Publications Office of the European Union, Luxembourg.

Sarmiento, J.L., Gruber, N., 2006. Ocean Biogeochemical Dynamics. Princeton University Press, Princeton, NJ.

Seidel, M.P., DeGrandpre, M.D., Dickson, A.G., 2008. A sensor for in situ indicator-based measurements of seawater pH. Mar. Chem. 109, 18–28. http://dx.doi.org/10.1016/j.marchem.2007.11.013.

Takeshita, Y., Martz, T.R., Johnson, K.S., Dickson, A.G., Characterization of an ion sensitive field effect transistor and chloride ion selective electrodes for pH measurements in seawater, Anal. Chem. (submitted for publication).

Van Heuven, S., Pierrot, D., Rae, J.W.B., Lewis, E., Wallace, D.W.R., 2011. MATLAB Program Developed for CO_2 System Calculations. http://dx.doi.org/10.3334/CDIAC/otg.CO2SYS_MATLAB_v1.1.

Yu, P.C., Matson, P.G., Martz, T.R., Hofmann, G.E., 2011. The ocean acidification seascape and its relationship to the performance of calcifying marine invertebrates: Laboratory experiments on the development of urchin larvae framed by environmentally-relevant pCO_2/pH. J. Exp. Mar. Bio. Ecol. 400, 288–295. http://dx.doi.org/10.1016/j.jembe.2011.02.016.

Acknowledgements

Chapter 3, in full, is a reprint of material previously published in Methods in Oceanography, 2014: Bresnahan, P.J., Martz, T.R., Takeshita, Y., Johnson, K.S., LaShomb, M. The dissertation author was the primary investigator and author of this paper.

CHAPTER 4: A SENSOR PACKAGE FOR MAPPING PH AND OXYGEN FROM MOBILE PLATFORMS

Abstract

A novel chemical sensor package named “WavepHOx” was developed in order to facilitate the measurement of surface ocean pH, dissolved oxygen, and temperature from mobile platforms. The system comprises a Honeywell Durafet pH sensor, Aanderaa optode oxygen sensor, and chloride ion selective electrode, packaged into a hydrodynamic, lightweight housing. The WavepHOx has been deployed on a stand-up paddleboard (SUP) and a Liquid Robotics Wave Glider in multiple near-shore settings in the Southern California Bight. Integration of the WavepHOx into these mobile platforms has enabled high spatiotemporal resolution data collection in near-shore environments. It is a particularly valuable tool for mapping shallow, fragile, or densely vegetated ecosystems which cannot be easily accessed by other platforms. Results from three surveys in San Diego, California, USA, are reported in order to demonstrate the WavepHOx’s capabilities. We discuss surveys with pH and dissolved oxygen gradients of > 0.3 pH and > 50% oxygen saturation over merely tens to hundreds of meters to highlight the degree of natural spatial variability in these vegetated ecosystems. When deployed during a rigorous discrete sampling program, the WavepHOx pH had a root mean squared error of 0.028 relative to pH calculated from fifty six measurements of total alkalinity and total dissolved inorganic carbon, confirming its capacity for accurate, high spatiotemporal resolution data collection.

Introduction

As sources and sinks of carbon dioxide continue to fluctuate with an intensifying anthropogenic signature (*Sabine and Tanhua*, 2010; *Gruber et al.*, 2009), observations and analyses of the marine inorganic carbon cycle are increasingly critical. Current estimates of the ocean's annual CO_2 uptake rate have substantial uncertainty, with a range of 2±1 Pg $C \cdot yr^{-1}$ (*Takahashi et al.*, 2009). Coastal carbon budgets have proven particularly difficult to close due to their inter- and intra-ecosystem spatiotemporal heterogeneity, resulting in an estimated sink of 0.35 Pg $C \cdot yr^{-1}$ in continental shelves and source of 0.50 Pg $C \cdot yr^{-1}$ from inner estuaries, salt marshes, and mangrove forests (*Borges*, 2005; *Gattuso et al.*, 1998; *Borges*, 2010; *Borges et al.*, 2006; *Chen and Borges*, 2009; *Laruelle et al.*, 2010). However, uncertainty in continental shelf CO_2 flux remains quite large—between 50-75% (*Bauer et al.*, 2013)—such that even its sign (let alone magnitude) isn't well resolved over annual cycles (*Hales et al.*, 2005). These large uncertainties notwithstanding, it is still believed that coastal ecosystems are responsible for a disproportionately large percentage of global air-sea CO_2 flux, especially considering the fact that estuaries and continental shelves combined account for less than 10% of ocean surface area (*Cai*, 2011). *McLeod et al.* (2011) suggest that a critical gap in our understanding of coastal carbon sequestration could be filled by mapping the spatiotemporal variability of biogeochemical cycling.

There is, therefore, substantial motivation to develop a tool specifically for oceanographic carbon mapping applications. High resolution upper ocean carbon mapping is valuable in its own right as it has great potential to uncover meaningful

biogeochemical patterns that couldn't be feasibly captured with observation programs limited to bottle sampling (*Byrne et al.*, 2010). Such techniques could also be used in a "prospecting" sense—that is, to determine optimal mooring sites prior to long-term static sensor deployments. There have been numerous attempts to characterize the temporal variability of inorganic carbon chemistry using moored autonomous sensors (*Gray et al.*, 2012; *Harris et al.*, 2013; *Hofmann et al.*, 2011; *Yu et al.*, 2011; *Cullison Gray et al.*, 2011; *Frieder et al.*, 2012; *Martz et al.*, 2014; *Martz et al.*, 2009; *Price et al.*, 2012; *Kapsenberg et al.*, 2015) and countless spatial surveys of upper ocean carbon dynamics (*e.g.*, *Takahashi et al.*, 2009; *Zirino et al.*, 1986; *Crosswell et al.*, 2012; *Evans et al.*, 2013; *Evans et al.*, 2012; *Takahashi et al.*, 2014; *Alin et al.*, 2012; *Manzello et al.*, 2012; *Zhang and Fischer*, 2014; *Feely et al.*, 2001; *Feely et al.*, 1998; *Rérolle et al.*, 2014), but few tools exist to measure near-shore spatial carbon variability. None of the aforementioned sensors were built with mobility in mind to our knowledge. High-quality, autonomous, *in situ* inorganic carbon sensors tend to be much bulkier, heavier, and less hydrodynamic than desired for mobile applications. Moreover, there are many fragile ecosystems (*e.g.*, seagrass beds, shallow coral reefs) which larger, motorized vehicles couldn't easily access or which they would likely disturb.

The WavepHOx attempts to overcome this technology gap in order to offer a sensor package for coastal ocean acidification and inorganic carbon mapping studies. It was designed to be incorporated onto low-power and human-powered mobile platforms. To date, the WavepHOx has been deployed primarily on stand-up paddleboards (SUPs), as well as a Liquid Robotics Wave Glider (liquidr.com). These platforms were chosen

in order to access shallow, hard-to-reach, and fragile ecosystems, and to deploy the WavepHOx on longer, autonomous expeditions. Similar technology for mobile carbon measurements has been proposed (*Willcox et al.*, 2009) but to our knowledge no sensor data have been published. Here we outline design considerations, the WavepHOx configuration, and results from the three representative surveys (two in La Jolla Bay and one in Mission Bay).

Methods

Sensor Design

The WavepHOx sensor package comprises the Honeywell Durafet pH sensor, Aanderaa optode oxygen sensor, and Orion chloride ion selective electrode (Cl-ISE). Both the Durafet and optode include thermistors, such that the full suite of measured parameters includes pH, oxygen, and temperature (*Martz et al.*, 2010). Details on calculation and quality control of pH data can be found elsewhere (*Bresnahan et al.*, 2014). A custom ARM®-based microcontroller provides data logging and power regulation (from a rechargeable 12 V, 1.6 mA·h NiMH battery, Tenergy, P/N 11615). All components are enclosed inside a waterproof housing and the Durafet, optode, and Cl-ISE active sensing surfaces are exposed to seawater but protected by a passively-flushed dome-shaped flow cell (Figure 4.1). The flow cell has a single inlet, aligned with the forward direction of the platform, and three outlets, each adjacent to one of the main sensor components. Through the platform's forward movement (nominal speed 0.2-2 knots), water flushes through the flow cell with a residence time of approximately

2-10 seconds. Sampling period is user-determined, but can be as fast as 15 seconds. While sampling at 15 second intervals, the battery nominally lasts 5.4 hours for stand-alone applications. Flow simulations were performed using SolidWorks 2014 (with the Flow Simulation add-in) in order to optimize the flow cell's geometry (Figure 4.1). The flow cell was designed to flush as rapidly as possible while protecting the sensors from impact and direct sunlight and providing a hydrodynamic cap for the housing.

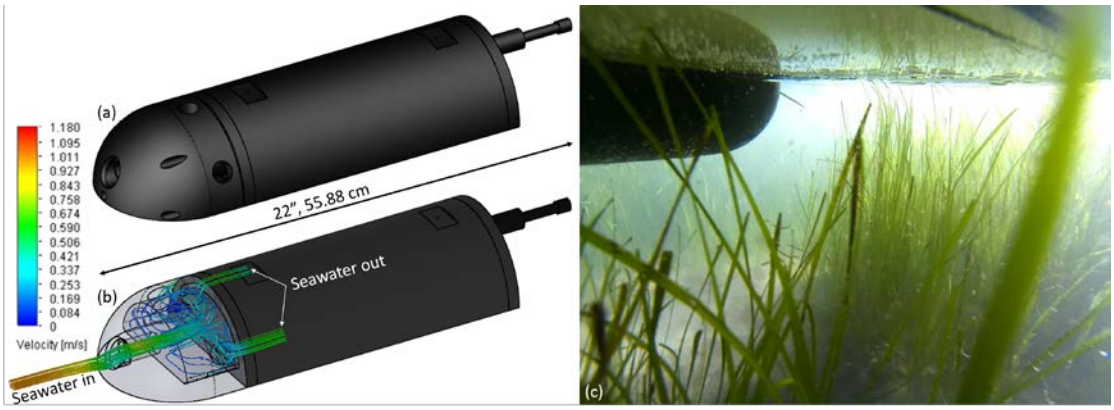

Figure 4.1. (a) WavepHOx schematic rendering and (b) flow simulation illustrating streamlines into flow cell inlet and out of the three outlets (two shown, one hidden on opposite side). Flow cell is transparent in (b) to depict the inner cavity where the pH, O_2, and temperature sensing surfaces are located. (c) The WavepHOx deployed on the bottom of a stand-up paddleboard in shallow eelgrass in Mission Bay, CA.

Electrode conditioning can be a critical limitation when using potentiometric pH sensors, but can be avoided by keeping the components immersed in seawater and never cutting off power to the sensor in between deployments (*Bresnahan et al.*, 2014). The flow cell is filled with seawater or tris buffer in synthetic seawater (*DelValls and Dickson*, 1998) and inlets/outlets plugged between deployments such that sensor components remain wetted and, therefore, always conditioned to seawater. Additionally, the battery is charged directly through a main bulkhead connector so that power never needs to be cut and recharging can take place without disassembling the housing. The

same bulkhead is used for serial communication with the instrument, which is performed both through 1) a direct RS-232 connection between the WavepHOx and a PC and 2) using an AirConsole 2.0 device with the GetConsole iOS application for wireless communication between the WavepHOx and an iPhone.

Deployments

We describe results from three WavepHOx deployments—two on a SUP and one on a Wave Glider. While the WavepHOx has two means of measuring pH via the internal and external reference electrodes (that is, pH^{INT} and pH^{EXT}, respectively), calculation of pH^{EXT} requires salinity which is not presently measured during SUP deployments, but is available from the Sea-Bird Electronics CTD sensor on the Wave Glider. We report pH^{INT} on the total scale here. The sensors used in all deployments were conditioned prior to deployment by operating the assembled WavepHOx in a 6000 L filtered seawater tank at Scripps Institution of Oceanography for two weeks. pH sensor calibration coefficients were determined using spectrophotometric pH of a discrete sample taken from the tank after the sensor's conditioning period (*Bresnahan et al.*, 2014; *Clayton and Byrne*, 1993). The optode was calibrated in accordance with the manufacturer's recommendations.

WavepHOx deployments on the SUP utilize an external GPS recorder (Garmin Quatix), synchronized with the sensor's internal clock. The WavepHOx is secured to the bottom of the SUP prior to deployment by pressing it onto 3M Dual Lock Reclosable Fastener (TB3550). Both the WavepHOx housing and SUP have permanently adhered strips of this fastener, allowing for quick assembly and disassembly prior to and after

deployments. The sensor is also tethered to an integrated D-ring on the SUP for additional security. Nominal sensor depth during SUP deployments is 10 cm.

The Wave Glider has an internal GPS logger, in addition to several peripheral instruments (*e.g.*, Sea-Bird Electronics CTD, fluorometer, barometric sensors). HDPE clamps fasten the sensor package to the Wave Glider's hull, maintaining a nominal WavepHOx depth of 50 cm. The WavepHOx can be powered internally, as described above, or externally by the Wave Glider battery via the main bulkhead connector.

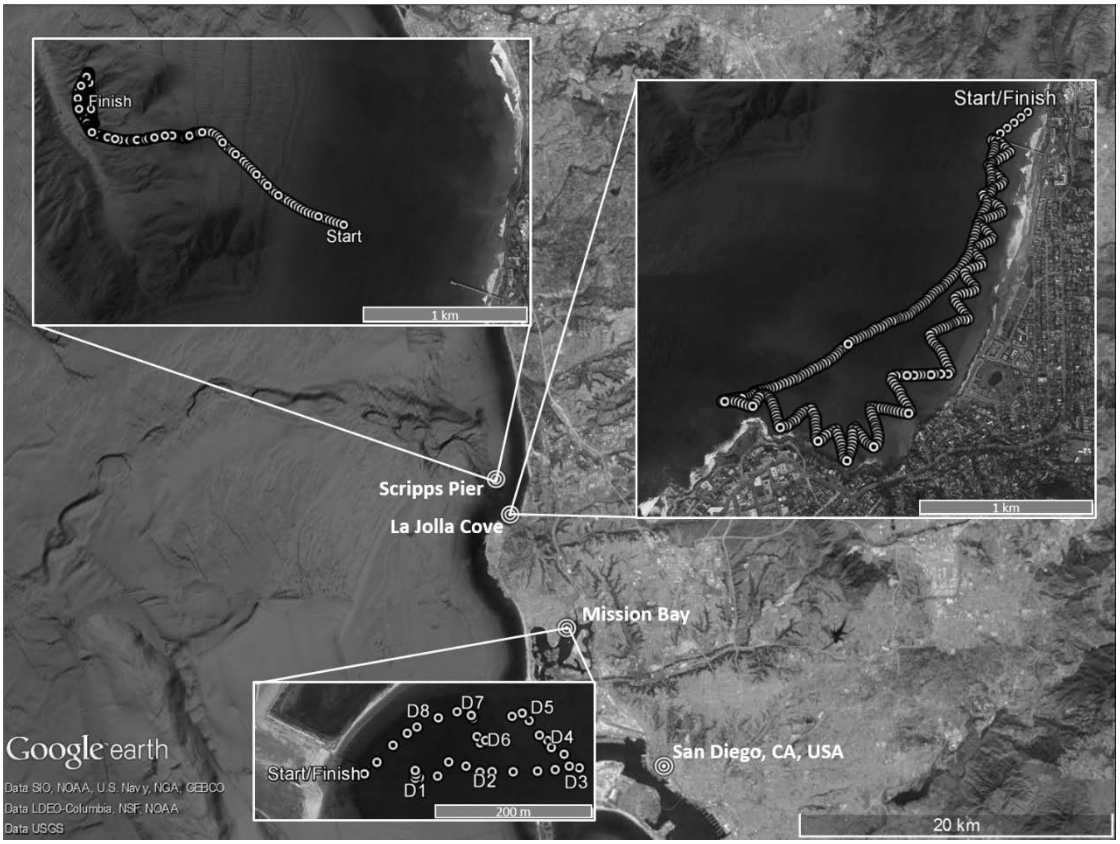

Figure 4.2. Map of field sites in San Diego, CA, USA with the survey patterns shown with circular symbols in magnified boxes. The magnified image of the Mission Bay survey also shows the eight locations where discrete samples were collected (D1-D8), eight times each for a total of sixty four discrete samples. Images from Google Earth Pro.

Mission Bay

The WavepHOx was deployed in the Kendall-Frost Reserve in Mission Bay, San Diego, CA (Figure 4.2, 32.790 °N, 117.227 °W) on a SUP from 10:00, 22-Nov-2014, through 09:00, 23-Nov-2014. Sunset was 16:44 on 22-Nov-2014; sunrise the following morning was 06:26 PST. The sampled portion of the reserve has a muddy/sandy bottom with dense eelgrass (*Zostera marina*) patches and is surrounded by a salt marsh. Surveys within a ~300 m × ~200 m grid were repeated roughly every two hours for just under twenty-four consecutive hours. Each survey lasted ~30 minutes. The WavepHOx sampled at 30 second intervals, slightly below its maximum sampling frequency, in order to conserve power during the 24-hour study. While individual survey durations varied slightly, 782 samples were collected throughout the entire 24-hour study for an average of 55 samples per survey. The sensor was charged once from 00:00-03:00, resulting in no sensor data during those hours.

In conjunction with the SUP-mounted WavepHOx, sixty-four discrete seawater samples were collected simultaneously by kayak for total alkalinity (TA) and dissolved inorganic carbon (DIC) analyses. Samples for TA and DIC were collected in 200 mL borosilicate glass bottles and fixed with 100 μL of saturated $HgCl_2$ solution. TA was determined by potentiometric acid titration using 0.1 N HCl standardized against Certified Reference Material (CRM) from Andrew Dickson's laboratory at Scripps Institution of Oceanography. An automated titrator implementing a Metrohm 876 Dosimat Plus dispensing unit and an Ecotrode Plus pH electrode (Metrohm) was used to conduct the titrations. CRMs were run every 5 samples to determine the precision of

the system (s.d. = 1.2 µmol·kg^{-1}, *n* = 20). DIC was determined using a MARIANDA Automated Infra-Red Inorganic Carbon Analyzer (AIRICA), running CRMs every 3-5 samples to validate system performance (s.d. = 1.2 µmol·kg^{-1}, *n* = 30). Temperature (18.7±0.3 °C) and salinity (34.1±0.1) were measured using an Orion 4 Star conductivity probe (Thermo Scientific). pH^{disc} (discrete sample pH on the total scale) was calculated in MATLAB using CO2SYS.m with TA, DIC, temperature, and salinity as inputs (*van Heuven et al.*, 2011).

Sensor pH (pH^{sensor}) was recalibrated to minimize the anomaly between sensor and discrete pH (*n* = 56; 8 of the 64 discrete samples did not coincide with sensor samples) (*Bresnahan et al.*, 2014). We also report a Model II least squares fit (*Peltzer*, 2007) between perturbations in pH^{disc} and pH^{sensor} from the minimum value of pH^{disc}. These perturbation variables, defined as $pH^{disc'} = pH^{disc} - \min(pH^{disc})$ and $pH^{sensor'} = pH^{sensor} - \min(pH^{disc})$, enable careful examination of the Model II fit gain and offset (or slope and y-intercept: c_1 and c_0).

La Jolla Bay

The WavepHOx was also deployed on a SUP in La Jolla Bay, San Diego, CA (Figure 4.2, 32.855 °N, 117.265 °W) on 14-Mar-2015 and 15-Jun-2015. The March study occurred during peak sunlight hours (~ 14:00) while the June survey was performed on a cloudy morning at sunrise (~ 06:00), allowing a comparison between photosynthesis-dominated and respiration-dominated patterns, respectively. The bay, largely protected within the Matlahuayl State Marine Reserve, is characterized by variable bottom type: sandy at its northern extent to a mix of rock reef, eelgrass beds

(*Zostera marina*), and kelp beds (*e.g.*, *Macrocystis pyrifera*) in the southern portion. Sampling was conducted just offshore of the breaking waves, which were approximately 25 m from shore on average. Significant wave height during the surveys was < 60 cm at Scripps Pier (http://cdip.ucsd.edu/), the northernmost extent of the study area, allowing relatively calm conditions for the operator to safely maneuver into very shallow water (< 1 m water depth). Salinity, also measured at the pier, was 33.3 (http://www.sccoos.org/data/piers/).

While the only directly measured CO_2 system master variable in this deployment is pH, TA in a seawater tank at the base of Scripps Pier has been observed to be relatively constant (TA = 2223±11 μmol·kg^{-1}) over approximately three years (*Bockmon et al.*, 2013). We combine pH_{total} and this average TA in order to calculate DIC, pCO_2, and Ω_{Ar} at *in situ* temperature. pH_{total} and pCO_2 are also calculated at 20 °C (*i.e.*, $pH_{@T=20°C}$, $pCO_{2,@T=20°C}$) in order to emphasize the chemical patterns—as opposed to physical—found throughout the survey. Uncertainties in derived variables resulting from these approximations are discussed. Data analysis was performed with MATLAB R2014b, utilizing the built-in Mapping Toolbox and freely available "breakxaxis" function.

Scripps Pier

The final WavepHOx deployment occurred on 19-Dec-2014 on board a Liquid Robotics Wave Glider, just offshore of the La Jolla Bay experiment described above (Figure 4.2, 32.876 °N, 117.280 °W). The Scripps Pier deployment lasted four hours, recording 959 pH/O_2 measurements and covering ~4 km cross-shore.

Results and Discussion

Mission Bay Results

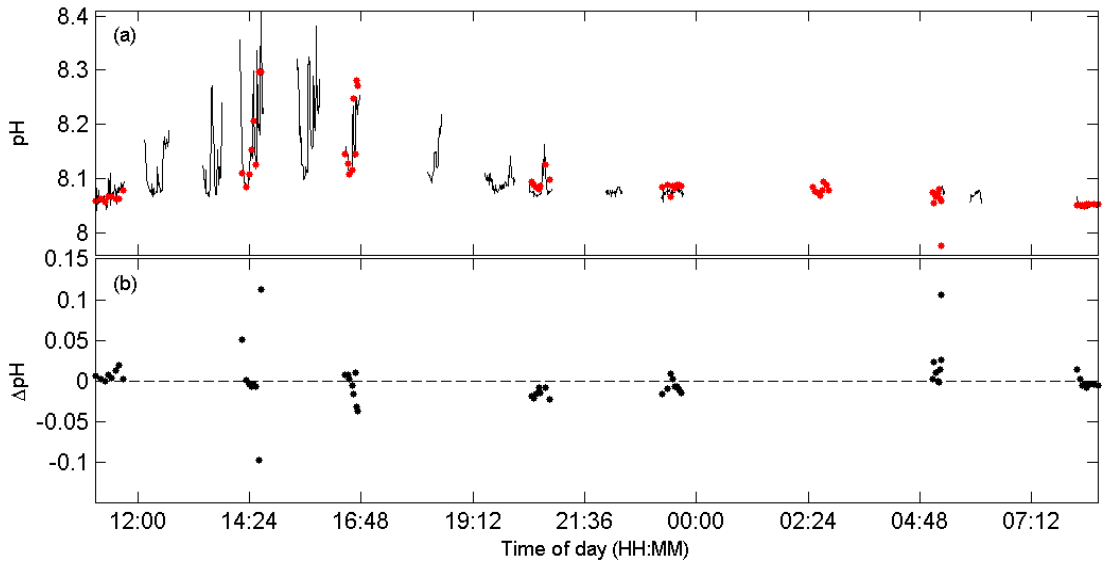

Figure 4.3. (a) pH^{sensor} (black line) and pH^{disc} (red dots) and (b) pH anomaly (pH^{sensor}-pH^{disc}) time-series in the Kendall-Frost Reserve, Mission Bay over 24 hours.

During the Kendall-Frost Reserve 24-hour study, sensor pH varied from 8.04 to 8.41 (range = 0.37) over the 300 m by 200 m grid (Figure 4.3a). Discrete pH, on the other hand, captured a substantially lower range of 0.25 (after removal of one statistical outlier during the 05:00 sampling period, defined as > 3 standard deviations difference from rest of data in given survey). The majority of variability occurred during daylight hours, due to the photosynthetic activity of the eelgrass. Figure 4.3b highlights that while sensor and discrete values are in good agreement on average, the largest anomalies tend to occur when natural variability is largest, reinforcing the difficulty of capturing sensor calibration-quality bottle samples in dynamic environments. Also noteworthy is that, while the bottle sampling captures much of the variability and may serve as validation for the sensor data, the bottle measurement campaign requires significantly

greater effort due to bottle analysis in addition to the recurring costs of operating the bench-top systems. For example, measuring DIC and TA on the sixty-four discrete samples required roughly twenty person hours including typical instrument setup and cleanup procedures.

The features which appear to represent temporal variability when displayed as a time-series (Figure 4.3) are shown to have a very strong spatial component (Figure 4.4). In the southeastern extent of the sampled area, characterized by deeper water and lower eelgrass density, pH variability is much lower (pH range < 0.05 over 24 hours) while the north-northwestern portion experiences the full pH range. In the right column of Figure 4.4, it can be seen that sensor and discrete pH anomalies reach ±0.05, illustrating the degree of variability lost when using discrete samples alone. Moreover, approximately 50% more area was covered using the sensor than using discrete samples only, reinforcing the value of an autonomous sensor for biogeochemical mapping.

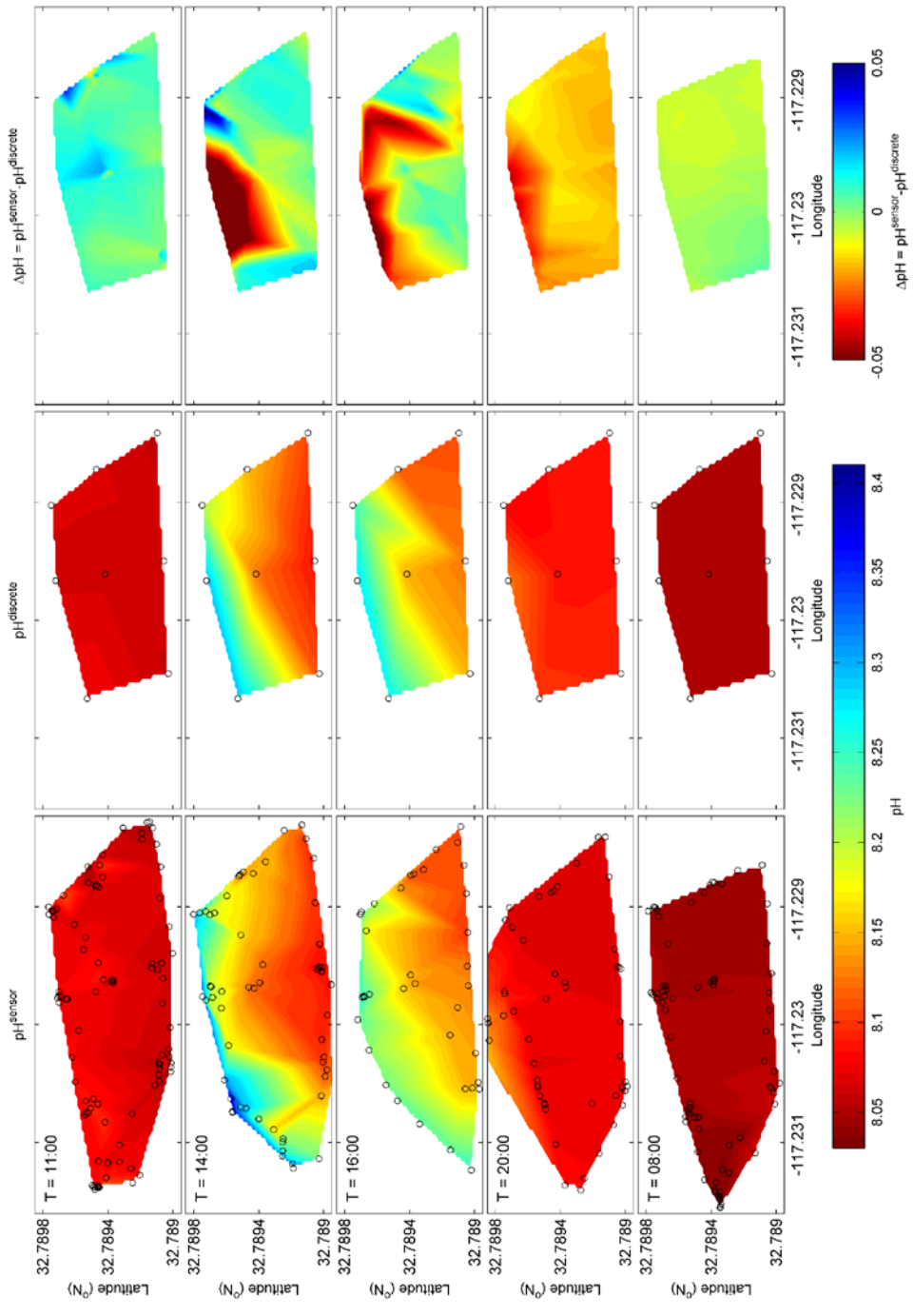

Figure 4.4. (Left) Sensor pH, (middle) discrete sample pH, and (right) anomaly of sensor minus discrete sample pH patterns in Mission Bay. Time of each survey is in upper right of panels in left column. Open circles denote sampling locations.

The property-property plot of $pH^{sensor'}$ vs. $pH^{disc'}$ (Figure 4.5) emphasizes the strong agreement between sensor and discrete pH and, importantly, the WavepHOx's ability to track true changes in pH. This finding demonstrates that the flow cell flushes sufficiently quickly relative to the speed of the platform and scales of natural chemical gradients. While a calibration based on a single discrete sample could lead to sensor pH inaccuracy of ≈ 0.1, collecting sixty four samples provides a much better means for quality control. Such a laborious sampling scheme is often unrealistic, but these findings illustrate the WavepHOx's ability to resolve spatiotemporal biogeochemical variability and set a benchmark for the level of accuracy attainable when the sensor is rigorously calibrated and validated.

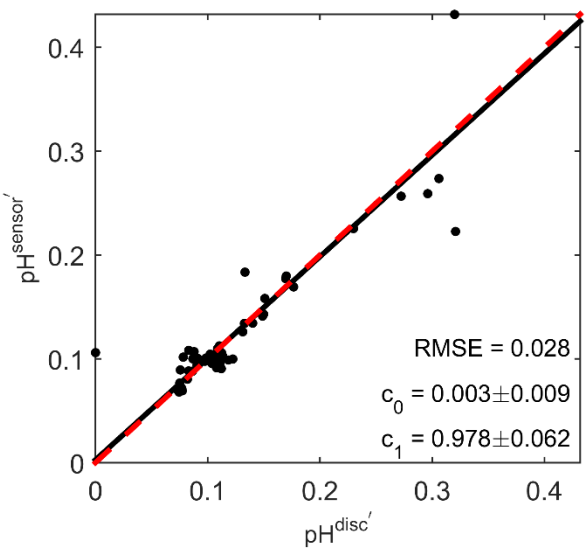

Figure 4.5. Property-property plot of $pH^{sensor'}$ vs. $pH^{disc'}$ during Kendall-Frost Reserve twenty-four hour study. The dashed red line represents the 1:1 line ($pH^{sensor'} = pH^{disc'}$) and solid black line is Model II least squares fit (Peltzer, 2007). c_0 and c_1 represent the intercept and slope (alternatively, sensor offset and gain) of the least squares fit. RMSE is the root mean square error.

La Jolla Bay SUP Results

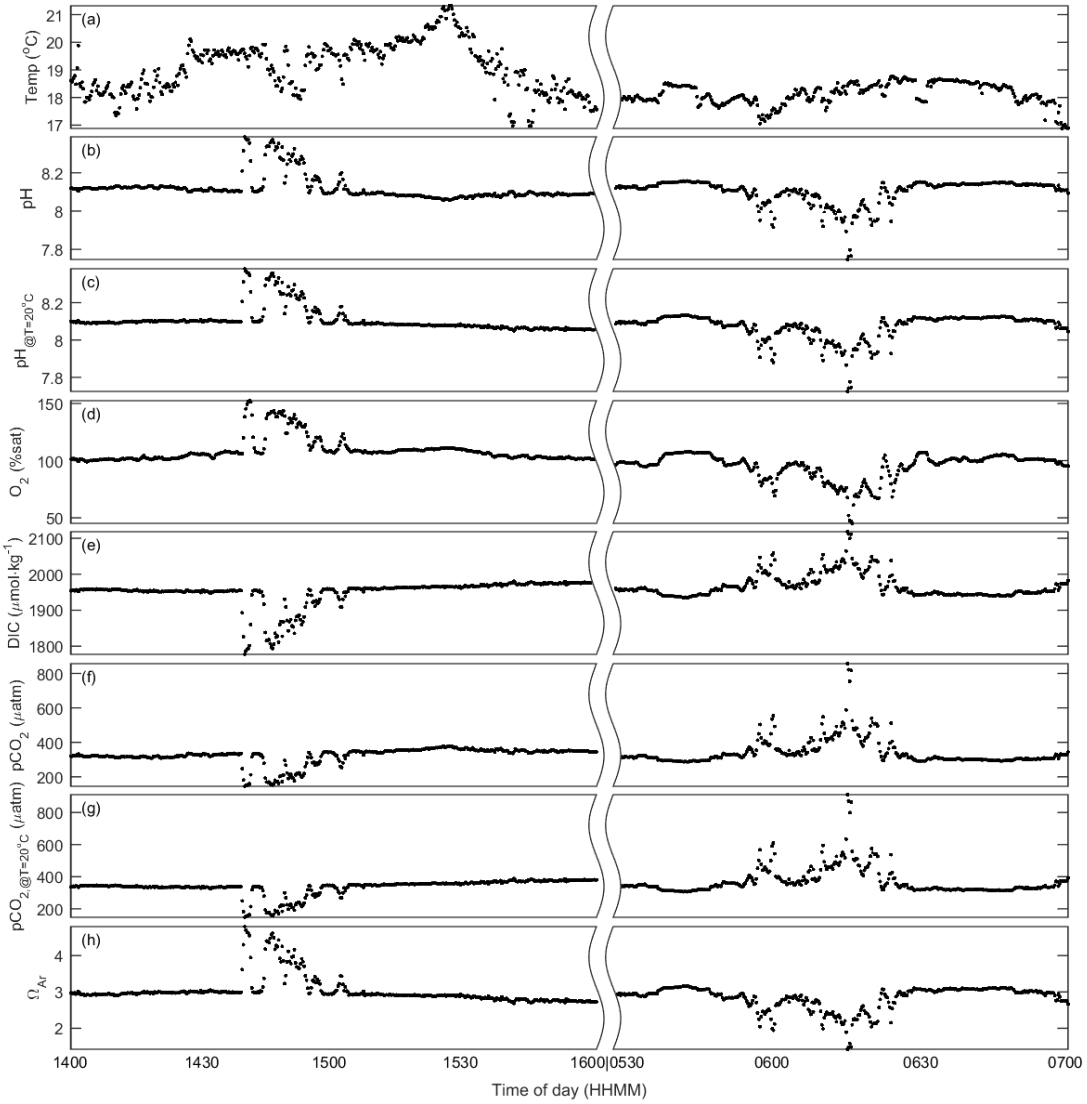

Figure 4.6. Time-series of data collected with WavepHOx on (left) 14-Mar-2015 and (right) 15-Jun-2015. Temperature (a), pH (b), and oxygen (d) are measured directly. $pH_{@T=20°C}$(c), DIC (e), pCO_2 (f), $pCO_{2,@T=20°C}$ (g), and Ω_{Ar} are derived as described in the text.

The two ~ 2 hour La Jolla Bay deployments (Figure 4.6) captured a pH range of 7.75 to 8.39 and oxygen saturation range from 45.1% to 152.1%. Meanwhile, pCO_2 spiked to over 800 µatm and was drawn down to 145.0 µatm. Both pCO_2 and pH show nearly identical patterns at *in situ* temperature and at 20 °C, suggesting that the changes

seen here are biological in nature. Moreover, the spatial patterns suggest that the high pH and oxygen region in the southern, in-shore portion of the survey results from photosynthesis on March 14th (Figure 4.7, left); the corresponding low pH and oxygen region on June 15th (Figure 4.7, right) results from respiration. The chemical signal from this rarely observed biological hot spot is mixed into the offshore waters, which remain in near equilibrium with the atmosphere.

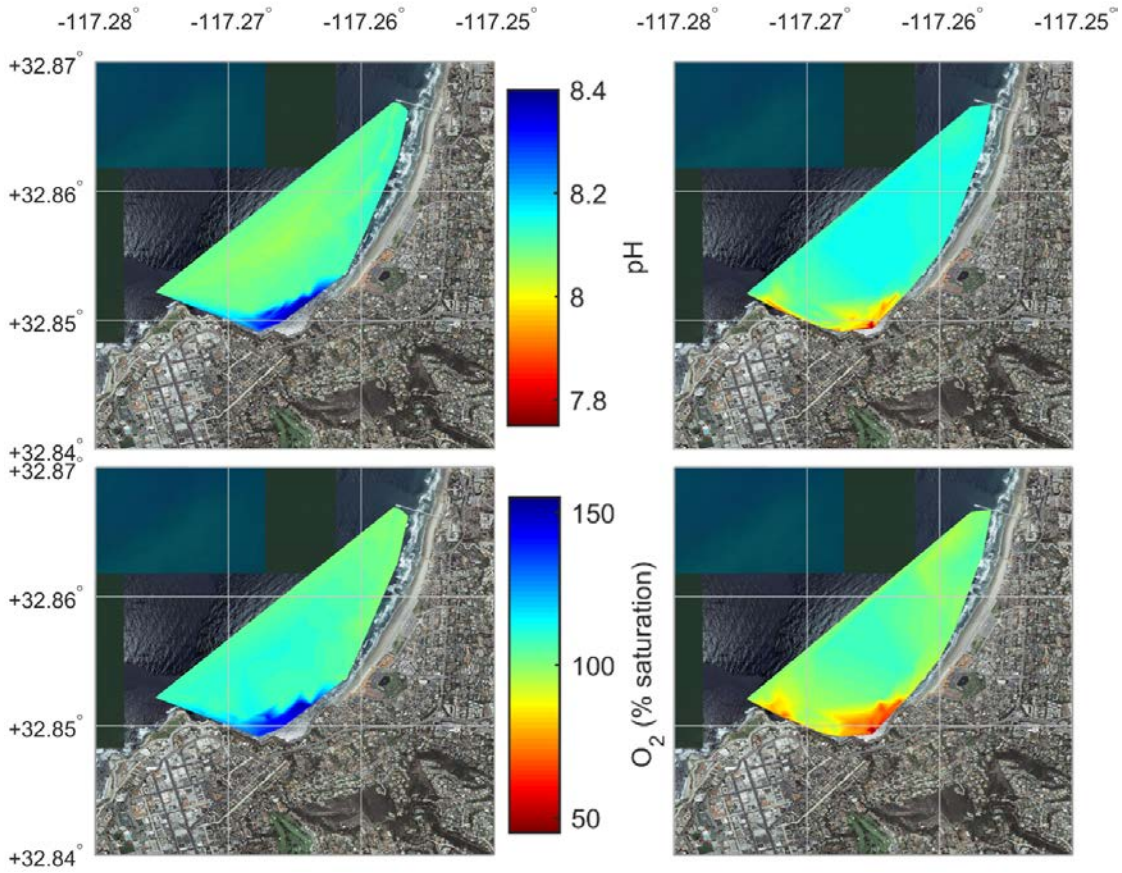

Figure 4.7. (Top) pH and (bottom) oxygen patterns in La Jolla Bay on (left) 14-Mar-2015 and (right) 15-Jun-2015.

Measuring a second CO_2 system master variable (*viz.*, TA, DIC, pCO_2) is always recommended but was not feasible during the La Jolla Bay deployment. A principle design goal for the WavepHOx was to keep the instrument's form factor as small as

possible, substantially limiting the number of integral and peripheral instruments that could be incorporated. The low natural historical variability of TA ($\sigma = 11$ μmol·kg^{-1}) (*Bockmon et al.*, 2013) translates to uncertainty in DIC and pCO_2 of approximately 10 μmol·kg^{-1} and 2 μatm, respectively. A hypothetical inaccuracy in measured pH of ±0.03 (*Bresnahan et al.*, 2014), for example, would correspond to uncertainty in DIC and pCO_2 of approximately 16 μmol·kg^{-1} and 27 μatm, respectively, demonstrating the relative importance of pH sensor calibration compared to knowledge of TA in this ecosystem.

Scripps Pier Results

The Scripps Pier WavepHOx deployment on board the Wave Glider recorded very little variability: pH = 8.048±0.002. As this experiment took place to the northwest of the La Jolla Bay survey depicted in Figure 4.7 where little variability was detected during that survey, this result is not surprising. The Durafet itself is stable to 0.0005 pH (*Martz et al.*, 2010), suggesting that this small change is in fact environmental, not simply instrumental noise, but reinforcing the findings from the La Jolla Bay deployment. We do, however, expect that continued Wave Glider surveys in and beyond this region will uncover interesting spatiotemporal patterns, especially as the survey extent is broadened. The Scripps Pier deployment successfully demonstrated the feasibility of incorporating the WavepHOx into future Wave Glider studies.

Conclusions

We have designed a pH and oxygen sensor package ideal for use on mobile platforms. The WavepHOx shows great promise for high spatiotemporal surface ocean pH and oxygen mapping. Compared to mapping pH from discrete bottle samples, using the WavepHOx is substantially less laborious. Moreover, the sensor is able to capture higher resolution—and sometimes higher magnitude—gradients than a discrete sampling scheme could reasonably achieve. We wish to emphasize that the WavepHOx is not designed specifically for citizen science applications, due to cost (> $10,000) and complexities in sensor care and calibration (*Bresnahan et al.*, 2014). However, supervised deployments by non-experts have been successful, demonstrating that the package can be operated by diverse users within and outside of the professional science community.

At Mission Bay, of the four largest pH anomaly values between sensor and discrete sample (absolute value of ΔpH > 0.05), three occurred during the survey with highest natural variability (14:00, 22-Nov-2014). This finding suggests that neither sensor nor discrete values are necessarily inaccurate, but rather it highlights the difficulties of capturing a discrete sample at the exact same time and place as the instrument. Ecosystems with large spatiotemporal gradients likely require a larger number of discrete samples for sensor calibration and validation. In summary, the utility of bottle samples carried out alongside WavepHOx deployment clearly benefits the resulting dataset by providing validation data, yet the number of bottle samples required

to validate an in situ sensor is highly site and user dependent and must be considered on a site-by-site basis (*Bresnahan et al.*, 2014).

The La Jolla Bay deployment shows large changes in inorganic carbon and dissolved oxygen across small spatial scales. Such high spatial variability is often neglected when relying on moored sensors and discrete sampling programs. Continued mapping is necessary to unearth variability across many spatial scales, especially in dynamic coastal waters, and these data must be incorporated in biogeochemical budgets.

The lack of an integrated conductivity/salinity sensor is a notable shortcoming; however, we don't believe it had a significant impact on data quality during these deployments due to small salinity ranges documented in the bottle observations (Mission Bay) and historical records (La Jolla Bay). It could have a larger effect during sampling of ecosystems with large salinity gradients (*e.g.*, estuaries with significant freshwater input). The next version of the WavepHOx will incorporate a miniature conductivity probe.

Lastly, in addition to serving as a powerful oceanographic research tool, the WavepHOx and stand-up paddleboard are a superb science outreach combination, captivating diverse audiences across Southern California. The authors have directly engaged roughly 300 individuals through indoor and outdoor presentations on the science of ocean acidification and the technology used to monitor it. The allure of collecting oceanographic data from stand-up paddleboards is a noteworthy contribution to science outreach approaches.

Acknowledgements

The authors would like to thank Timothy Ray for many inspiring conversations about giving San Diego's youth an opportunity to experience oceanographic fieldwork firsthand and his family and the Scripps Foundation for Science and the Environment for providing the funding to make it possible. PJB was supported by the Department of Defense (DoD) through the National Defense Science and Engineering Graduate (NDSEG) Fellowship Program. TW was supported by an NSF-sponsored California Current Ecosystem Long-Term Ecological Research (CCE-LTER) research experience for undergraduates (REU). Ocean Discovery Institute provided the substantial logistical support and supervision necessary to work with middle and high school students throughout this project. Yuichiro Takeshita and Yassir Eddebbar have been tremendously helpful in offering scientific and outreach guidance throughout the project. Thirty middle and high school students assisted with the Mission Bay deployment the Ocean Discovery Institute (http://oceandiscoveryinstitute.org/). Students were involved in closely-supervised field sampling, discrete sample analysis, and data analysis.

Chapter 4, in full, is currently being prepared for publication of the material. Bresnahan, P.J., Wirth, T., Martz, T.R., Andersson, A., Cyronak, T., D'Angelo, S., Pennise, J., Melville, W.K., Lenain, L., Statom, N. The dissertation author was the primary investigator and author of this material.

References

Sabine, C. L. and Tanhua, T., 2010 Estimation of Anthropogenic CO2 Inventories in the Ocean. *Annual Review of Marine Science*, 2, 175-198. doi:10.1146/annurev-marine-120308-080947

Gruber, N., Gloor, M., Mikaloff Fletcher, S. E., Doney, S. C., Dutkiewicz, S., Follows, M. J., Gerber, M., Jacobson, A. R., Joos, F., Lindsay, K., Menemenlis, D., Mouchet, A., Müller, S. A., Sarmiento, J. L. and Takahashi, T., 2009 Oceanic sources, sinks, and transport of atmospheric CO2. *Global Biogeochemical Cycles*, 23, n/a-n/a. doi:10.1029/2008GB003349

Takahashi, T., Sutherland, S. C., Wanninkhof, R., Sweeney, C., Feely, R. A., Chipman, D. W., Hales, B., Friederich, G., Chavez, F., Sabine, C., Watson, A., Bakker, D. C. E., Schuster, U., Metzl, N., Yoshikawa-Inoue, H., Ishii, M., Midorikawa, T., Nojiri, Y., Körtzinger, A., Steinhoff, T., Hoppema, M., Olafsson, J., Arnarson, T. S., Tilbrook, B., Johannessen, T., Olsen, A., Bellerby, R., Wong, C. S., Delille, B., Bates, N. R. and de Baar, H. J. W., 2009 Climatological mean and decadal change in surface ocean pCO2, and net sea–air CO2 flux over the global oceans. *Deep Sea Research Part II: Topical Studies in Oceanography*, 56, 554-577. doi:10.1016/j.dsr2.2008.12.009

Borges, A., 2005 Do we have enough pieces of the jigsaw to integrate CO2 fluxes in the coastal ocean? *Estuaries*, 28, 3-27. doi:10.1007/BF02732750

Gattuso, J. P., Frankignoulle, M. and Wollast, R., 1998 CARBON AND CARBONATE METABOLISM IN COASTAL AQUATIC ECOSYSTEMS. *Annual Review of Ecology and Systematics*, 29, 405-434. doi:10.1146/annurev.ecolsys.29.1.405

Borges, A. C.-A., 2010 A Global Sea Surface Carbon Observing System: Inorganic and Organic Carbon Dynamics in Coastal Oceans. *Proceedings of OceanObs'09: Sustained Ocean Observations and Information for Society (Vol. 2)*, ESA Publication WPP-306. doi:10.5270/OceanObs09.cwp.07

Borges, A. V., Schiettecatte, L. S., Abril, G., Delille, B. and Gazeau, F., 2006 Carbon dioxide in European coastal waters. *Estuarine, Coastal and Shelf Science*, 70, 375-387. doi:10.1016/j.ecss.2006.05.046

Chen, C.-T. A. and Borges, A. V., 2009 Reconciling opposing views on carbon cycling in the coastal ocean: Continental shelves as sinks and near-shore ecosystems as sources of atmospheric CO2. *Deep Sea Research Part II: Topical Studies in Oceanography*, 56, 578-590. doi:10.1016/j.dsr2.2009.01.001

Laruelle, G. G., Dürr, H. H., Slomp, C. P. and Borges, A. V., 2010 Evaluation of sinks and sources of CO2 in the global coastal ocean using a spatially-explicit typology of estuaries and continental shelves. *Geophysical Research Letters*, 37, L15607. doi:10.1029/2010GL043691

Bauer, J. E., Cai, W.-J., Raymond, P. A., Bianchi, T. S., Hopkinson, C. S. and Regnier, P. A. G., 2013 The changing carbon cycle of the coastal ocean. *Nature*, 504, 61-70. doi:10.1038/nature12857

Hales, B., Takahashi, T. and Bandstra, L., 2005 Atmospheric CO2 uptake by a coastal upwelling system. *Global Biogeochemical Cycles*, 19, n/a-n/a. doi:10.1029/2004GB002295

Cai, W. J., 2011 Estuarine and coastal ocean carbon paradox: CO2 sinks or sites of terrestrial carbon incineration? *Ann Rev Mar Sci*, 3, 123-45. doi:10.1146/annurev-marine-120709-142723

McLeod, E., Chmura, G. L., Bouillon, S., Salm, R., Björk, M., Duarte, C. M., Lovelock, C. E., Schlesinger, W. H. and Silliman, B. R., 2011 A blueprint for blue carbon: toward an improved understanding of the role of vegetated coastal habitats in sequestering CO2. *Frontiers in Ecology and the Environment*, 9, 552-560. doi:10.1890/110004

Byrne, R. H., DeGrandpre, M. D., Short, R. T., Martz, T. R., Merlivat, L., McNeil, C., Sayles, F. L., Bell, R. and Fietzek, P., 2010 Sensors and Systems for In Situ Observations of Marine Carbon Dioxide System Variables. *Proceedings of OceanObs'09: Sustained Ocean Observations and Information for Society (Vol. 2)*. doi:10.5270/OceanObs09.cwp.13

Gray, S. E. C., DeGrandpre, M. D., Langdon, C. and Corredor, J. E., 2012 Short-term and seasonal pH, pCO2 and saturation state variability in a coral-reef ecosystem. *Global Biogeochemical Cycles*, 26, 13. doi:10.1029/2011gb004114

Harris, K. E., DeGrandpre, M. D. and Hales, B., 2013 Aragonite saturation state dynamics in a coastal upwelling zone. *Geophysical Research Letters*, 40, 2720-2725. doi:10.1002/grl.50460

Hofmann, G. E., Smith, J. E., Johnson, K. S., Send, U., Levin, L. A., Micheli, F., Paytan, A., Price, N. N., Peterson, B., Takeshita, Y., Matson, P. G., Crook, E. D., Kroeker, K. J., Gambi, M. C., Rivest, E. B., Frieder, C. A., Yu, P. C. and Martz, T. R., 2011 High-frequency dynamics of ocean pH: a multi-ecosystem comparison. *PLoS One*, 6, e28983. doi:10.1371/journal.pone.0028983

Yu, P. C., Matson, P. G., Martz, T. R. and Hofmann, G. E., 2011 The ocean acidification seascape and its relationship to the performance of calcifying marine invertebrates: Laboratory experiments on the development of urchin larvae framed by environmentally-relevant pCO2/pH. *Journal of Experimental Marine Biology and Ecology*, 400, 288-295. doi:10.1016/j.jembe.2011.02.016

Cullison Gray, S. E., DeGrandpre, M. D., Moore, T. S., Martz, T. R., Friederich, G. E. and Johnson, K. S., 2011 Applications of in situ pH measurements for inorganic carbon calculations. *Marine Chemistry*, 125, 82-90. doi:10.1016/j.marchem.2011.02.005

Frieder, C. A., Nam, S. H., Martz, T. R. and Levin, L. A., 2012 High temporal and spatial variability of dissolved oxygen and pH in a nearshore California kelp forest. *Biogeosciences*, 9, 3917-3930. doi:10.5194/bg-9-3917-2012

Martz, T., Send, U., Ohman, M. D., Takeshita, Y., Bresnahan, P., Kim, H.-J. and Nam, S., 2014 Dynamic variability of biogeochemical ratios in the Southern California Current System. *Geophysical Research Letters*, 41, 2496-2501. doi:10.1002/2014gl059332

Martz, T. R., DeGrandpre, M. D., Strutton, P. G., McGillis, W. R. and Drennan, W. M., 2009 Sea surface pCO2 and carbon export during the Labrador Sea spring-summer bloom: An in situ mass balance approach. *Journal of Geophysical Research*, 114. doi:10.1029/2008jc005060

Price, N. N., Martz, T. R., Brainard, R. E. and Smith, J. E., 2012 Diel variability in seawater pH relates to calcification and benthic community structure on coral reefs. *PLoS One*, 7, e43843. doi:10.1371/journal.pone.0043843

Kapsenberg, L., Kelley, A. L., Shaw, E. C., Martz, T. R. and Hofmann, G. E., 2015 Near-shore Antarctic pH variability has implications for the design of ocean acidification experiments. *Sci. Rep.*, 5. doi:10.1038/srep09638

Zirino, A., Fuhrmann, R. A., Oksanen-Gooden, D., Lieberman, S. H., Clavell, C., Seligman, P. F., Mathewson, J. H., Jones, W. D., Kogelschatz, J. and Barber, R. T., 1986 pH-temperature-nutrient relationships in the eastern tropical Pacific Ocean. *Science of The Total Environment*, 58, 117-137. doi:10.1016/0048-9697(86)90082-3

Crosswell, J. R., Wetz, M. S., Hales, B. and Paerl, H. W., 2012 Air-water CO2 fluxes in the microtidal Neuse River Estuary, North Carolina. *Journal of Geophysical Research*, 117, 12. doi:10.1029/2012jc007925

Evans, W., Hales, B. and Strutton, P. G., 2013 pCO2 distributions and air–water CO2 fluxes in the Columbia River estuary. *Estuarine, Coastal and Shelf Science*, 117, 260-272. doi:10.1016/j.ecss.2012.12.003

Evans, W., Hales, B., Strutton, P. G. and Ianson, D., 2012 Sea-air CO2 fluxes in the western Canadian coastal ocean. *Progress in Oceanography*, 101, 78-91. doi:10.1016/j.pocean.2012.01.003

Takahashi, T., Sutherland, S. C., Chipman, D. W., Goddard, J. G., Ho, C., Newberger, T., Sweeney, C. and Munro, D. R., 2014 Climatological distributions of pH, pCO2, total CO2, alkalinity, and CaCO3 saturation in the global surface ocean, and temporal changes at selected locations. *Marine Chemistry*, 164, 95-125. doi:10.1016/j.marchem.2014.06.004

Alin, S. R., Feely, R. A., Dickson, A. G., Hernández-Ayón, J. M., Juranek, L. W., Ohman, M. D. and Goericke, R., 2012 Robust empirical relationships for estimating the carbonate system in the southern California Current System and application to CalCOFI hydrographic cruise data (2005–2011). *Journal of Geophysical Research*, 117. doi:10.1029/2011jc007511

Manzello, D. P., Enochs, I. C., Melo, N., Gledhill, D. K. and Johns, E. M., 2012 Ocean Acidification Refugia of the Florida Reef Tract. *PLoS ONE*, 7, e41715. doi:10.1371/journal.pone.0041715

Zhang, J. Z. and Fischer, C. J., 2014 Carbon dynamics of Florida Bay: spatiotemporal patterns and biological control. *Environ Sci Technol*, 48, 9161-9. doi:10.1021/es500510z

Feely, R., Sabine, C., Takahashi, T. and Wanninkhof, R., 2001 Uptake and Storage of Carbon Dioxide in the Ocean: The Global CO2 Survey. *Oceanography*, 14, 18-32. doi:10.5670/oceanog.2001.03

Feely, R. A., Wanninkhof, R., Milburn, H. B., Cosca, C. E., Stapp, M. and P. Murphy, P., 1998 A new automated underway system for making high precision pCO2 measurements onboard research ships. *Analytica Chimica Acta*, 377, 185-191. doi:10.1016/S0003-2670(98)00388-2

Rérolle, V. M. C., Ribas-Ribas, M., Kitidis, V., Brown, I., Bakker, D. C. E., Lee, G. A., Shi, T., Mowlem, M. C. and Achterberg, E. P., 2014 Controls on pH in surface waters of northwestern European shelf seas. *Biogeosciences Discussions*, 11, 943-974. doi:10.5194/bgd-11-943-2014

Willcox, S., Meinig, C., Sabine, C. L., Lawrence-Slavas, N., Richardson, T., Hine, R. and Manley, J., 2009 An autonomous mobile platform for underway surface carbon

measurements in open-ocean and coastal waters. *OCEANS 2009, MTS/IEEE Biloxi - Marine Technology for Our Future: Global and Local Challenges*, 1-8.

Martz, T. R., Connery, J. G. and Johnson, K. S., 2010 Testing the Honeywell Durafet for seawater pH applications. *Limnology and Oceanography: Methods*, 8, 172-184. doi:10.4319/lom.2010.8.172

Bresnahan, P. J., Martz, T. R., Takeshita, Y., Johnson, K. S. and LaShomb, M., 2014 Best practices for autonomous measurement of seawater pH with the Honeywell Durafet. *Methods in Oceanography*, 9, 44-60. doi:10.1016/j.mio.2014.08.003

DelValls, T. A. and Dickson, A. G., 1998 The pH of buffers based on 2-amino-2-hydroxymethyl-1,3-propanediol ('tris') in synthetic sea water. *Deep Sea Research Part I: Oceanographic Research Papers*, 45, 1541-1554. doi:10.1016/S0967-0637(98)00019-3

Clayton, T. D. and Byrne, R. H., 1993 Spectrophotometric seawater pH measurements: total hydrogen ion concentration scale calibration of m-cresol purple and at-sea results. *Deep Sea Research Part I: Oceanographic Research Papers*, 40, 2115-2129. doi:10.1016/0967-0637(93)90048-8

van Heuven, S., Pierrot, D., Rae, J. W. B., Lewis, E. and Wallace, D. W. R., 2011 MATLAB Program Developed for CO2 System Calculations. ORNL/CDIAC-105b. Carbon Dioxide Information Analysis Center, Oak Ridge National Laboratory, U.S. Department of Energy, Oak Ridge, Tennessee. doi:10.3334/CDIAC/otg.CO2SYS_MATLAB_v1.1

Peltzer, E., 2007 Model II least squares fit: lsqfitma.m.

Bockmon, E. E., Frieder, C. A., Navarro, M. O., White-Kershek, L. A. and Dickson, A. G., 2013 Technical Note: Controlled experimental aquarium system for multi-stressor investigation of carbonate chemistry, oxygen saturation, and temperature. *Biogeosciences*, 10, 5967-5975. doi:10.5194/bg-10-5967-2013